DOCTORAL (PhD) DISSERTATION

Abdul Wafi

University of Pannonia
2021

Doctoral (PhD) Dissertation

University of Pannonia

Doctoral School of Chemistry and Environmental Sciences

DOI:10.18136/PE.2021.784

Preparation and characterization of nitrogen-doped TiO_2 semiconductors for photocatalytic degradations

Written by
Abdul Wafi

Supervisors:
Dr. Ottó Horváth, DSc
Full Professor

Dr. Erzsébet Szabó-Bárdos, PhD
Associate Professor

University of Pannonia, Center of Natural Sciences
Research Group of Environmental and Inorganic Photochemistry
Veszprém, 2021

Preparation and characterization of nitrogen-doped TiO_2 semiconductors for photocatalytic degradations

Thesis for obtaining a PhD degree in the Doctoral School of Chemistry and Environmental Sciences of the University of Pannonia

in the branch of Natural Sciences

Written by Abdul Wafi

Supervisor(s): Dr. Ottó Horváth, DSc
Dr. Erzsébet Szabó-Bárdos, PhD

propose acceptance (yes / no) …………………………
(supervisor)

…………………………
(co-supervisor)

As reviewer, I propose acceptance of the thesis:

Name of Reviewer: Dr. Emília Tálas, PhD yes / no ……………………
(reviewer)

Name of Reviewer: Dr. Attila Demeter, PhD, DSc yes / no ……………………
(reviewer)

The PhD-candidate has achieved …..........% at the public discussion.

Veszprém, …………. 2021 ………………………………
(Chairman of the Committee)

The grade of the PhD Diploma …..................................... (…….. %)

Veszprém, …………. 2021 …………………………
(Chairman of UDHC)

Abbreviations

AOP	Advanced oxidation processes
A	Acceptor
$RO^\bullet$	Alkoxyl radical
E_g	Band-gap energy
BJH	Barret-Joyner-Halenda
BET	Brunauer-Emmett-Teller
cb	Conduction band
DSC	Differential scanning calorimetry
DTA	Differential thermal analyses
DRS	Diffuse reflectance spectra
D	Donor
EDS	Energy dispersive X-ray spectrometry
FFT	Fast Fourier transform
FTIR-ATR	Fourier transform infrared spectroscopy-attenuated total reflection
HPLC	High performance liquid chromatograph
HRTEM	High resolution transmission electron microscope
HAADF	High-angle annular dark-field
$^\bullet OOH$	Hydroperoxyl radical
1,4-HQ	1,4-hydroquinone
7-OHC	7-hydroxycoumarin
$^\bullet OH$	Hydroxyl radical
OHC	Hydroxylated coumarin or hydroxycoumarin
v_0	Initial rate
MO	Methyl orange
MB	Methylene blue
ε	Molar absorption coefficient
N-TiO_2	Nitrogen-doped TiO_2

NT-A	N-TiO_2 prepared by using ammonia as nitrogen precursor
NT-U	N-TiO_2 prepared by using urea as nitrogen precursor
e_{cb}^-	Photo-generated electron
h_{vb}^+	Photo-generated hole
k	Rate constant
ROS	Reactive oxygen species
RhB	Rhodamine B
SEM	Scanning electron microscope
S	Semiconductor
E^0	Standard redox potential
$^{\bullet}O_2^-$	Superoxide anion radical
SPR	Surface plasmon resonance
TG	Thermogravimetric analysis
TTIB	Titanium(IV) isobutoxide
TTIP	Titanium(IV) isopropoxide
TOC	Total organic carbon
TEM	Transmission electron microscope
UV	Ultraviolet
vb	Valence band
XRD	X-ray diffraction

Abstract

Heterogeneous photocatalysis has been an intensively investigated in the field of science for decades. The band gap of TiO_2 – the most commonly used semiconductor catalyst – is rather wide, therefore titanium dioxide can utilize only a small part of the sunlight's energy. However, there is an increasing demand for extending the sensitivity of this catalyst towards the visible-light region.

A visible-light active photocatalyst can be more effective in energetical sense and as an indoor application also self-cleaning and antibacterial surfaces could be realized by their use. Doping TiO_2 with different elements (N, S, B, F, Fe, Mn, Co, etc.) is a widespread technique to create defects in the crystal lattice, thus reducing the minimal energy needed to generate electron-hole pairs.

Nitrogen-doped TiO_2 catalysts with hollow and non-hollow structure were synthesized by co-precipitation (NT-A) and sol-gel (NT-U) methods, respectively. Different approaches, such as dosing order of the reagents, temperature of the synthesis, calcination time and temperature, were tested for NT-A preparation to examine the optimum outcome regarding photoactivity.

The photocatalytic performance of the catalysts were examined with coumarin as hydroxyl radical scavenger and 1,4-hydroquinone as a contaminant of emerging concern in the pharmaceutical and personal care industries. The results showed that surface structure, crystallinity, nitrogen content, and specific surface area were found to be crucial features in the photocatalytic performance of the catalysts. Due to its hollow structure and larger specific surface area, the photoactivity of NT-A was higher compared to non-hollow NT-U catalyst.

Furthermore, various silver amounts were successfully loaded on the surface of these catalysts (NT-U and NT-A) by using a facile photo-deposition technique. The results exhibited that Ag-loading on the surface of NT-U could double the photocatalytic performance with an optimum Ag concentration of 10^{-6} mol g^{-1}, while a slight but monotonous decrease was caused in this respect for the NTA catalyst upon increasing Ag concentration. In addition, an appreciable antibacterial activity against *Vibrio fischeri* strain was also observed for silver loading on the surface of NT-U, which was comparable to that of a reference material practically applied for disinfection in polymer coatings.

The photocatalytic pathways showed that the degradation of coumarin through the reaction with electron (anaerobic) and superoxide anion radical (aerobic) was more efficient than with hydroxyl radical. This is in agreement with the main route of 1,4-hydroquinone degradation, in which the cleavage of the aromatic ring takes place via reactions other than hydroxylation, and needs the presence of dissolved oxygen.

Table of Contents

1. Introduction

A wide range of chemical and biological pollutants has been generated during industrial transformation up to now, leading to significant adverse impact on the environment. Direct release of industrial wastes into water resources makes them unusable for drinking and other purposes. It is found that the existing methods are not capable to evacuate these toxic materials as well as pathogenic microorganisms from water and this situation is becoming more challenging with time [1,2]. Therefore, there is a crucial need to design and develop an advanced, cost-effective, and efficient technology that could remove a wide range of toxic substances and generate decontaminated water without interference in the ecosystem.

Several methods have been proposed for wastewater treatment, such as coagulation, filtration, adsorption, and reverse osmosis. However, these methods are relatively expensive and cannot eliminate organic pollutants or microbes entirely but just transform them from one phase to another. In recent years, advanced oxidation processes (*AOP*s) have been suggested as impressive methods for wastewater treatment. Common characteristic of *AOP*s is the production of oxidative radicals, predominantly hydroxyl radicals ($^{\bullet}$OH), which oxidize a great variety of organic compounds [3].

Heterogeneous photocatalysis may be one of the best approach for the abstraction of organic pollutants from industrial wastewaters. Photochemical purification methods are supported by the fact that in nature and in many cases contaminants are degraded in photochemical reactions. The advantage of heterogeneous photocatalysis is that the system can also run on solar energy, as a result of which not only the cost but also the emissions to the environment can also be reduced. On the one hand, light radiation is a pure energy, on the other hand, it generates pure reagents and the environmentally friendly catalyst can be recovered at the end of the process. Solar light containing visible light around 96 % and UV light around 4 % is abundantly available and free of charge [4].

Several photocatalysts (such as ZnO, TiO_2, WO_3, ZnS, CdS, and Fe_2O_3, etc.) have been studied for this purpose [3]. Among those transition metal oxides, TiO_2 is widely used as a photocatalyst due to its unique characteristics of low cost, good optical activity, high chemical stability, and non-toxic nature. In addition, TiO_2-based photocatalysts have been applied in several areas, including wastewater treatment, surfaces with self-cleaning and antifogging properties, purification of outdoor air, and indoor air-deodorization [5–7].

However, the wide band-gap of TiO_2 (~ 3.2 eV for anatase) limits its photocatalytic utilization to the UV range ($\lambda < 400$ nm). Therefore, the need for photocatalysts that also show a good photocatalytic activity by visible light ($\lambda > 400$ nm) has significantly increased [8]. Such photocatalysts will lead to the application of more sustainable technologies that take advantage of most of the solar or visible spectrum for both removal of contaminants and disinfection [8].

2. Objective

The main objective of this work is to study the material properties and photoactivity of TiO_2 based semiconductors, which can be activated under visible illumination.

Many papers have reported different strategies in order to enhance the photoactivity of TiO_2 in the visible range, reducing the band-gap energy by surface modification with dye sensitizers [9] or noble metals [10] or by doping with metal [11] or non-mental [12] elements.

Doping with non-metals such as nitrogen seems to be a viable approach in order to extend the light absorption of TiO_2 into the visible range. Hence, in this work, two different nitrogen-doped TiO_2 (N-TiO_2) catalysts will be synthesized by using different precursors and methods (co-precipitation and sol gel). Nitrogen has been proven and considered as an effective dopant to narrow the band-gap energy due to its atomic size comparable to that of oxygen, high electronegativity and ionization energy, marked thermal stability and cost-effectiveness [13,14].

In addition, nanoparticles of a noble metal such as Ag will also be decorated on the surface of prepared N-TiO_2 catalysts in order to enhance the visible-light harvesting via surface plasmon resonance (*SPR*) effect as well as to overcome the problem of fast recombination of electron-hole pairs through the formation of Schottky barriers [11,15–17]. Beside enhancing the photoactivity of N-TiO_2, Ag doping is also expected to result in an antibacterial effect due to its strong cytotoxicity toward a wide range of bacterial spectrum [18].

Furthermore, the as-prepared catalysts will be assessed by using various techniques to investigate their material properties.

Several organic model compounds have been previously used to study the photocatalytic performances of catalysts such as rhodamine B (*RhB*) [19,20], methylene blue (*MB*) [12,21], methyl orange (*MO*) [22] and eriochrome black-T [23]. However, those dye compounds can absorb a significant fraction of the light and may function as sensitizers in the visible range. Hence, to avoid both inner filter effect and possible sensitization, two organic model compounds which do not absorb in the wavelength range of the light applied will be used for photocatalytic investigation.

Coumarin will be used as a chemical probe to evaluate the formation of both hydroxyl radical and other reactive species (photo-generated electron or superoxide anion radical) under visible-light irradiation [24]. In addition, to evaluate the performance of photocatalytic degradation for emerging contaminants in the environment, 1,4-hydroquinone (1,4-HQ) will also be used as a model organic pollutant, which is a major benzene metabolite and commonly found in the wastewaters of industries manufacturing pharmaceutical or personal care products [25,26]. Lastly, antibacterial effects of the catalysts will be evaluated by using a bioluminescence method in the presence of *Vibrio fischeri* strain [27].

3. Literature Review

3.1 Advanced oxidation processes

In the past few decades, new and facile technologies, such as advanced oxidation processes, have been developed to solve the drawbacks of traditional water cleaning methods [28,29]. Since 1980s, *AOP*s techniques have exhibited a great attention to the removal of chemicals and biologicals contaminants because of their ability to generate non-selective and highly reactive oxygen species (*ROS*): hydroxyl radical ($^{\bullet}OH$), superoxide anion radical ($^{\bullet}O_2^{-}$), hydroperoxyl radical ($^{\bullet}OOH$), or alkoxyl radical ($RO^{\bullet}$) [30].

Numerous *AOP*s have been developed and studied in the past and can be classified into several techniques involving photolysis, ozonation, based on the use of hydrogen peroxide, electrochemical, sonochemical oxidation, and photocatalysis (Table 3.1) [31,32].

Table 3.1. Classification of advanced oxidation processes.

Method	Source of hydroxyl radicals
Photolysis	UV radiation
O_3-based processes	O_3 O_3/UV O_3/H_2O_2 O_3/H_2O_2/UV
H_2O_2-based processes	H_2O_2/UV H_2O_2/Fe^{2+} (Fenton) H_2O_2/Fe^{3+} (Fenton-like) H_2O_2/Fe^{2+}/UV (photo-Fenton)
Electrochemical oxidation	Electricity, 2 - 20 A (water electrolysis)
Sonochemical oxidation	Ultrasounds 20 kHz - 2 MHz (water sonolysis)
Heterogeneous photocatalysis	TiO_2/UV $TiO_2/UV/H_2O_2$

Photolysis method is based on the interaction of UV light with molecules to cause their dissociation into simpler fragments or the initiation of the oxidative destruction of otherwise inert molecules. UV has proven its capacity to initiate the cleavage of the chemical bonds of a wide variety of pharmaceuticals such as cefalexin, ciprofloxacin, sulfamethoxazole, etc. [32]. Ozone-based *AOP*s have, been employed as a single oxidation method (standard redox potential, $E^0 = 2.08$ V) for disposal of various contaminants such as anti-inflammatory drug indomethacin [33], amoxicillin [34], diclofenac, carbamazepine, sulfamethoxazole, and trimethoprim [35]. Nevertheless, artificial generations of both UV and ozone are quite expensive and require remarkable energy consumption, which is inefficient from economical perspective.

In addition, Fenton reaction is based on the use of a mixture of iron salts (Fe^{2+}) and H_2O_2 under acidic conditions, and the photo-Fenton reactions can enhance the production of hydroxyl radicals by UV - Vis illumination. Photo-Fenton processes have been investigated for removal of various pharmaceutical contaminants such as antibiotics, anti-inflammatory, analgesic and antineoplastic drugs [36,37]. This technique shows important drawbacks such as excessive sludge production and limited range of operational *pH* (usually below 3).

Therefore, among *AOP*s, heterogeneous photocatalysis has gained a great consideration due to its potential application in wastewater treatment, disinfection and hydrogen generation under solar light, which is a green and abundant energy source. It is called as a “reaction assisted by photons in the presence of semiconductor photocatalyst” [38].

3.2 Heterogeneous photocatalysis

Heterogeneous photocatalysis using semiconductors has exhibited much interest for wastewater treatment. The utilization of solar light makes this technology to be sufficiently impressive compared to other methods [39].

The term heterogeneous refers to the fact that the catalyst or semiconductor is in a solid phase and the contaminants are present in a liquid phase. Photocatalysis is defined as the speeding up of a photochemical reaction in the presence of semiconductor activated by the absorption of light [32]. Photocatalysis was firstly reported by *Barry and Stone* from their invention of the adsorption/desorption and oxidation of CO on ZnO [40]. Afterward, the photo-response of TiO_2 in daytime and oxidations of alkanes were also studied by *Djeghri and co-workers* [41].

However, *Fujishima and Honda* gained a great momentum in the field of science and technology after investigating semiconductor photocatalysts (TiO_2) for water splitting into H_2 and O_2 [42].

Numerous efforts have been invested to study the photocatalytic activity of semiconductors under UV - Vis and solar light. Heterogeneous photocatalysis has gained a lot of attention because of its various applications including degradation of organic pollutants or harmful bacteria at room temperature and pressure, almost complete mineralization process without secondary pollution, and low-cost semiconductor nanostructures [43].

However, a large-scale application of heterogeneous photocatalysis is still hindered due to mostly low quantum efficiencies, particularly in the visible light. In addition, the high concentration of organic pollutants in industrial wastes can deactivate the photocatalysts and leads to catalyst poisoning, which also limits their applicability. Hence, heterogeneous photocatalysis can only be applied in the last step of wastewater treatment processes with low concentration of organic pollutants.

Moreover, the recovery or regeneration of powdered (non-magnetic) photocatalysts from the reaction mixture by filtration or sedimentation is rather high cost and not very easy. On the other hand, immobilization of photocatalysts on different support materials, such as glass, ceramic, polymer, etc., reduces their effective surface area and, accordingly, decreases the photocatalytic performance [44].

3.3 Photocatalytic reaction

Semiconductor is a material having a valence band (*vb*) and a nearly empty conduction band (*cb*) that are separated from one another by a band gap. Typically, in a ground-state semiconductor, all electrons can be found in the *vb*.

(i) However, once the semiconductor (*S*) is illuminated with light the energy of which is equal or greater than the band-gap energy (E_g), the electrons (e_{cb}^-) are excited to the *cb* and leaving holes (h_{vb}^+) in the *vb* (Fig. 3.1, Eq. 3.1) [45].

(ii) Thereafter, a large percentage of electrons in the *cb* recombines with the holes in the *vb* due to electrostatic force of interaction, releasing heat (Eq. 3.2).

(iii-iv) Simultaneously, photo-generated electrons in the *cb* and h^+ in the *vb* migrate to the surface of the semiconductor. Then, electrons reduce acceptor (*A*) species such as O_2 (Eqs. 3.3 - 3.4), and holes oxidize donor (*D*) species (such as H_2O or OH^-) adsorbed on the surface of semiconductor (Eqs. 3.5 - 3.7).

(v) In addition, surface recombination also occurs due to the presence of a number of active surface states on the semiconductor crystal [43].

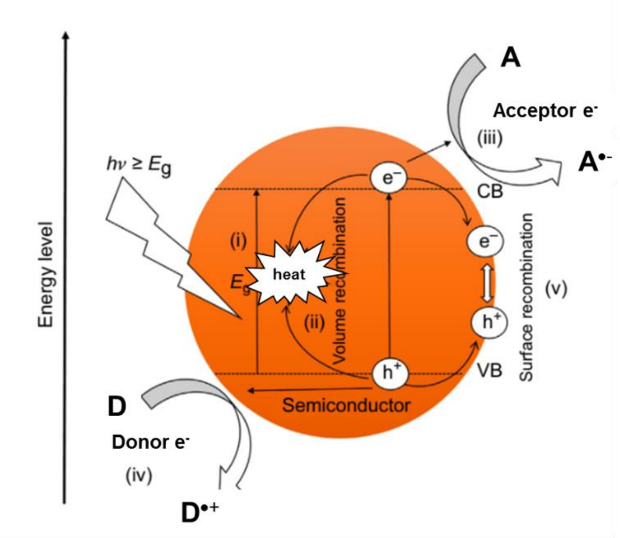

Figure 3.1. Schematic of photocatalysis mechanism [43].

$$S + h\nu \rightarrow S\,(h_{vb}^+ + e_{cb}^-) \tag{3.1}$$

$$S\,(h_{vb}^+ + e_{cb}^-) \rightarrow S + heat \tag{3.2}$$

$$S\,(e_{cb}^-) + A_{ads} \longrightarrow S + A^{\bullet -}_{ads} \tag{3.3}$$

$$S\,(e_{cb}^-) + O_{2ads} \longrightarrow S + {}^{\bullet}O_2{}^{-}_{ads} \tag{3.4}$$

$$S\,(h_{vb}^+) + D_{ads} \longrightarrow S + D^{\bullet +}_{ads} \tag{3.5}$$

$$S\ (h_{vb}^{+}) + H_2O_{ads} \rightarrow S + {}^{\bullet}OH_{ads} + H^{+} \quad (3.6)$$

$$S\ (h_{vb}^{+}) + OH^{-}_{ads} \rightarrow S + {}^{\bullet}OH_{ads} \quad (3.7)$$

The photocatalytic reaction usually involves several active species: h_{vb}^{+}, e_{cb}^{-}, hydroxyl radical, and superoxide anion radical, where hydroxyl radical is the primary oxidant in the photocatalytic degradation of the pollutant in the aqueous system. Normally, the generation of hydroxyl radical takes place via two routes: (i) the oxidation of electron donor (generally H_2O and OH^{-} in aqueous environment) by photo-generated h_{vb}^{+} (Eqs. 3.6 - 3.7) and (ii) reduction of acceptor (O_2 dissolved in the aqueous solution) by photo-generated e_{cb}^{-} to form superoxide anion radical (Eq. 3.4), followed by protonation of superoxide anion radical in a thermal reaction to form hydroperoxyl radical and then further reactions to produce hydroxyl radicals (Eqs. 3.8 - 3.11).

$${}^{\bullet}O_{2\,ads}^{-} + H^{+} \leftrightarrow {}^{\bullet}OOH_{ads} \quad (3.8)$$

$$2\,{}^{\bullet}OOH_{ads} \rightarrow H_2O_2 + O_{2ads} \quad (3.9)$$

$$H_2O_2 + {}^{\bullet}O_{2\,ads}^{-} \rightarrow {}^{\bullet}OH_{ads} + OH^{-} + O_2 \quad (3.10)$$

$$H_2O_2 + h\nu \rightarrow 2\,{}^{\bullet}OH_{ads} \quad (3.11)$$

$$\text{Pollutant} + (h_{vb}^{+}, e_{cb}^{-}, {}^{\bullet}OH, {}^{\bullet}O_2^{-}) \rightarrow \text{Mineralization} \quad (3.12)$$

Furthermore, these active species (h_{vb}^{+}, e_{cb}^{-},${}^{\bullet}OH$, ${}^{\bullet}O_2^{-}$) are able to attack many organic pollutants and mineralize them into harmless products through multi-steps reactions (Eq. 3.12) [46,47].

3.4 Fundamental semiconductor

In all semiconductors, a forbidden energy region or gap exists between the energy bands. As mentioned in chapter 3.3, the lowest empty band is called the *cb*, while the highest filled band is called the *vb* (at 0 K). However, at certain temperature (e.g., room temperature), thermal ionization may occur, leading to the occupation of the *cb* by excited electrons and leaving holes in the *vb*. The electrochemical potential of electrons in a semiconductor is determined by the

Fermi level. In other words, Fermi level defines the occupation of the energy levels at thermodynamic equilibrium [48,49].

An *intrinsic* semiconductor, also called as pure or undoped semiconductor, consists of perfect semiconductor crystals which are free of defects and impurities of other elements. The number of excited electrons and the number of holes in the *intrinsic* semiconductors are equal. Hence, the Fermi level is approximately between the valence and conduction energy levels (Fig. 3.2 a).

However, an *extrinsic* semiconductor is a pure semiconductor doped with other elements which are able to deeply modify its electrical properties. As a consequent, the number of electrons and holes are not equal. For a silicon semiconductor, doping pentavalent impurities such as arsenic yields *n*-type semiconductor, where electrons are majority carriers. In addition, doping trivalent impurities in a silicon crystal, such as boron, results in *p*-type semiconductor, where holes are majority carriers. Therefore, the Fermi level for an *extrinsic* semiconductor lies close to the *cb* (*n*-type semiconductor) or *vb* (*p*-type semiconductor) as shown in Figs. 3.2 b-c [50].

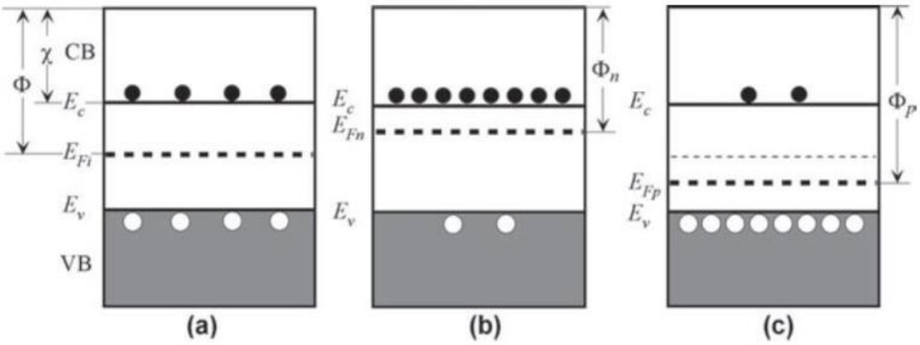

Figure 3.2. Energy band diagram of (a) *intrinsic*, (b) *n*-type, and (c) *p*-type semiconductors [50].

black circle: electron, white circle: hole, E_C: bottom of the conduction band, E_F: Fermi level, E_V: top of the valence band, Φ: work function, χ: electron affinity

Moreover, when a semiconductor comes into contact with a solution (redox species), to maintain electrostatic equilibrium, there will be a charge transfer between the semiconductor and the solution if the formal redox potential of the redox species lies inside the semiconductor band gap. At thermodynamic equilibrium, the Fermi level of the semiconductor and the formal redox potential of the redox species are aligned at the interface between the semiconductor and the redox species.

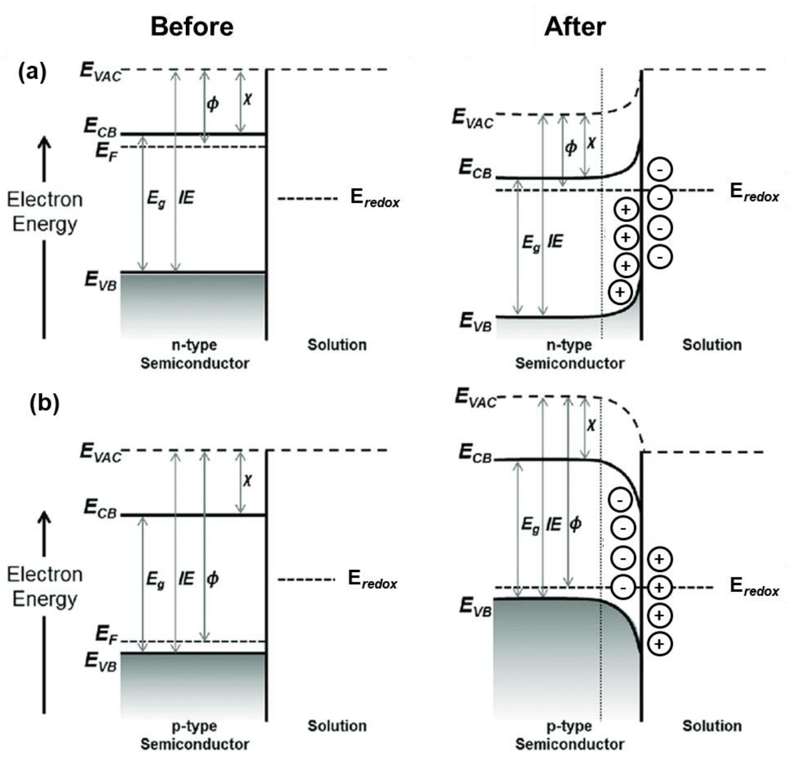

Figure 3.3. Energy levels of the semiconductor/electrolyte interface for (a) *n*-type and (b) *p*-type semiconductor before and after contact [51].

E_{VAC}: vacuum level, E_{CB}: bottom of the conduction band, E_F: Fermi level, E_{VB}: top of the valence band, E_{redox}: electrochemical redox potential E_g: band-gap energy, I_E: ionization energy, ϕ: work function, χ: electron affinity

Considering an *n*-type semiconductor, its Fermi level is typically higher than the electrochemical redox potential of the solution. As a result, the electrons will be transferred from the semiconductor to the solution. The Fermi level in the semiconductor moves "down" and the process stops when the Fermi level equals to the electrochemical redox potential. This transfer of electrons bends the bands upwards and creates a layer near the semiconductor surface that is depleted of electrons; namely depletion layer (Fig. 3.3 a).

On the other hand, if the Fermi level of the semiconductor is lower than the electrochemical redox potential, as is typical for *p*-type semiconductors, the holes flow from the semiconductor to the solution, thereby raising the Fermi level of the semiconductor until it equals to the electrochemical redox potential, as shown in Fig. 3.3 b. Similarly, a depletion layer of holes is formed [51–53].

3.5 TiO_2 semiconductor

Some examples of semiconductor oxides (e.g. TiO_2, ZrO_2, ZnO, WO_3, MoO_3, SnO_2, α-Fe_2O_3, etc.) and semiconductor sulfides (e.g. ZnS, CdS, CdSe, WS_2, MoS_2, etc.) have been utilized as catalysts for photoinduced chemical reactions due to their *intrinsic* electronic structure that consists of a filled *vb* and an empty *cb*. Generally, semiconductors with a wide band gap (E_g(TiO_2) = 3.2 eV) can be excited only under UV illumination. Conversely, if the band-gap energy of a semiconductor is relatively narrow (E_g < 3.0 eV), it can absorb the vast majority of visible light (Fig. 3.4) [54–57].

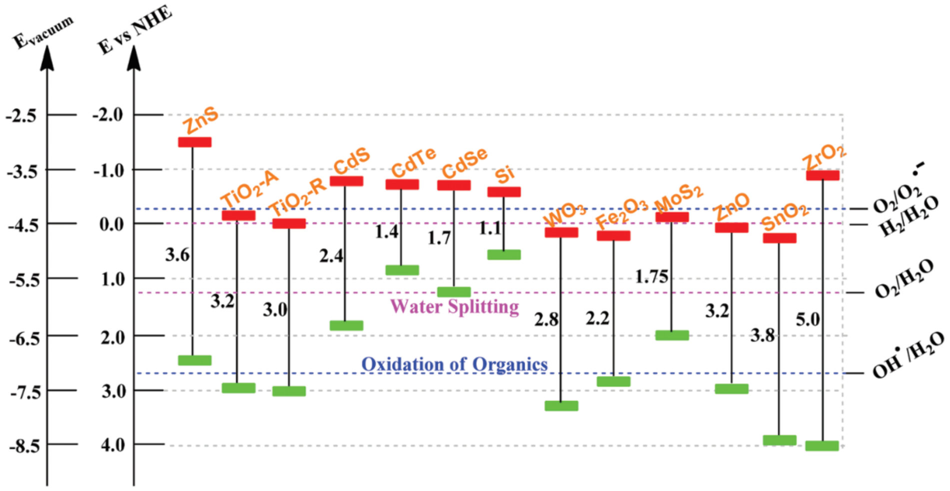

Figure 3.4. Position of *vb* (green) and *cb* (red) of various semiconductors [58].

From thermodynamic point of view, redox potentials and band-edge positions have to be taken into account when chosing a semiconductor. The redox potential of the *vb* must be more positive than that of hydroxyl radical (E^0(H_2O/$^{\bullet}OH$) = 2.8 V vs. NHE), and the *cb* must be sufficiently more negative than superoxide anion radicals (E^0(O_2/$^{\bullet}O_2^{-}$) = -0.28 V vs. NHE) in this respects [59]. Fig. 3.4 shows that the band-edge positions of TiO_2, ZnO, and ZrO_2 are relatively good for photocatalytic applications [58].

In addition, another consideration of proper semiconductors in the photocatalytic application also depends on its resistance ability. For instance, ZnO only has a stable valence of +2, and can be decomposed by photo-generated h_{vb}^{+}. Furthermore, ZnO is also prone to be deactivated due to the generation of $Zn(OH)_2$ on its surface. However, TiO_2 is more stable and suitable compared to other materials because the oxidation state of Ti in TiO_2 can be reversibly changed (from +4 and +3) [58–60]. ZnO and TiO_2 are predominant for water treatment application [61,62].

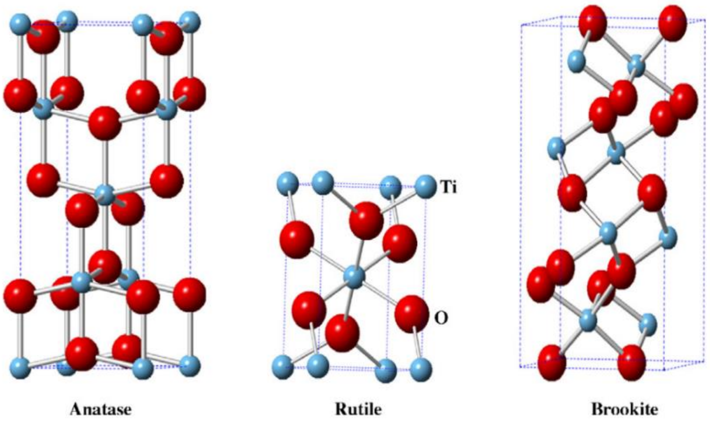

Figure 3.5. Crystal structure of anatase, rutile, and brookite [63].

TiO_2 has three different crystal structures including anatase, rutile, and brookite (Fig. 3.5). The anatase phase TiO_2 (E_g = 3.2 eV) is more active for photocatalysis applications, even though the rutile phase TiO_2 (E_g = 3.0 eV) possesses a smaller band-gap, revealing the possibility to absorb a longer-wavelength radiation. It can be attributed to the *cb* of anatase TiO_2 that is more negative compared to rutile [64].

Furthermore, the shape of anatase TiO_2 crystals is divided into different facets and each facet possesses different surface atomic arrangements or coordination of Ti atoms in TiO_2 facets (Fig. 3.6). The coordination environment of the surface atoms and the Ti-O-Ti bond angle are commonly used as criteria to predict the molecular adsorption performance on the crystal facet, which further affects the photocatalytic activity [65–67].

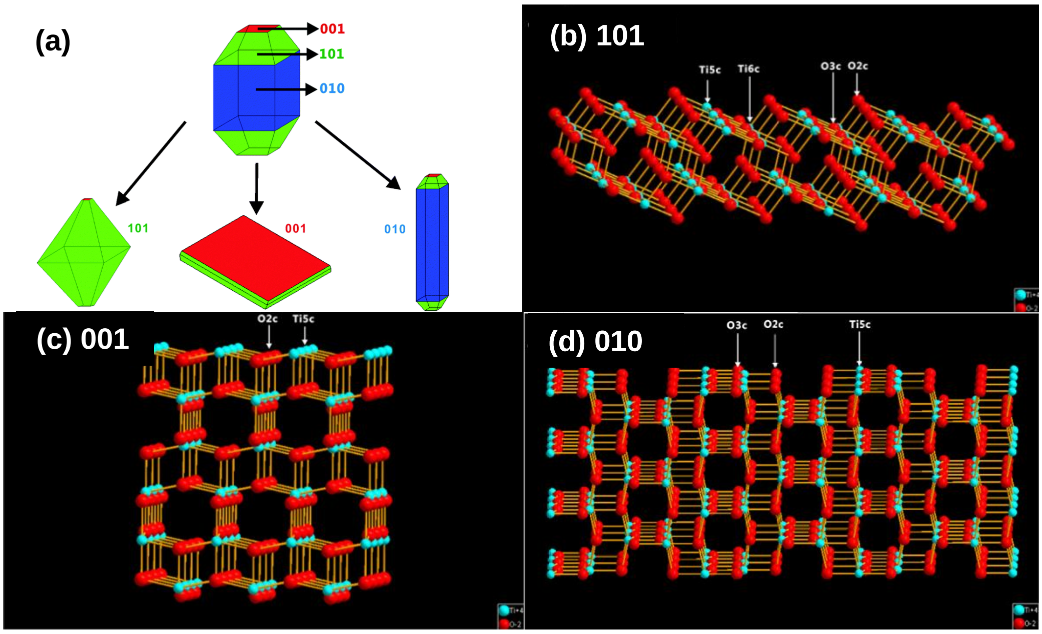

Figure 3.6. (a) Models and (b-d) atomic structure of the facets of anatase TiO_2 nanocrystals [68].

Moreover, different facets also have different *vb* and *cb* energy levels, which determine the redox potential and separation efficiency of the photo-generated carriers in a photocatalytic reaction. Many papers have reported the different electronic band structures of various TiO_2 facets [69–71]. For instance, *Pan and co-workers* reported that the band-gap energy of the (010) facets (3.23 eV) and (101) facets (3.22 eV) were larger or higher than that of the (001) facets (3.18 eV) [67], which can be attributed to the different atomic configurations on each surface [72,73].

3.6 TiO_2 modification

TiO_2-based photocatalysis is one of the most effective methods for the inhibition and control of pollutants in water. Unmodified TiO_2, which has a large band-gap, exhibits little visible-light absorption, which limits its photocatalytic application, particularly for indoors or in places where it can only be illuminated by visible light. To overcome such a vital deficiency, certain modifications toward TiO_2 photocatalyst have been attempted to enable them for visible-light responses with good efficiency such as dye sensitization, doping with metal or non-metal elements [46,74].

Dye sensitization has been reported to be one of the most promising ways to extend the photoresponse of TiO_2 photocatalysts into the visible region, and to possess certain advantages over direct photocatalysis. This is a simple and interesting strategy for achieving effective visible-light harvesting by surface modification with appropriate sensitizer molecules such as a transition metal complex or an organic dye [46,75–77].

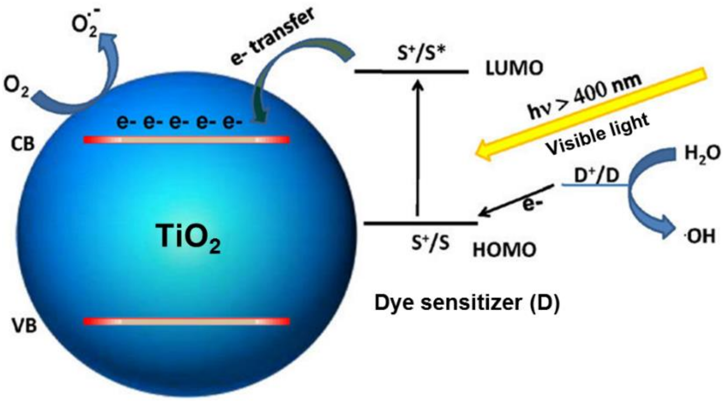

Figure 3.7. Schematic illustration showing the mechanism of dye sensitization with functionalized TiO_2 photocatalyst [78].

As shown in Fig. 3.7, the sensitization process involves photoexcitation of a sensitizer molecule to the appropriate singlet or triplet electronic excited state, followed by an electron injection from the excited sensitizer molecule into the *cb* of TiO_2. The electron injection from the sensitizer molecule to the *cb* of TiO_2 is owing to the interfacial electronic energy alignment between the excited sensitizer and the *cb* of TiO_2. In other words, the energy difference between the two materials provide the necessary driving force for electron injection [79]. Subsequently, the holes in the sensitizer molecules are delivered to the electrolyte through a redox reaction. In this respect, the maximum output voltage is the difference between the Fermi level of the TiO_2 semiconductor and the redox potential of the electrolyte [80].

The resulting electron-hole pair can be converted to various *ROS* for decomposition of organic pollutants [78]. Metalloporphyrins and ruthenium complexes are considered as efficient sensitizers due to the presence of delocalized electron systems, strong absorption in the visible region, as well as high thermal and chemical stability [81,82]. In addition to Ru(II) complexes and metalloporphyrins, other metal complexes based on Os(II) [83,84], Zn(II) [9,77], Cu(II) [81], Ir(III) [84], and Re(I) [84,85] have also been extensively used as sensitizers. *Murcia and co-workers* modified TiO_2 powder with quinizarin and zinc protoporphyrin. A higher *MO* photodegradation was achieved by using the quinizarin-TiO_2 catalyst (1.10×10^{-3} mg dm^{-3} s^{-1}) compared to zinc protoporphyrin-TiO_2 catalyst (0.41×10^{-3} mg dm^{-3} s^{-1}) under visible illumination [77].

Noble-metal deposition: Noble metals, such as platinum, silver, gold, and palladium, are also abundantly applied to modify the morphological characteristics. These metals are loaded on the surface of photocatalyst and able to extend the light absorption into the visible region through surface plasmon resonance effect as shown in Fig. 3.8 a. *SPR* is described as the collective oscillation of *cb* electrons in a metal particle, driven by the electromagnetic field of incident light [78]. Additionally, the surface metal loading may also enhance the separation of the photo-generated electrons and holes, making their lifetime longer (Fig. 3.8 b) [14,86–92], and possibly increasing the cathodic exchange current density.

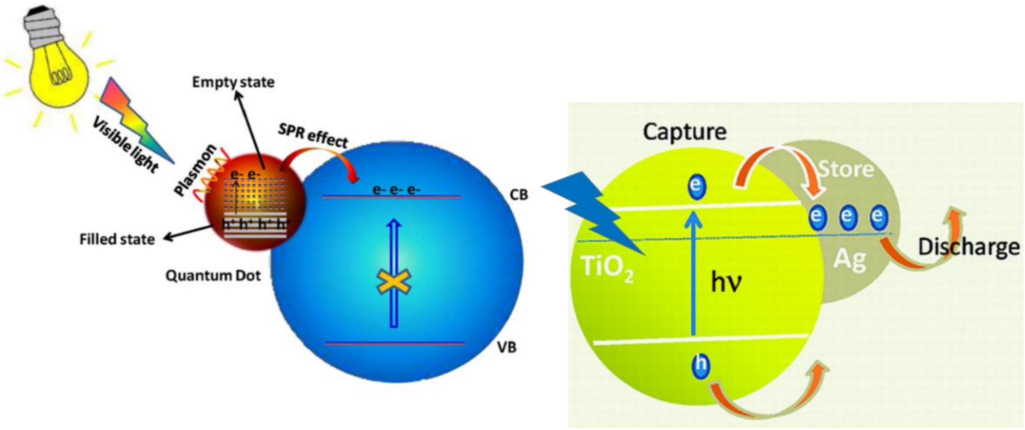

(a) (b)

Figure 3.8. Processes of (a) surface plasmon resonance [78] and (b) charge separation enhancement [63] over Ag loading onto TiO_2 photocatalyst.

Among those noble metals, Ag is the most suitable candidate for industrial applications due to its relatively low cost and easy preparation. The deposition of Ag nanoparticles onto the surface of TiO_2 can effectively increase the photocatalytic activity by accelerating charge separation and extending the absorption edge to the visible-light region [93–96]. *Bhardwaj et al.* prepared various concentration of Ag co-catalyst over TiO_2 surface via photodeposition method under UV illumination. A considerable red shift in the plasmon band was observed with a significant color change (white to light brown) with increased photodeposition time (30 - 90 min). The synthesized Ag-TiO_2 catalysts possessed appreciable photocatalytic enhancement to decompose salicylic acid (80 %) compared to Degussa P25 TiO_2 (less 20 %) under UV-light irradiation [97]. *Rabhi and co-workers* synthesized Ag-TiO_2 via sol-gel method by using titanium isopropoxide and silver nitrate as precursors. The photodegradation of amlodipine besylate shows that Ag-TiO_2 exhibits much higher photocatalytic activity compared to pure TiO_2: reaching 100 % for only 100 min, while it is only 61 % for 120 min in the presence of pure TiO_2 [98].

Modification of band-gap energy is another strategy in order to extend light absorption of TiO_2 into the visible region by downward shift of *cb* or upward shift of *vb*. It can be achieved by doping with metal and non-metal element, respectively. Generally, it rebuilds the *cb* and *vb* and narrows the band-gap energy [99].

The unoccupied *cb* of TiO_2 consists Ti 3d, 4s, 4p orbitals whereas the occupied *vb* contains O 2p orbitals. The lower position of the *cb* is dominated by Ti 3d orbital. Metal doping is responsible for creating an impurity level on the *cb* in replacement of Ti as shown in Fig. 3.9 a. However, doping with non-metal element localizes a new energy level (such as C, S, or N 2p states) in the *vb* (Fig. 3.9 b) [14,100]. The resultant intermediate energy level promotes visible-light absorption by acting as either an electron acceptor or a donor.

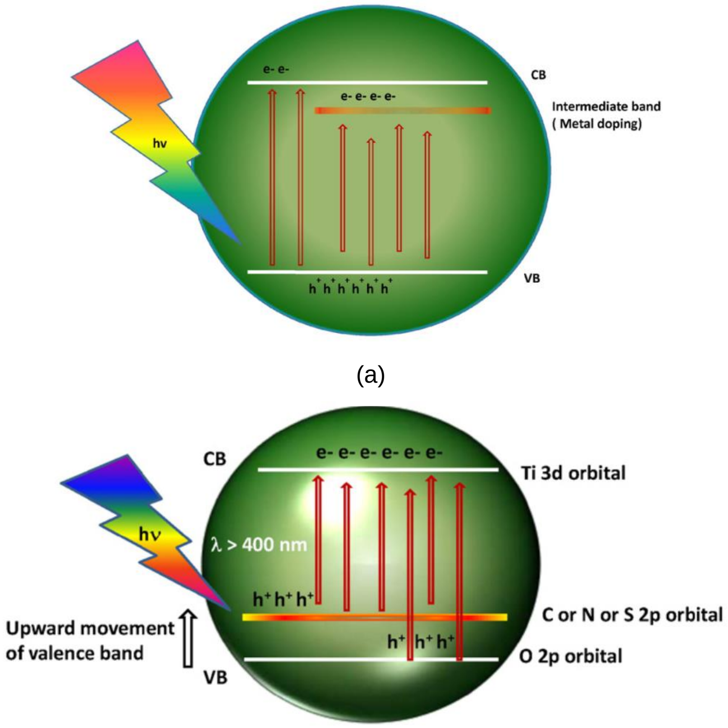

(a)

(b)

Figure 3.9. Formation of localized energy levels in the band-gap due to metal (a) and non-metal (b) doping into TiO_2 photocatalyst [78].

Copious efforts have been devoted to modify TiO_2 photocatalyst by doping with metal and non-metal elements. For instance, *Karafas and workers* used metal-doped TiO_2 (Mn-, Co- and Mn/Co-) to degrade indoor/outdoor pollutants for air quality improvement. The doping with metal induces a slight shift of band-gap energy from 3.1 eV for the undoped TiO_2 to 3.0 eV for Mn-TiO_2, Co-TiO_2 and Mn/Co-TiO_2. The main contribution in narrowing band-gap energy is due to the Co(II) 3d orbitals in the *cb*. The percentage of photocatalytic degradation of CH_3CHO over Mn/Co-TiO_2 is significantly higher (74 %) than with undoped TiO_2 (13 %) under visible-light irradiation, indicating that the metal doping significantly accelerates the photocatalytic degradation of organic pollutants [101]. In 2020, *Elmehasseb and co-workers* modified TiO_2 with Zn via sol-gel method. The optical properties was extremely enhanced by reducing the band-gap energy from (3.2 eV) for TiO_2 to (2.5 eV) for Zn-TiO_2. The photodegradations of *MB* (dye) and ciprofloxacin (antibiotic) and toxic Cr(VI) from wastewater reveal excellent results under visible illumination [102].

In addition, several non-metal elements, such as N, C, S, and B, have been incorporated into the TiO_2 crystal structure in order to enhance visible-light absorption of TiO_2 [14,103]. *Zhang et al.* synthesized B-TiO_2 via traditional hydrothermal method by using titanium tetrachloride and boric acid as starting materials. Boron doping can increase the specific surface area and promote a clear red-shift phenomenon in the optical response of the TiO_2. B-TiO_2 shows photocatalytic degradation of gaseous benzene under visible irradiation within 70 min [104]. *Li and fellow workers* reported S-TiO_2 by using sol-gel method. The S-TiO_2 catalyst reveals a better photocatalytic degradation of pyrimethanil fungicide under visible irradiation compared to the undoped one, indicating the important role of sulfur doping in narrowing the band-gap energy of TiO_2 from 3.11 eV to 2.94 eV [105].

However, doping with S requires much energy to incorporate it into the O site of TiO_2 crystals because of its large ionic radius. Therefore, *Asahi et al.* suggested that N is a most promising dopant, owing to its atomic size comparable to that of oxygen and its p states contribute to the narrowing band-gap energy by mixing with O 2p [14].

Various techniques have been used to prepare N-TiO_2 such as hydrolysis [106], co-precipitation [19], sputtering [107], ion implantation [108], ball milling [109], wet impregnation [110], sol-gel [111], hydrothermal [112], and solvothermal [113] methods as well as oxidation of titanium nitride [12]. Generally, ammonia, hydrazine, NO_2, tert-butylamine, triethylamine, and urea are used as N sources [3]. Table 3.2 shows the results of various preparation methods of N-TiO_2 under different circumstances.

Table 3.2. Comparison of several N-TiO_2 photocatalyst.

Circumstances	*Cheng et al.* [20]	*Gurkan et al.* [110]	*Cheng et al.* [114]	*Abdelhaleem et al.* [115]
Method	Sol gel	Wet impregnation	Hydrolysis-precipitation	Sol gel
N source	Ammonium-chloride	Urea	Ammonia water	Urea
Band-gap energy	2.85 eV	2.70 eV	2.28 eV	2.75 eV
Light source	Visible	Sunlight	Visible	Visible LED
Pollutant	Rhodamine B	Cefazolin	Phenol	4-chlorophenoxy-acetic acid
Degradation efficiency	90.3 % for 2 h	80 % for 0.5 h	65.3 % for 2 h	100 % for 6 h

Suwannaruang and co-workers reported the synthesis of nanorice N-TiO_2 photocatalysts via hydrothermal method. The N-TiO_2 samples consisted of only anatase phase because nitrogen dopant in TiO_2 restrained the phase transformation from anatase to rutile. The band-gap energies of the synthesized N-TiO_2 showed a small shift to lower energy (3.07 eV - 3.18 eV), compared to pure anatase TiO_2 (3.20 eV). They found that an increase of the nitrogen content could enhance the production of hydroxyl radicals and accelerate the photodegradation of paraquat under UV- and visible-light irradiation [112,116].

Sanchez-Martinez and co-workers also prepared N-TiO_2 by co-precipitation method, using ammonium solution as nitrogen precursor. They obtained a slight shift of absorption edge of TiO_2 into the visible region (3.09 eV - 2.94 eV). The results showed an impressive photocatalytic degradation of *RhB* (99.2 %) under a 540-min visible-light irradiation [19].

Co-doping is another ideal solution to improve the absorption edge of TiO_2. Due to a synergistic effect between two or more dopants, co-doping materials show a higher visible-light absorption than single-doped TiO_2, which can efficiently increase the photocatalytic activity. Co-doping can be possible in forms of different metal elements, non-metal elements, or metal and non-metal elements as co-dopants [74].

Giannakas et al. reported the preparation of B/N-TiO_2 and B/N/F-TiO_2 photocatalyst for simultaneous Cr(VI) reduction and benzoic acid oxidation. UV-Vis diffuse reflectance spectra show a narrowing of the band-gap energy for all doped samples (3.08 eV - 2.91 eV), compared to the undoped TiO_2 (3.18 eV). As a consequence, the photocatalytic activities of B/N-TiO_2 and B/N/F-TiO_2 catalysts exhibited higher reduction and oxidation rates than N-TiO_2 and undoped TiO_2 catalysts did [117]. *Mancuso et al.* synthesized Fe/N-TiO_2 by metal and non-metal co-doping, using sol-gel method with titanium(IV) isopropoxide, urea and iron(II) acetylacetonate as precursors. The as-prepared catalysts (Fe/N-TiO_2) displayed a narrower band-gap energy (2.7 eV) than those of Fe-TiO_2 (2.8 eV) and N-TiO_2 (2.9 eV). The photodegradation of acid orange 7 azo dye and its mineralization under visible-light illumination for 60 min were about 90 % and 83 %, respectively [118].

Gao et al. prepared Ag/N-TiO_2 via hydrothermal method with various Ag concentrations. It was found that the photocatalytic performance of Ag/N-TiO_2 was affected by the amount of Ag-loading. The photodegradation of *RhB* initially increased with the increasing Ag loading then fell down after optimum Ag-loading. The optimum Ag concentration was found at 0.92 mol % with the photocatalytic degradation of *RhB* was about 55 % within a 240-min visible irradiation [119]. *Gaidau et al.* synthesized Ag/N-TiO_2 grains by using electrochemical method.

The photocatalytic experiments with orange II dye demonstrated the activities of TiO_2 under visible light can be improved by the synergistic effect of N doping and Ag modification [120]. *Sun and co-workers* successfully fabricated Ag/N-TiO_2 catalysts via an in situ calcination procedure, with titanium nitride and silver nitrate as starting materials. The catalysts revealed an enhanced light absorption and a red shift of the optical edge compared to pure TiO_2 and N-TiO_2. Under visible-light irradiation, a superior *MB* degradation over Ag/N-TiO_2 was also found compared to N-TiO_2 [96].

Yang et al. reported the preparation of a hybrid Ag/N-TiO_2 photocatalyst via a supercritical solvothermal process in ethanol fluid. The catalyst showed that antibacterial activities were much higher under visible-light irradiation than in dark, against a variety of bacteria such as *Acinetobacter baumannii, Staphylococcus aureus, Escherichia coli, Pseudomonas aeruginosa*. For instance, the mortality of *Escherichia coli* in the presence of the catalyst reaches to almost 40 % and 100 % under dark and visible light for 30 min, respectively [121]. *Dziedzic and fellow workers* also published the antibacterial properties of Ag/N-TiO_2 coating on glass, prepared by direct current reactive magnetron sputtering. The microbiological test against *Staphylococcus aureus* revealed the maximum percentage of reduction of 55.1 % after a one-hour incubation under UV light [122].

3.7 Photocatalytic assessment

In general, there are two approaches used to assess the photocatalytic efficiency of catalyst. Investigations of degradation percentage, and rate, as well as mineralization of a model compound have been usually presented in many papers. Another possible way is the application of chemical probes to monitor the *ROS* production [123].

In the photocatalytic processes, the choice of an organic model compound is one of the crucial steps in order to evaluate the performance of the photocatalyst. Several features have to be taken into account, such as solubility, *pH*-dependence, and light sensitivity. *RhB* [19,20], *MB* [12,21], *MO* [22] and eriochrome black-T [23] have been extensively used to study the photocatalytic efficiency.

Marques and co-workers investigated the photocatalytic activity of N-TiO_2 (prepared by sol-gel method with urea as the nitrogen source) in *MB* solution. The results showed that the catalysts were able to decompose the *MB* about 95 % and 65 % under UV- and visible-light irradiation, respectively [12]. *Sacco et al.* reported that under visible light, up to 97 % mineralization of *MB* was achieved in the presence of N-TiO_2 catalyst prepared by direct hydrolysis of titanium(IV) isopropoxide with ammonia. Similar trends were also observed for *MO* decolorization with the initial concentration of 9 mg dm^{-3} [22].

However, those dye compounds can only be used for such a purpose with care because the process involves competing light absorptions by the dyes and the catalyst. Dyes absorb a significant fraction of the light used to excite the catalyst. Hence, the initial concentration of the dyes must be kept at a low level. Additionally, the dyes may function as sensitizers in the visible range, which, however, can increase the photocatalytic activity. Therefore, to avoid both inner filter effect and possible sensitization, other organic model compounds must be applied that do not absorb at the irradiation wavelengths [123].

Beside dyes, some chemical emerging contaminants such as 2-chlorophenol, ethylparaben, diclofenac, 4-acetamidophenol, 1,4-HQ, and others are commonly applied as a model compound for photocatalytic investigation of TiO_2-based catalysts because they are hazardous, colorless, and do not absorb light [124,125].

Nguyen et al. evaluated the removal of diclofenac by using a sub-merged photocatalytic membrane reactor with suspended N-TiO_2 (sol-gel method) under visible-light. The result indicated that higher initial concentration reduced the efficiency of the process. The 5 mg dm^{-3} of initial concentration was observed as an optimum degradation rate of diclofenac with a value of 0.0023 mg dm^{-3} min^{-1} [126]. *Rajoriya and co-workers* investigated the degradation of 4-acetamidophenol in the presence of N-TiO_2 fabricated via ultrasound assisted sol-gel process. The results showed the degradation percentages of 4-acetamidophenol: 63.3 % ($k = 6.5\times10^{3}$ min^{-1}) and 28.3 % ($k = 2.1\times10^{3}$ min^{-1}) under UV- and visible-light illumination, respectively [127].

1,4-HQ is one of the promising organic model compounds for testing the photocatalytic degradation because of its widespread application in human and industrial activities. It can be used as a developing agent in pharmaceutical, personal care products, dye intermediates, etc. It is present in the medical products, cosmetic formulations of products such as skin lightening, finger nails coating, and hair dyes [128]. On the other hand, 1,4-HQ can also appear as intermediate metabolites, or a degradation product generated by transformation of several aromatic compounds, particularly from phenol and several benzene derivatives. The formation of 1,4-HQ at early stages of phenol oxidation increases the toxicity of phenol wastewaters, showing that these compounds were more toxic and less degradable than the original pollutant.

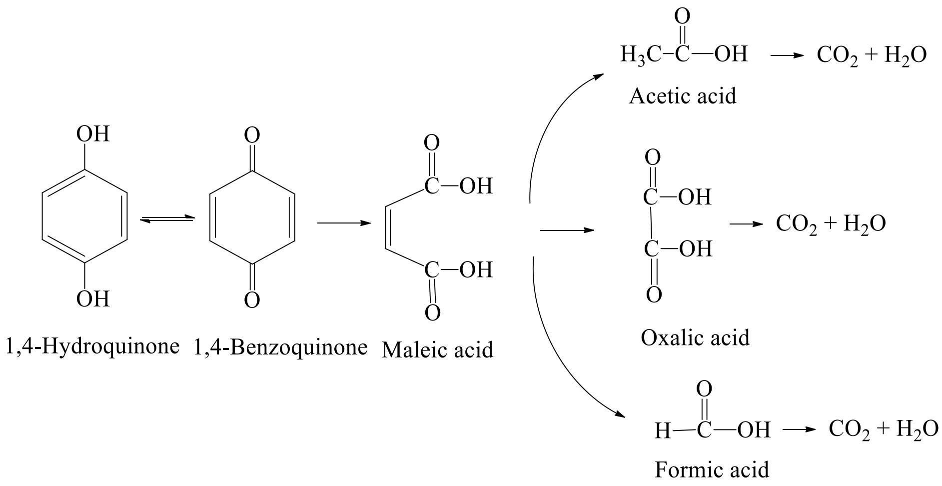

Figure 3.10. Proposed mechanism of 1,4-HQ degradation.

In the photocatalytic reaction, however, 1,4-HQ can be degraded into several compounds such as acetic acid, oxalic acid, and formic acid, then further mineralized to CO_2 and H_2O as shown in Fig. 3.10 [129–132]. *Houndedjihou and co-workers* reported the investigation of 1,4-HQ photodegradation by using thin layer of Degussa P25 TiO_2. The photocatalytic study showed that about 57 % of 1,4-HQ was degraded under UV-A illumination for 300 min. Two intermediate by-products have been observed at the wavelength of 246 nm and 256 nm, which could be assigned to 1,4-benzoquinone and (probably) hydroxyl-benzoquinone, respectively. The existing benzoquinone (even at the initial time), is due to a reversible reduction-oxidation reaction of 1,4-HQ occurring in solution [125].

Furthermore, *ROS* ($^{\bullet}$OH and $^{\bullet}O_2^{-}$) are well known as primary intermediates of photocatalytic reactions. The evaluation of these species, both their quantification and kinetics are important in terms of understanding the photocatalytic mechanisms, enhancing the efficiency, and utilizing the various technologies for practical applications [133].

Paramagnetic resonance, UV/Vis absorption spectroscopy, fluorescence, and other methods have been developed in order to identify *ROS* formation. However, fluorescence probing is one of the favorable methods, due to its high sensitivity to measure at low concentrations. This method is based on the appearance of a fluorescent product in the reaction of the molecular probe with *ROS*. At a specified wavelength, the excitation of the reaction product leads to a characteristic emission, which can be measured by spectrofluorometry [134].

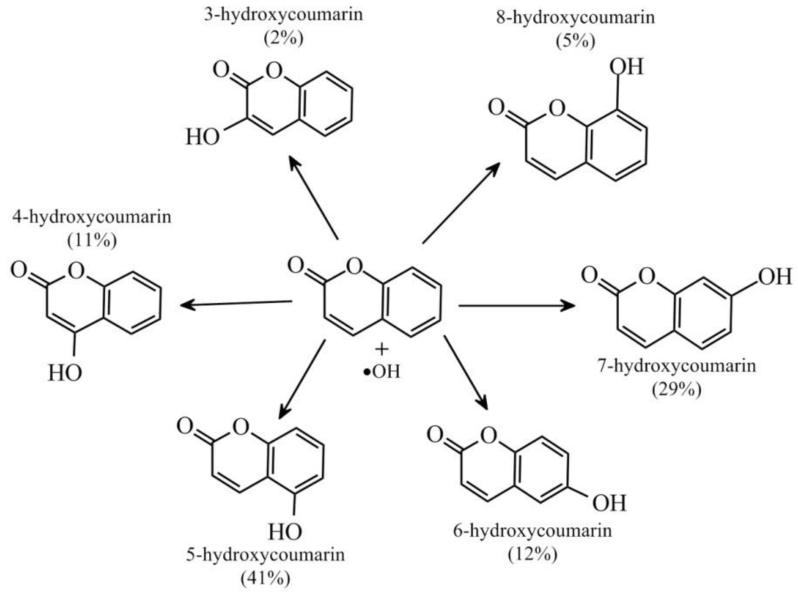

Figure 3.11. Product distribution of the reaction of coumarin with hydroxyl radical.

Numerous compounds, such as terephthalic acid and sodium terephthalate [135,136], coumarin [137–139], coumarin-3-carboxylic-acid [140,141], and ninhydrin [142], have been successfully applied in the quantification of hydroxyl radicals. Nevertheless, coumarin is found to serve as an adequate probe for the direct assessment of $^{\bullet}OH$. The amount of this radical was estimated by measuring the fluorescence of the 7-OHC product, the yield of which was 29 % of the hydroxyl radicals reacted with coumarin. The product distribution of this reaction is shown in Fig. 3.11 [138,139].

The main advantage of this method is its simplicity, sensitivity, reproducibility and accuracy. However, some parameters should be taken into account, such as the *pH*-dependence of the fluorescence, formation of other hydroxylated products in addition to the quantifiable ones, and degradation of the product to be measured under specific operating conditions [143].

Furthermore, another important *ROS* is superoxide anion radical produced in the reaction between photo-generated electron and oxygen in the photocatalytic system. This type of *ROS* is easily protonated to $^{\bullet}OOH$, although superoxide anion radical still predominates in aqueous media [143].

Various compounds have been tested as chemical probes to quantify superoxide anion radical in various *AOP*s, including nitroblue tetrazolium, 2,3-nis(2-methoxy-4-nitro-5-sulfophenyl)-2H-tetrazolium-5-carboxanilide, and methoxy cypridina luciferin analog. However, luminol is the most widely used as a probe for superoxide anion radical by producing the chemiluminescent 3-aminophtalate (Fig. 3.12) [143].

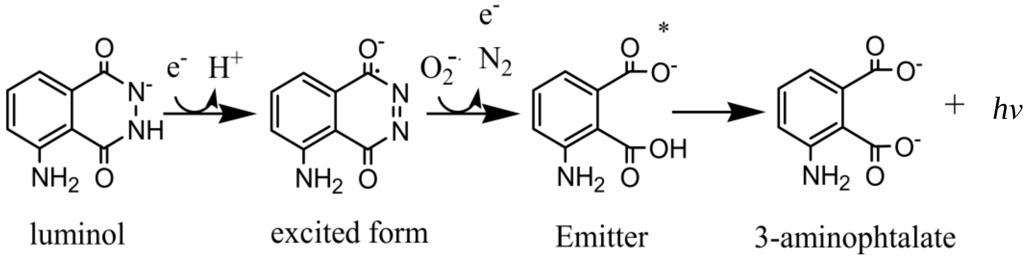

Figure 3.12. Reaction of luminol with $^{\bullet}O_2^{-}$ [143].

Typically, luminol is first converted into an intermediate radical by a one-electron oxidation, normally mediated by H_2O_2. Then the luminol radical reacts with superoxide anion radical to form an electronically excited

3-aminophthalate. Luminescence occurs when the 3-aminophthalate decays to the ground state [144]. Furthermore, the oxidation of luminol in the presence of light is a complex, multistep process and depends on several factors such as *pH*, temperature, metal catalyst, hydroxide ions, and reactive species present in solution that interact with luminol [145].

4. Experimental

4.1 Materials

Titanium(IV) isopropoxide ($Ti[OCH(CH_3)_2]_4$, 98 %) and titanium(IV) iso-butoxide ($Ti[OC(CH_3)_3]_4$, 98 %) were purchased from Acros Organic (China) and used as titanium precursor. Urea (CH_4N_2O) and ammonium hydroxide (NH_4OH, 25 %) were used as nitrogen source (pure reagent grade) and obtained from Scharlab Hungary Kft (Hungary). Nitric acid (HNO_3, 65 %) was supplied by VWR international (Hungary). Silver nitrate ($AgNO_3$) and ethanol were purchased from Forr-Lab Kft. (Hungary) and Molar Chemical Kft. (Hungary), respectively The two organic model compounds, coumarin ($C_9H_6O_2$) and 7-hydroxycoumarin ($C_9H_6O_3$, 99 %) were obtained from Carlo Erba Reagent (Italy) and Sigma-Aldrich (Hungary), respectively. 1,4-hydroquinone ($C_6H_6O_2$, ≥ 99 %) was purchased from Sigma-Aldrich (Hungary). Barium sulphate ($BaSO_4$) was purchased from Reanal (Hungary). Freeze-dried bacteria (for Lumistox bacteria test) were provided by Hach Lange GmbH (Germany).

High purity water used in these experiments was double distilled and then purified with a Milli-Q system. Compressed air or argon bubbling was introduced into the reaction mixtures from gas bottles.

4.2 Preparation of N-TiO_2

4.2.1 NT-A preparation

The preparation of N-TiO_2 (NT-A) was realized by using a previously published method [19] with numerous modifications. It was conducted by various synthesis temperatures, dosing order steps, calcination time and temperature.

The synthesis temperature was adjusted to 0, 10 and 25 °C during the preparation. For the first dosing order, a volume of 2 cm^3 of titanium(IV) isopropoxide (TTIP) was drop-wise added into 50 cm^3 of distilled water, while continuously stirring for 10 min. Subsequently, 20 cm^3 of nitric acid (65 %) was added to this white suspension, and it turned into a transparent solution. Afterward, ammonium hydroxide (25 %, 85 cm^3) was slowly added in the solution and magnetically stirred for 60 min [19]. The second dosing order was nitric acid, ammonium hydroxide, distilled water, and TTIP.

Furthermore, the precipitate obtained from the final mixture was vacuum filtered and dried at 40 °C for 24 h. Then the dried catalyst was ground and calcined at 450 °C for 30 min in air atmosphere with a heating rate of 2 °C min^{-1} (in a Nabertherm P330 Furnace, Germany). In order to investigate the effects of calcination time on the photoactivity, the catalysts were calcined at 450 °C for 30, 60, 120, and 240 min. In addition, the effect of calcination temperature was also examined at 150, 250, 350, 400, 450, 500 and 650 °C for 30 min (best calcination time). The NT-A catalysts obtained at different calcination temperatures are shown in Attachment as Fig. A4.1.

For comparison, undoped TiO_2 was also prepared by drop-wise addition of titanium precursor into distilled water. The undoped TiO_2 was calcined at 450 °C for 30 min.

4.2.2 NT-U preparation

A volume of 5 cm^3 titanium(IV) isobutoxide (TTIB) was dissolved drop-wise into 50 cm^3 anhydrous ethanol. Furthermore, 3.6 g of urea in 2 cm^3 of NH_4OH was added slowly with vigorous stirring at room temperature for 2 h then increased to 80 ^{o}C for 1 h. Subsequently, a white gel was vacuum filtered and dried at 40 ^{o}C for 24 h [146]. Finally, N-TiO_2 sample (NT-U) was ground and calcined at 450 °C for 30 min (optimum calcination temperature and period) in air atmosphere with a heating rate of 2 °C min^{-1} (Nabertherm P330 Furnace).

4.3 Preparation of Ag/N-TiO_2

Ag nanoparticles were decorated on the surface of N-TiO_2 by using photo-deposition method. Firstly, 0.18 cm^3 solutions of various $AgNO_3$ concentrations (0.2, 2.0, 20, and 200 mM) were diluted to 15 cm^3 with distilled water. Then, 0.36 g of NT-U or NT-A was added into these solutions, followed by 10-min stirring to reach the adsorption-desorption equilibrium. Subsequently, under continuous stirring, the mixture was irradiated by using a UV LED (λ_{max} = 390 nm) for 10 min from a distance of 5 cm [147]. Lastly, the catalyst was dried at 50 °C for 24 h. The obtained catalysts are denoted as Ag/NT-U*x* and Ag/NT-A*x*, where *x* (*x* = 0, 10^{-7}, 10^{-6}, 10^{-5} and 10^{-4} mol g^{-1}) represents the Ag/NT ratio. The color of the synthesized catalysts changed from light yellow to gray upon increasing the Ag concentration.

In order to estimate the amount of Ag nanoparticles attached on the surface of the catalysts, the concentrations of Ag in the solution initially (i.e., before the adsorption process), after the adsorption, and at the end of the UV irradiation were measured by using inductively coupled plasma optical emission spectroscopy (ICP-EOS, Spectroflame Modula, SPECTRO) under Ar plasma.

4.4 Characterization

The morphology and elemental analysis of the catalysts were investigated by using an Apreo SEM (ThermoFisher Apreo S scanning electron microscope) equipped with Octane Elect Plus EDX (AMETEK) was used at 5.0 kV for imaging and 25.0 kV for elemental analysis. A Talos F200X G2 instrument (Thermo Fisher), equipped with a field-emission gun and a four-detector Super-X energy-dispersive X-ray spectrometer was used at 20.00 kV for transmission electron microscopy (TEM) and elemental analysis. TEM and high-angle annular dark-field (HAADF) images were collected for both structure analyses and elemental mapping.

Thermal analysis was carried out by using two different instruments. Thermogravimetric analysis (TG) and differential thermal analyses (DTA), a Derivatograph-C type thermoanalytical instrument (Hungarian Optical Works) was applied in the temperature range of 20 °C - 1000 °C, with 5 °C min^{-1} heating rate and dynamic synthetic air atmosphere, using open ceramic crucibles. Additionally, TG-DSC (Differential scanning calorimetry) analysis was carried out by using Netzsch STA 409 CD simultaneous thermoanalytical equipment, open ceramic crucible heated in dynamic Ar flow, 20 °C - 1015 °C, 10 °C min^{-1}.

Raman analysis was performed by using a Bruker Senterra dispersion Raman micro-spectroscope, equipped with a 532-nm excitation laser operated at 2 mW, 10x optical magnification for visual images.

Fourier transform infrared spectroscopy-attenuated total reflection (FTIR-ATR) measurements were carried out by using a BRUKER Vertex 70 type spectrometer with a single reflection Bruker Platinum diamond ATR adapter. The spectra of the ground samples were recorded at a resolution of 2 cm^{-1}, with a room temperature DTGS detector by averaging 512 scans.

The specific surface area was determined by nitrogen adsorption/desorption isotherms measured with a Micromeritics ASAP 2000-type instrument on samples (weight ≈ 1.0 g) previously outgassed in vacuum at 160 ^{o}C.

The surface areas of the samples were determined by the BET (Brunauer-Emmett-Teller) method from the corresponding nitrogen adsorption isotherms.

The crystal structures of the catalysts were examined by using XRD (with a Philips PW 3710 type powder diffractometer) with a Cu-Kα radiation source (λ = 1.5405 Å). Diffraction peaks were recorded from 10° to 70° and used to determine the structure of catalysts. The crystallite size values were calculated by using the Scherrer equation [148].

Diffuse reflectance spectra (DRS) were recorded on a luminescence spectrometer (PerkinElmer, USA) equipped with an integrating sphere. The band-gap energy was calculated by using Tauc plot of the Kubelka-Munk function [149]. The details of the calculation are described in Text A4.1 of the Attachment.

4.5 Reactor and photocatalytic experiments

Photochemical experiments were carried out by using a laboratory-scale reactor with a volume of 50 cm^3, (Figs. 4.1 - 4.2) and in all experiments air or argon (Ar) was continuously bubbled into the reaction mixture. The flow rate of gas was 20 dm^3 h^{-1}.

UV (λ_{max} = 390 nm; 60 W, light intensity = 7.6 mW cm^{-2}) and visible (λ_{max} = 453 nm; 7 W) LEDs were used as light sources (Fig. A4.2). The visible LEDs were located on one (light intensity = 23 mW cm^{-2}) or both sides (light intensity = 90 mW cm^{-2} for each side) of the reactor with a distance of 10 or

3 cm, respectively. The change of position and distance of the visible LEDs was carried out in order to enhance the light intensity. The optimum light intensity was obtained by the lamps arrangement with two-side positions.

The temperature of the reaction mixture was relatively stable during the illumination, increasing by only 2-3 °C. It resulted in a negligible effect to the rate of photochemical and thermochemical reactions.

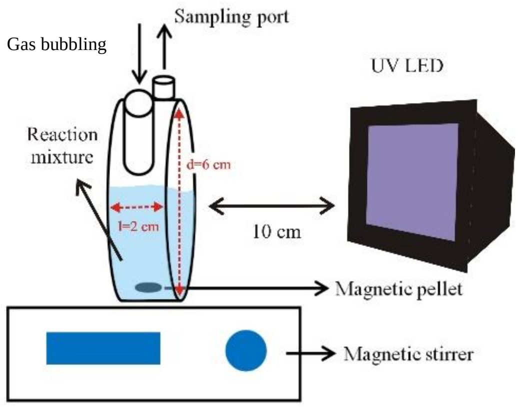

Figure 4.1. Schematic illustration of the lab-scale quartz glass reactor and its arrangement in the setup for photocatalytic experiments under UV LED.

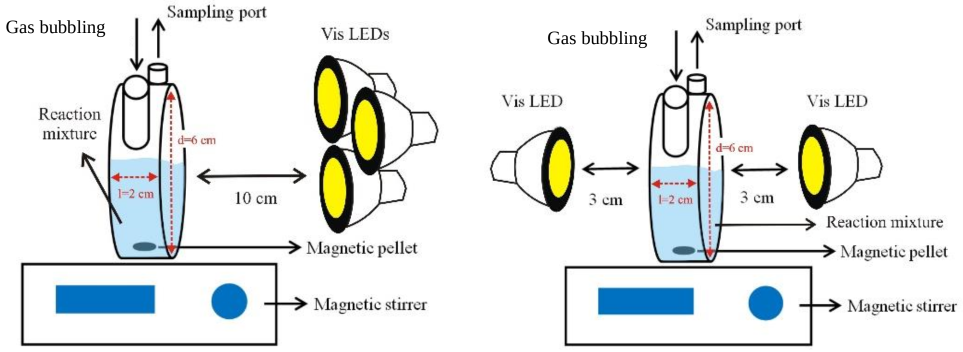

(a) (b)

Figure 4.2. Illustration of photocatalytic reactor under Vis LED with (a) first and (b) second arrangements.

Initially, 50 mg of catalyst was placed in 10 cm^3 distilled water and mixed under sonication for 30 min, (to disperse the catalyst particles) followed by stirring overnight to homogenize the particles. Hydroxyl radicals might be formed during sonication [150]. However, they would recombine in the absence of scavenger. Afterwards, 40 cm^3 solution of organic substrate (coumarin or 1,4-HQ) was added into the suspension and left in the dark for 30 min to establish an adsorption-desorption equilibrium at room temperature. The initial concentrations of coumarin and 1,4-HQ were 0.8×10^{-4} M and 2×10^{-4} M, respectively. The concentration of the catalyst was 1 g dm^{-3} in all experiments.

Before and during the irradiation, 3 cm^3 samples were taken through a septum with a syringe and filtered by a Millipore Millex-LCR PTFE 0.45 µm membrane filter.

4.6 Analytical measurements

In this work, coumarin was used as scavenger of hydroxyl radicals generated during the photoreaction, producing strongly emissive 7-hydroxycoumarin (7-OHC) [139]. The emission of 7-OHC (λ_{ex} = 332 nm and λ_{em} = 453 nm) was determined by spectrofluorometer (PerkinElmer LS50B).

The actual coumarin concentration was calculated from absorption spectra. The molar absorption coefficient (ε) of the 7-OHC compound at 277 nm was significantly lower than that of coumarin, therefore at low concentrations ($c = 10^{-5}$ M at lower concentrations, 7-OHC is formed about 10^{-7}-10^{-8}), the resulting 7-OHC did not significantly alter the light absorption. No spectrum distortion appeared at the maximum absorption of the 7-OHC (λ = 324 nm) (Fig. A4.3). Then the absorbances of coumarin were measured by using a UV-Vis spectrophotometer (Scinco S-3100) (Fig. A4.4) and the degradation rate constant (k) was determined by pseudo-first order kinetics. The quantum yield was estimated according to a previously reported method as described in Text A4.2 [151].

The concentration of 1,4-HQ was analyzed by using a luminescence method due to its intensive emission at λ_{em} = 330 nm (λ_{ex} = 288 nm). In addition, a high performance liquid chromatograph (HPLC, Shimadzu) was also applied for monitoring the photodegradation of 1,4-HQ by using a C18 column (Phenomenex Kinetec, 3.0×100 mm, 2.6 µm particle sizes) for separation, and a UV detector at

246 nm and 288 nm wavelengths. The mobile phase consisted of methanol and water (5/95 %, v/v), and its flow rate was 0.2 cm^3 min^{-1} [152].

The degradation efficiency (*D(t)*, %) was calculated by using Eq. 4.1.

$$D(t)(\%) = \frac{c_0 - c_t}{c_0} \quad (4.1)$$

where c_0 and c_t are the initial and actual concentration of the organic compound, respectively [153].

The mineralization process was measured by using a total organic carbon analyzer (TOC-L, Shimadzu).

4.7 Antibacterial study

The antibacterial effect was measured by using *Vibrio fischeri* luminescent bacteria. The sample preparation for antibacterial study is described in the Text A4.3 [154]. The luminescent intensity of *Vibrio fischeri* was detected by a Toxalert 100 device. The inhibition percentage of bioluminescence could be achieved by Eq. 4.2.

$$Relative\ decomposition_t(\%) = \frac{I_{reference(t)} - I_{sample(t)}}{I_{reference(t)}} \times 100 \quad (4.2)$$

where $I_{reference(t)}$ is the emission intensity of the reference or blind sample and $I_{sample(t)}$ is the emission intensity of the actual sample.

5. Result and Discussion

5.1 NT-A catalyst

The main objective of this study is to synthesize catalysts being active under visible illumination. In the first stage of experiments were carried out to find the optimum dosing order, synthesis temperature and calcination time of NT-A (calcined at 450 °C) from the viewpoint of photoactivity.

The photocatalytic activity of catalysts were assessed by measuring the generation of hydroxyl radicals under visible and UV light. Hydroxyl radical formation is usually considered as a key process characterizing the photocatalytic activity [112]. It is well known that hydroxyl radical is one of the highly *ROS* in the photocatalysis that attacks the organic contaminants, resulting in the degradation of these compounds [155,156]. Coumarin was used as the scavenger of hydroxyl radical and the concentrations of 7-OHC formed were calculated from the emission data at 453 nm by using a calibration curve (Fig. A5.1), and the initial rates (v_0) were determined from the slope of linear regression equation obtained from 7-OHC concentration as a function of irradiation time. The concentration of 7-OHC was found to be proportional to the amount of hydroxyl radical produced.

5.1.1 Effect of dosing order and synthesis temperature

In this section, two different dosing orders of the NT-A preparation were applied at controlled temperature (0, 10, 25 °C) in order to investigate their effect on the photoactivity. The first dosing order is designated as TTIP-H_2O-HNO_3-NH_4OH, while the second one as HNO_3-NH_4OH-H_2O-TTIP. Fig. 5.1 reveals that at all synthesis temperatures, the photocatalytic 7-OHC formation with NT-A prepared by using the second dosing order was significantly higher compared to those achieved with NT-A synthesized by the first dosing order, which was negligible under visible irradiation within 240 min. In addition, the 7-OHC formations with undoped TiO_2 and Degussa P25 TiO_2 were relatively slow with the v_0 of 0.4×10^{-10} M min^{-1} and 0.2×10^{-10} M min^{-1}, respectively.

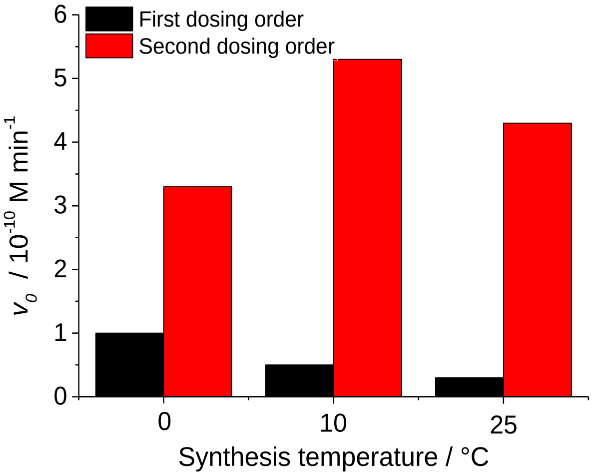

Figure 5.1. Effect of dosing order and synthesis temperature on 7-OHC formation. c_0(coumarin) = 0.8×10^{-4} M, c(catalyst) = 1 g dm^{-3}, Vis LED (1st arrangement), 20 dm^3 h^{-1} air

The dosing order of the preparation steps significantly affected to the photoactivity of NT-A catalyst. As we can see in the first dosing order (TTIP-H_2O-HNO_3-NH_4OH), titanium precursor was firstly hydrolyzed in water to form $Ti(OH)_4$, then dissolved in the strong acid (HNO_3). In this step, the precipitate $Ti(OH)_4$ converted into ionic form (Ti^{4+}) in acidic solution. Afterwards, further hydrolysis reaction occurred during NH_4OH addition and turned to titanium precipitate. As a product of hydrolysis reaction, it is believed that the presence of acid solution will delay the hydrolysis reaction producing $Ti(OH)_4$ precipitate. It might be due to the neutralization reaction between HNO_3 and NH_4OH in the first stage of reaction before precipitation of titanium hydroxide. In other words, it takes more time for the $Ti(OH)_4$ nuclei to form. The initial acid concentration will also influence the particle size and morphology of the titanium dioxide by affecting the nucleation and crystal growth [157].

However, in the case of the second dosing order (HNO_3-NH_4OH-H_2O-TTIP), the hydrolysis reaction of the titanium precursor occurred in the base solution. An excess of NH_4OH was added to the HNO_3 solution, producing basic buffer. This procedure might induce a faster hydrolysis reaction compared to that in the first dosing order, affecting the nucleation, crystal growth, and yield of titania produced.

The effect of synthesis temperature (0, 10 and 25 °C) indicates that the photoactivity of photocatalyst prepared by the first dosing order increased at lower synthesis temperature. The optimum 7-OHC formation was obtained at the lowest temperature (0 °C) with the v_0 of 1.0×10^{-10} M min^{-1}.

On the contrary, the results obtained be the second dosing order suggest that the photoactivity increased at higher temperature then decreased after an optimum value. The NT-A catalyst prepared at 10 °C demonstrated the highest 7-OHC formation with the v_0 of 5.3×10^{-10} M min^{-1}. The synthesis temperature might control the kinetic mechanisms of hydrolysis reaction of titanium precursor from the molecular level until the nucleation and growth of TiO_2 particles [158]. Furthermore, this optimum synthesis condition (second dosing order at 10 °C) was preferred for the further experiments.

Vaiano et al. [23] reported the preparation of N-TiO_2 at -20 °C to 0 °C, using sol-gel method. It was found that the lower synthesis temperature had a strong effect on the crystallite size and specific surface area. Particularly, the lower crystallite size occurred and the specific surface area was higher at lower temperature. The photoactivities of catalysts prepared at -20 °C were obtained by decolorization of eriochrome black-T; 41 % and 31 % upon UV- and visible-light irradiation (for 210 min), respectively. *Sanchez-Martinez et al.* [19] also proposed the synthesis of N-TiO_2 at room temperature (25 °C), using co-precipitation method. The photoactivity of the catalysts was tested in the *RhB* solution and its degradation efficiencies were 40 % and 99 % for UV- (80 min) and visible-light (540 min) irradiation, respectively.

Afterwards, the photoactivity of NT-A (second dosing order, 10 °C) was evaluated and compared to undoped TiO_2 and Degussa P25 TiO_2 under UV light (Fig. 5.2). According to our results, Degussa P25 TiO_2 exhibited the best photoactivity under UV light, followed by the undoped TiO_2 and NT-A. NT-A exhibited a lower photoactivity than undoped TiO_2 did under UV light, owing to the consequence of modification with nitrogen that may shift the level of the valence band, thereby reducing its oxidative efficiency, and, thus, producing less hydroxyl radicals. The tendencies were in agreement with the coumarin degradation and its quantum yield as shown in Fig. A5.2.

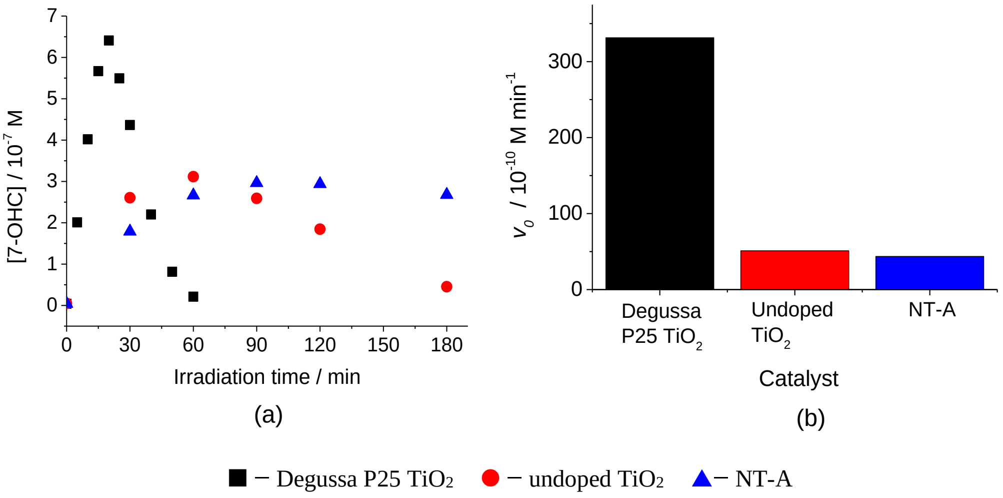
(a)
(b)

Figure 5.2. (a) Concentration and (b) v_0 of 7-OHC formation for the different catalysts under UV light.

c_0(coumarin) = 0.8×10^{-4} M, c(catalyst) = 1 g dm^{-3}, UV LED, 20 dm^3 h^{-1} air

5.1.2 TG-DTA analysis

Thermogravimetry and differential thermal analysis were used to detect the changes during the heat treatment of the catalysts. Fig. 5.3 shows the derivatograms of dried undoped TiO_2 and NT-A powders.

The initial masses of undoped TiO_2 and NT-A were 153.5 mg and 153.6 mg, respectively (100 %). As shown in Fig. 5.3 a, the TG and DTG curves of the undoped TiO_2 indicate a significant weight loss in the range of 25-302 °C. During the preparation, titanium tetrahydroxide was formed upon hydrolysis of the titanium precursor. Under heating (25-302 °C), pure titanium dioxide (106.4 mg (69.3 %), 1.32 mmol) and water molecules (47.1 mg (30.7 %), 2.6 mmol) were formed as shown in Eqs. 5.1-5.2. These values clearly indicate that 2 moles of H_2O were removed during heating treatment at 25-302 °C. No significant weight-loss were observed at higher temperatures.

$$\mathrm{Ti[OCH(CH_3)_2]_4 + 4H_2O \rightarrow Ti(OH)_4 + 4\,[HOCH(CH_3)_2]} \qquad (5.1)$$

$$\mathrm{Ti(OH)_4 \xrightarrow{\text{Heat treatment}} TiO_2 + 2H_2O} \qquad (5.2)$$

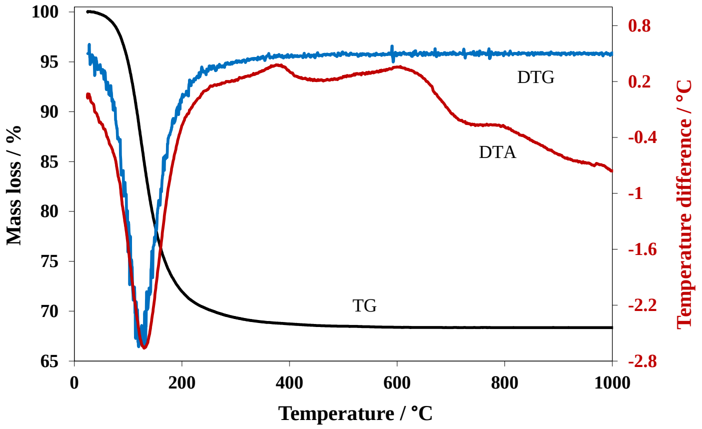

(a)

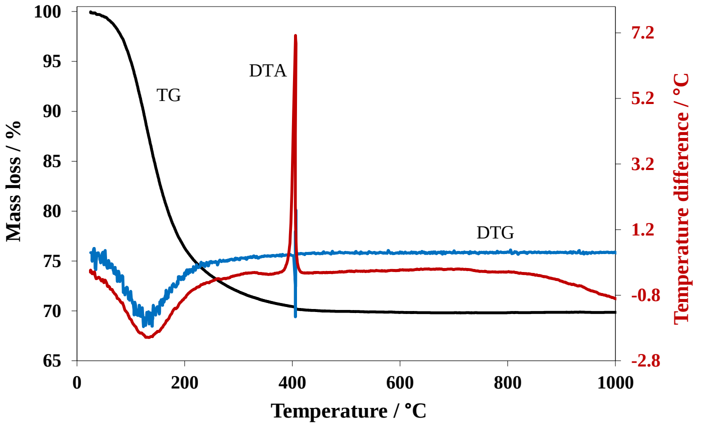

(b)

Figure 5.3. TG-DTA curve of (a) undoped TiO_2 and (b) NT-A catalysts.

Starting sample = the sample dried at 40 °C for 24 h in the preparation step

Furthermore, the TG and DTG curves of NT-A illustrate a total mass loss of 46.1 mg (30 %) as shown in Fig. 5.3 b. A weight loss of 43.2 mg (28.1 %) was recorded at 25-302 °C due to the removal of water, ammonia, and the remaining organic compounds originating from titanium precursor. A further weight loss of 2.9 mg (1.9 %) at 302-464 °C might be attributed to the evaporation of the residue of absorbed water. There was no weight loss above 464 °C for NT-A.

Additionally, DTA curves of all samples show an endothermic peak below 405 °C, which can be assigned to evaporation of water surface-adsorbed and decomposition of organic compounds. Then low and sharp exothermic peaks at 405 °C are visible in the undoped TiO_2 and NT-A, respectively, which can be attributed to the possible rearrangement of the TiO_2 structure from amorphous to anatase [159]. It is well known that amorphous TiO_2 is thermodynamically metastable, so it can evolve into a crystalline phase under heating treatment. The oxygen in the amorphous TiO_2 releases when it is heated at certain temperature, forming intermediate and water. Furthermore, the TiO_2 structure re-arranges and transforms into anatase [160,161].

Moreover, a small exothermic peak was observed around 600 °C for undoped TiO_2 and negligible for the NT-A sample. The peak around 600 °C is associated with the phase transformation from anatase to rutile [162]. From this point of view, it implies that doping with nitrogen could hinder the transformation of TiO_2 from anatase to rutile at high temperature (around 600 °C). These phenomena are also confirmed by XRD results, which will be discussed in the chapter 5.1.5.1.

5.1.3 SEM morphology

SEM measurements were carried our in order to investigate the effect of morphology on the photoactivity. The results exhibited that all samples (prepared by both first and second dosing orders) mainly contained amorphous microparticles with various sizes within ~ 2-100 µm. The particle sizes are similar to those previously reported by *Gurkan et al.* [110], in the case of which wet impregnation method was applied. The N-TiO_2 catalyst consisted of spherical particles with sizes up to 50-100 µm. Microsheets and nanorice grains were obtained for the morphology of the N-TiO_2 catalyst prepared by hydrothermal method with average lengths of 3.5 µm and 250 nm, respectively [112,163].

Noticeably, the dosing order of the synthesis significantly affected on the surface morphology. A non-hollow structure was obtained by the first dosing order (TTIP-H_2O-HNO_3-NH_4OH) as displayed in Fig. 5.4 a. However, NT-A catalysts prepared by the second dosing order (HNO_3-NH_4OH-H_2O-TTIP) displayed a hollow structure on the surface of catalyst as shown in Fig. 5.4 b.

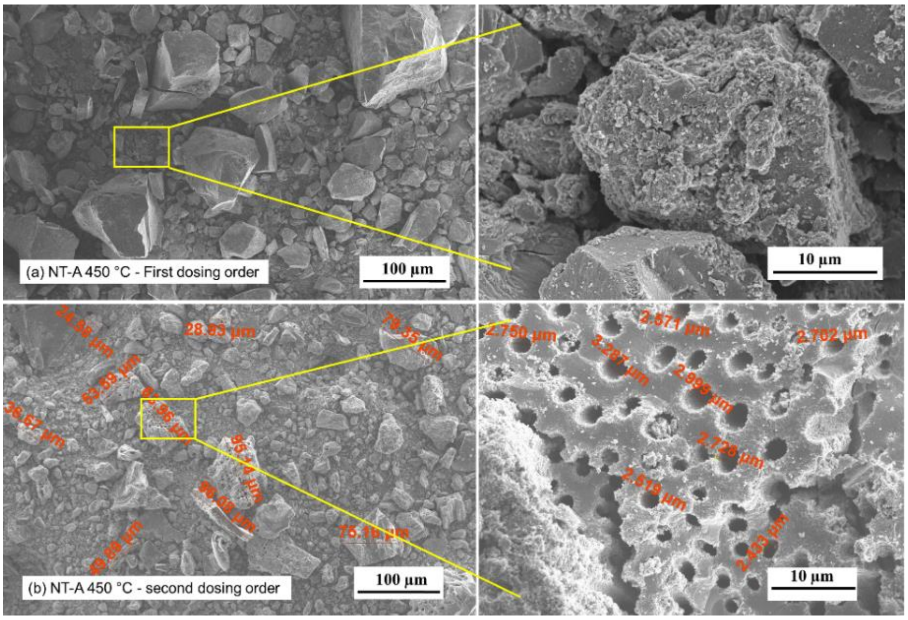

Figure 5.4. SEM morphology of catalysts prepared by (a) first and (b) second dosing order.

Generally, the hollow structure in the second order (HNO_3-NH_4OH-H_2O-TTIP) was formed due to the drop-wise addition of the titanium precursor into the basic solution (NH_4NO_3 << NH_4OH; pH=11). When titanium precursor was slowly dropped into the basic solution, hydrolysis reaction would rapidly occur at the surface of the droplets. The original droplet would be fragmented into many smaller ultrafine drops due to the surface reaction-induced acting force on the droplet and gravitation. Thereafter, the TiO_2 shell layers would be formed on the surface of the ultrafine drops due to the surface hydrolysis reaction, leading to the surface hardening of the drops. Because of the significant density difference between the solid TiO_2 and the liquid titanium precursor, the formed shell-layers turn into a hollow structure as illustrated in Fig. A5.3 [164].

Interestingly, the hollow structures were also observed on NT-A before calcination and in the undoped TiO_2 (450 °C) (Fig. 5.5). The hollow sizes of undoped TiO_2 were similar to those of the NT-A (450 °C) catalyst. Hence, it can be concluded that the formation of pores was not influenced by the nitrogen doping but due to the drop-wise process of the titanium precursor into distilled water (undoped TiO_2) or basic solution (NT-A).

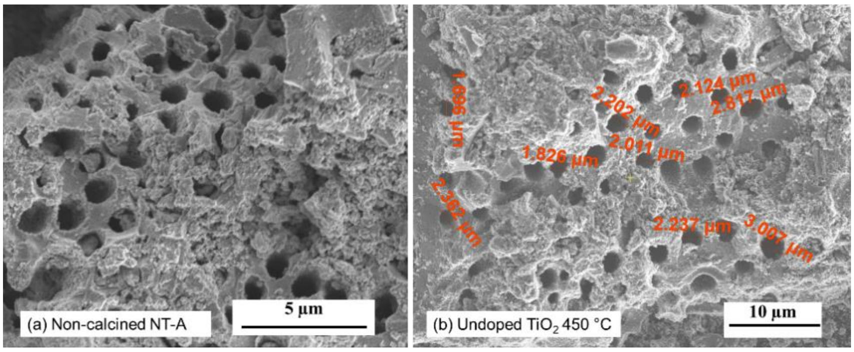

Figure 5.5. SEM morphology of (a) non-calcined NT-A and (b) undoped TiO_2.

The average pore size of undoped TiO_2 (450 ^oC) was stable during the calcination processes, but it increased for the NT-A catalysts. The average pore diameters of NT-A before and after calcination were about 1 and 3 µm, respectively. It is also reported that the calcination process increased the average pore size [19,165,166].

In addition, the hollow surface is an important feature in the photocatalytic performances because the large surface area can improve the adsorption of pollutants compared to the case of non-hollow materials. The surface area can strongly be related to the active sites, which are crucial in trapping photoinduced carriers and prolonging their lifetime [167].

5.1.4 Effect of the calcination time

Most of the previous studies only optimized the calcination temperature, instead of calcination time, e.g., *Sanchez-Martinez et al.* calcined N-TiO_2 (prepared by co-precipitation) at 200, 300, 400, and 500 °C for 2 h [19], *Suwannaruang, et al.* annealed the N-TiO_2 catalyst (synthesized by hydrothermal method) at 300, 400, 500, 550, 600, 650 and 700 °C for 4 h in air atmosphere [116]. Therefore, in this study, the effect of calcination time for NT-A catalyst (synthesis temperature 10 ^oC) was investigated within the range of 30-240 min, while the calcination temperature was kept at 450 °C. Afterwards, the photocatalytic 7-OHC formation was used as indicator to obtain the optimum calcination time.

The results indicated that v_0 of the 7-OHC formation under visible light decreased at longer calcination periods (Fig. 5.6 a). Notably, the decrease within the range of 60-240 min was almost negligible. This phenomenon may be attributed to the loss of some nitrogen during the calcination. The N contents of NT-A catalysts were 5.5; 4.19; 3.86 wt % for 30-, 60-, and 240-min calcination times, respectively. The decrease of nitrogen content above 60-min calcination time was rather slight, strongly correlating with the photoactivity. However, under UV light, the 7-OHC formation of NT-A was relatively stable as shown in Fig. 5.6 b. Therefore, the synthesis temperature of 10 °C and 30-min calcination time were used for further experiments.

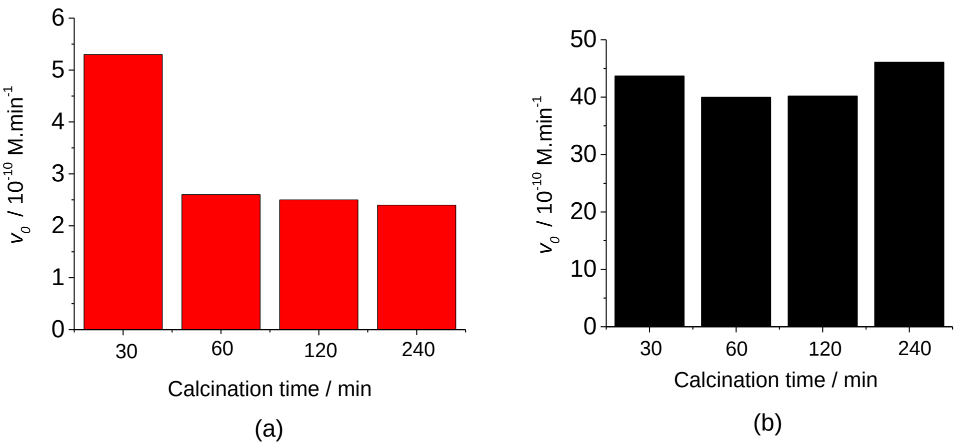

Figure 5.6. Effect of calcination time on the v_0 of 7-OHC formation under (a) visible and (b) UV light.

c_0(coumarin) = 0.8×10^{-4} M, c(catalyst) = 1 g dm^{-3} NT-A (450 °C), 20 dm^3 h^{-1} air

5.1.5 Effect of the calcination temperature

5.1.5.1 Material properties

The optimum parameters determined in the first stage of experiments were used for further investigations regarding the effect of the calcination temperature on the material properties and photoactivity under both UV and visible light.

Firstly, the changes of the vibrational states in the catalysts were measured by using FTIR spectroscopy. Fig. 5.7 exhibits the FTIR spectra of undoped TiO_2 and NT-A calcined at various temperatures.

For the undoped TiO_2 calcined at 0 °C (i.e., non-calcined), there are two characteristic peaks: a relatively sharp one at 1632 cm^{-1} and a broad one between 3000 cm^{-1} and 3500 cm^{-1}, which correspond to O-H bending and O-H stretching vibrations, respectively. However, after calcination at 450 °C, the sharp peak at 1632 cm^{-1} remarkably fell down and the broad band at 3000-3500 cm^{-1} significantly flattened.

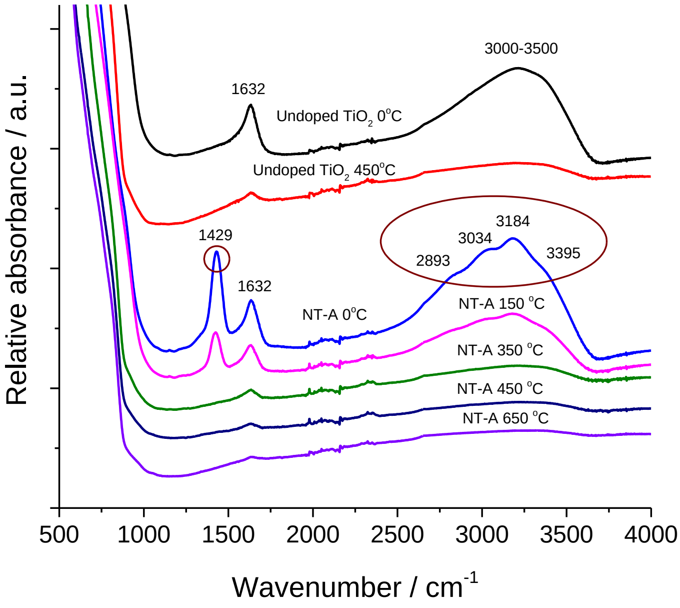

Figure 5.7. FTIR spectra of undoped TiO_2 and NT-A calcined at various temperatures.

For the NT-A catalyst (non-calcined), an additional peak appeared at 1429 cm^{-1} (N-H bending) and the broad band resolved into four ones at 2983, 3034, 3184, 3395 cm^{-1}, which can be assigned to N-H stretching overlapped with O-H vibrations. The intensity of these peaks decreased at 150 °C calcination temperature. The peak at 1429 cm^{-1} (N-H bending) and broad bands at 2800-3400 cm^{-1} started to disappear up to 350 °C calcination temperature while the peak at 1632 cm^{-1} still remained. It might be due to the transformations of N-H groups, resulting in new bonds of nitrogen (e.g., Ti-N/N-Ti-O), the vibrations of which were not detectable at the measurement parameters applied [19,168]. This tendency is relatively stable for calcination temperatures of 450 °C and 650 °C. The FTIR spectra of the undoped TiO_2 and NT-A catalysts calcined at 450 °C are very similar.

The structural properties of the catalysts were determined by using XRD measurements. Fig. 5.8 illustrates the XRD patterns of the undoped TiO_2 (450 °C) and NT-A catalysts calcined at various temperatures.

Pure anatase phase was obtained for undoped TiO_2 and NT-A calcined 450 °C. The diffraction peaks located at 25.2°, 37.8°, 47.9°, 54.9° and 62.7° are mainly related to the anatase phase (JCPDS card no. 21-1272) with Miller indices labeled as (101), (004), (200), (211) and (204), respectively.

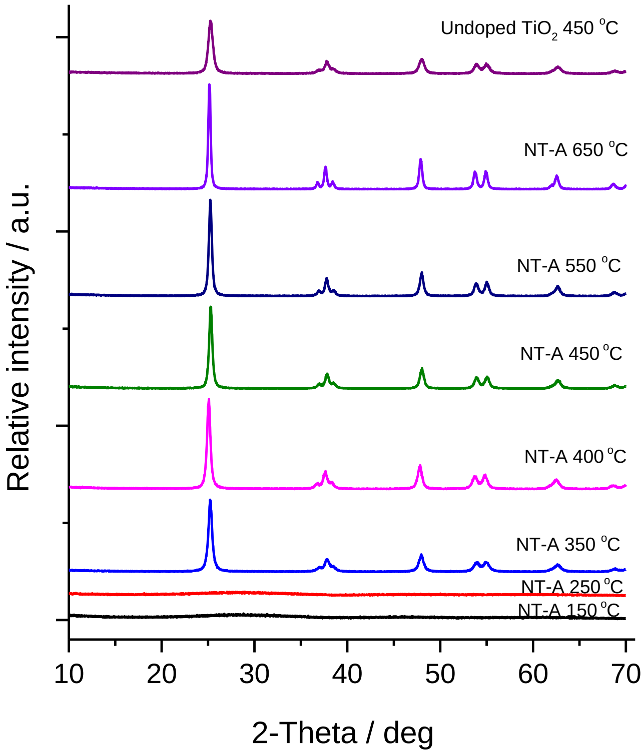

Figure 5.8. XRD patterns of undoped TiO_2 and NT-A calcined at various temperatures.

No peaks were observed for NT-A calcined at 150 °C and 250 °C, which indicated amorphous titania. The NT-A catalyst transformed into anatase phase above 350 °C and there was not any other phase transformation from anatase to rutile or brookite during calcination up to 650 °C. Generally, the phase transformation of pure TiO_2 from anatase to rutile occurs between 500 °C and 600 °C, and a complete transformation to rutile at 600 °C [169,170]. Our results clearly indicated that nitrogen doping of TiO_2 inhibited the phase transformation from anatase to rutile, in accordance with the TG-DTA measurement (Fig. 5.3) and a quite recent observation [112]. *Suwannaruang and fellow workers* synthesized nitrogen doped TiO_2 via hydrothermal method with various calcination temperatures from 300 °C to 700 °C. The XRD results showed that all samples contained only anatase crystalline phase and the phase transformation from anatase to rutile or brookite did not occur at calcination temperatures up to 700 °C [116].

The peak intensity of anatase (101) increases and the width of (101) plane becomes narrower with increasing calcination temperature. This tendency can be attributed to the growth of the average diameter of the crystal particles upon temperature rising. The crystallite sizes increased from 15 nm (350 °C) to 27.5 nm (650 °C) as summarized in Table 5.1. NT-A catalyst exhibited a higher crystallite size than that undoped TiO_2 possessed at the same calcination temperature (450 °C). In comparison, according to a previous work, the crystallite size of the standard Degussa P25 TiO_2 was approximately 79.7 nm [171].

Table 5.1. Summary of characteristic data for NT-A and TiO_2.

Calcination temperature / °C	Crystallite size / nm	Nitrogen content / wt %	Band-gap Energy / eV
non-calcined	-	14.09	-
150	-	9.53	3.01
250	-	8.88	3.03
350	15.05	8.41	3.05
400	17.22	7.20	3.11
450	19.20	5.50	3.12
500	20.70	3.30	3.13
650	27.53	3.61	3.17
450*	13.93	0.00	3.18

*Undoped TiO_2 calcined at 450 °C

Energy dispersive X-ray spectrometry (EDS) was applied to investigate the elementary composition of NT-A calcined at various temperatures. The nitrogen content of non-calcined NT-A was observed about 14.09 wt % and this value significantly decreased to 9.53 wt % after calcination at 150 °C. Then the percentage of nitrogen content continued to decrease upon increasing the calcination temperature (Table 5.1). It implies that not only water molecules were released from NT-A during the heating process, but also the nitrogen content changed. The loss of nitrogen could be replaced by oxygen from air upon increasing calcination temperature [172].

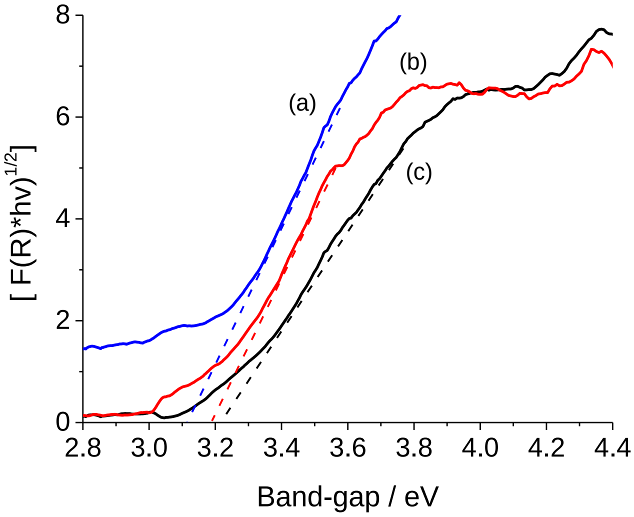

Figure 5.9. Tauc plot and band-gap energy of different catalysts.
(a) NT-A (450 °C): 3.12 eV (b) TiO_2 (450 °C): 3.18 eV (c) Degussa P25 TiO_2: 3.21 eV

The band-gap energies were determined by the analysis of diffuse reflectance spectra, applying the Kubelka-Munk function [149]. Fig. 5.9 shows the band-gap energy determined for Degussa P25 TiO_2 (3.21 eV), which is in good agreement with the literature data, i.e., the measurement method is reliable. About 3.18 eV band-gap energy was observed for undoped TiO_2 (450 °C) and this value slightly decreased to 3.12 eV after nitrogen doping (NT-A, 450 °C). This phenomenon is in accordance with previous observations, according to which the obtained band-gap energy of N-TiO_2 catalysts were 2.94-3.18 eV [12,19,112,116]. Those catalysts exhibited excellent photocatalytic performances in the degradation of *MB*, *RhB*, and ciprofloxacin under both visible and UV light.

Upon enhancing the calcination temperature, the band-gap energy indicates a moderate, but monotonous increase (Table 5.1). It is strongly related to the decrease of the nitrogen content. It is well known that nitrogen as doping element induces the formation of a new energy level (localized N 2p state) in the valence band, extending the light absorption into the visible range [113,172]. These results can also be used to verify that the higher calcination temperature could potentially increase the band-gap energy, due to the nitrogen loss.

5.1.5.2 Effect of calcination temperature on the photoactivity

The photocatalytic activity of these NT-A catalysts prepared in the various calcination temperatures were evaluated under UV light as shown in Fig. 5.10. The NT-A catalysts calcined at 150 °C and 250 °C were inefficient regarding the photoinduced 7-OHC formation, independently of the irradiation wavelength. It can be explained by the XRD results, according to which these catalysts were still in amorphous form. This phase contains many bulk defects, which served as recombination sites of photo-generated electrons and hole, thus leading to very low 7-OHC formations [173].

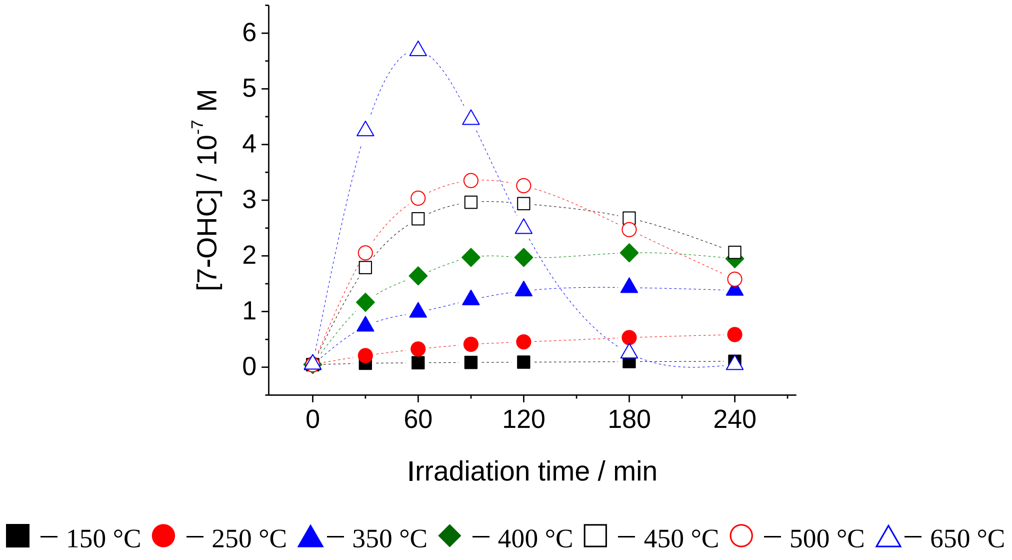

Figure 5.10. 7-OHC formation by NT-A catalysts prepared at various calcination temperatures, under UV light.

c_0(coumarin) = 0.8×10^{-4} M, c(catalyst) = 1 g dm^{-3} NT-A, UV LED, 20 dm^3 h^{-1} air

The photoactivities of NT-A calcined at 350 °C and 400 °C increased during the first 90-min period, then achieved a constant value. However, in the case of higher calcination temperatures (450, 500 and 650 °C), the intensity of 7-OHC formation rapidly increased during the first (90 min). In this period, an efficient formation of hydroxyl radical occurred, leading to a significant coumarin degradation accompanied with an appreciable 7-OHC formation [174]. After the first period, a declining phase occurred due to the low amount or completed degradation of coumarin and induced a low concentration of 7-OHC formation. In addition, the decrease of 7-OHC formation can also be attributed to the relative excess of *ROS* ($^{\bullet}OH$, $^{\bullet}O_2^{-}$, H_2O_2), which can also further degrade the formed 7-OHC itself along with other hydroxylated intermediates [175,176].

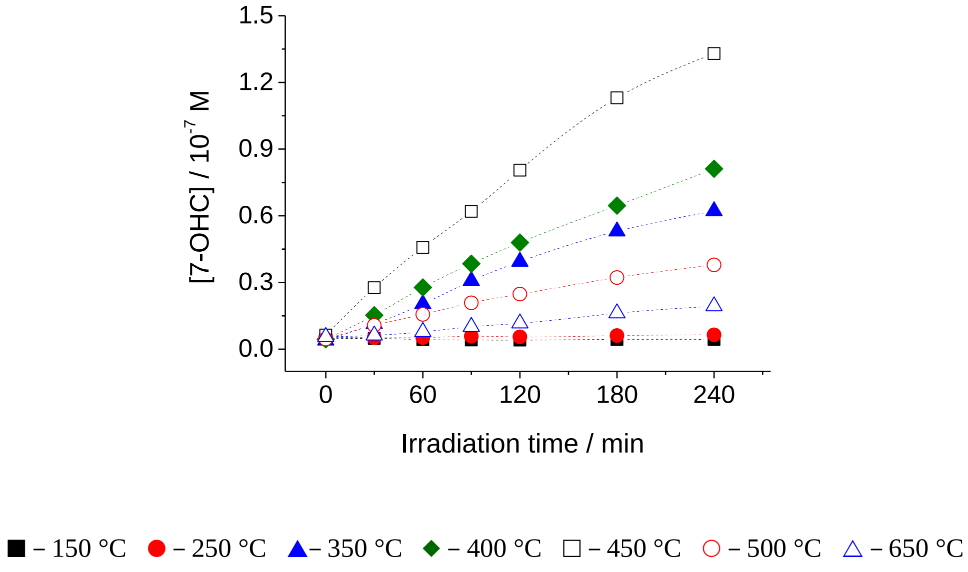

Figure 5.11. 7-OHC formation by NT-A catalysts prepared at various calcination temperatures, under visible light.

c_0(coumarin) = 0.8×10^{-4} M, c(catalyst) = 1 g dm^{-3} NT-A, Vis LED (1st arrangement), 20 dm^{3} h^{-1} air

The effect of calcination temperature on the 7-OHC formation under visible light is shown in Fig. 5.11. The NT-A catalysts calcined at 150 °C and 250 °C were also inactive regarding 7-OHC formation due to the amorphous phase of them. On other hand, the 7-OHC formation by NT-A steadily rose for higher calcination temperatures from 350 °C to 450 °C, and dramatically decreased for 500 °C and 650 °C. The optimum calcination temperature was obtained at 450 °C with a 7-OHC formation of 1.33×10^{-7} M after a 240-min visible irradiation.

Furthermore, beside the deviating tendencies, UV irradiation strongly improved the v_0 of 7-OHC formation over the NT-A catalysts compared to that observed under visible light. The ratio of 7-OHC formation ($v_{0\ \mathrm{UV/Vis}}$) increased upon increasing the calcination temperature from 5.2 to 187.6 for NT-A 350 °C and NT-A 650 °C, respectively (Table A5.1). This phenomenon can be attributed to the higher energy of UV compared to that of visible light [177] and to the structural deviations originated from the different nitrogen contents.

Moreover, crystalline phase, crystallite size, nitrogen content, and surface morphology are important features affecting the photocatalytic performances of NT-A catalysts. According to the XRD results, all catalysts were transformed into pure anatase phase during calcination at 350 °C to 650 °C, but they are characterized by different nitrogen contents and crystallinities (Table 5.1).

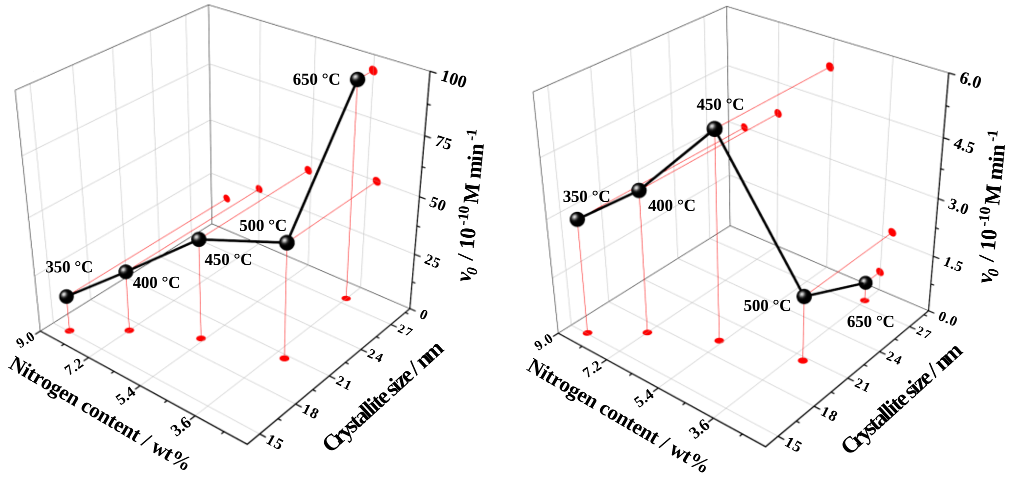

(a) (b)

Figure 5.12. Correlation of calcination temperature, nitrogen content and crystallite size on the v_0 of 7-OHC formation under (a) UV and (b) visible light.

The v_0 of 7-OHC formation under UV light significantly improved by higher calcination temperature. The increase of photoactivity was in line with the increasing of crystallite size (Fig. 5.12 a). Crystallites of larger size contained only few defects on the crystal lattice, thus resulting in less recombinations of charge carriers, and inducing a higher photoactivity [178]. However, it should also be noted that an increase of the calcination temperature also reduces the nitrogen content, which results in only a slight change in the oxidation capacity of the valence band. Nevertheless, it is a general phenomenon that relatively small decreases of the band gap diminishes the photoactivity in the UV range.

Under visible light, the photoactivity increased from 350 °C to 450 °C calcination temperatures and significantly decreased from 500 °C to 650 °C. Although the crystallite size steadily increased, the lower of photoactivities regarding 500 °C and 650 °C might be attributed to the decrease of the nitrogen content (Table 5.1) during calcination, which led to a higher band-gap energy and less light absorption in the visible range [19,116,172,179]. From this point of view, both crystallite size and nitrogen content of the NT-A catalysts play crucial roles in the v_0 of 7-OHC formation (Fig. 5.12 b).

5.1.6 Photocatalytic reactions of coumarin

One of our goals was to study the reactions of coumarin as a probe of the photocatalytic activity of the N-TiO_2 upon both UV- and visible-light irradiations. Beside the investigation of hydroxyl radical (7-OHC) production, coumarin degradation was also monitored during the photocatalytic experiments in order to estimate the degradation efficiency and the possibility of reactions between the parent compound and other photo-generated species such as electron or superoxide anion radical. For this purpose, the reaction mixtures were saturated with Ar or air during the irradiations, ensuring anaerobic or aerobic conditions, respectively.

5.1.6.1 Under UV light

The first measurements were carried out under UV irradiation with NT-A calcined at 450 °C because it displayed the highest photoactivity under visible light. Fig. 5.13 shows that 7-OHC formation in the absence of oxygen exhibited a gradual increase during the irradiation. After a 60-min irradiation, the concentration of

7-OHC reached 1.30×10^{-7} M and that of all OHC derivatives was 4.48×10^{-7} M. However, in the presence of oxygen the concentration of 7-OHC and OHC increased in the first period of irradiation time and subsequently declined. During the first 60-min irradiation, the concentration of 7-OHC and OHC reached 2.66×10^{-7} M and 9.18×10^{-7} M, respectively. The enhancement of the photoactivity in the presence of oxygen might be attributed to a better charge separation of photo-generated electron-hole pairs leading to a higher hydroxyl radical formation. In addition, the presence of oxygen probably opens a new cathode reaction, i.e., the oxygen reduction occurres at a more positive cathode potential compared to that in the absence of oxygen, which polarizes both the anode and the cathode to a more effective position, and that way increases the electric current and the rate of chemical reaction [180].

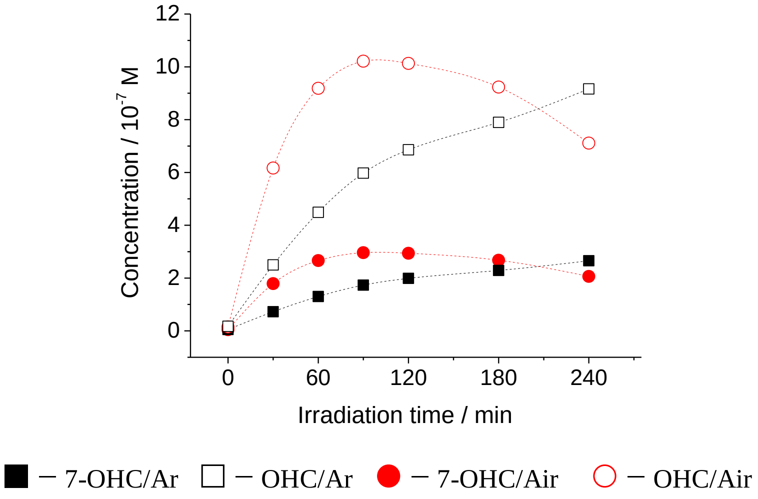

Figure 5.13. The change of concentrations under different circumstances.

c_0(coumarin) = 0.8×10^{-4} M, c(catalyst) = 1 g dm^{-3} NT-A (450 °C), UV LED, 20 dm^{3} h^{-1} gas

The concentration of coumarin was also measured during the photocatalytic reaction to evaluate the degradation efficiency. As illustrated in Fig. 5.14, in anaerobic atmosphere, the total coumarin degradation efficiency after a 240-min irradiation and the first-order degradation rate constant were 20.2 % and 1.63×10^{-5} s^{-1}, respectively. However, in aerobic atmosphere, the degradation efficiency of coumarin significantly increased; to 58.6 % after 240-min irradiation, with a degradation rate constant of $k = 6.10\times10^{-5}\ \mathrm{s}^{-1}$.

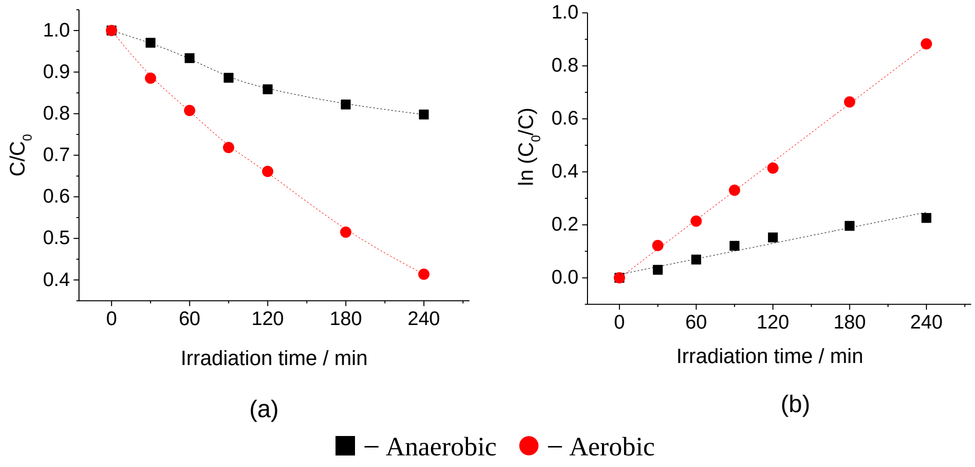

Figure 5.14. (a) Coumarin degradation and (b) its logarithm (for rate constant determination) under anaerobic and aerobic conditions. c_0(coumarin) = 0.8×10^{-4} M, c(catalyst) = 1 g dm^{-3} NT-A (450 °C), UV LED, 20 dm^{3} h^{-1} gas

In order to study the photocatalytic degradation pathways of coumarin, the total coumarin degradation was obtained from the difference between the initial and the actual coumarin concentrations. OHC concentration indicates the amount of coumarin degraded through the reactions with hydroxyl radical. The difference between the total coumarin degradation and the OHC concentration suggests the coumarin degradation through reactions with other reactive species.

Fig. 5.15 shows that coumarin prefers reaction with species other than hydroxyl radical which the efficiencies of coumarin degradation through the reaction with hydroxyl radical hardly depended on the presence of oxygen. The coumarin reactions with hydroxyl radicals were closely similar in anaerobic (0.97 %) and aerobic (1.01 %) atmospheres within a 60-min UV irradiation. However, the efficiencies of coumarin reaction with other reactive species significantly increased to 5.68 % and 18.24 % for anaerobic and aerobic atmosphere, respectively.

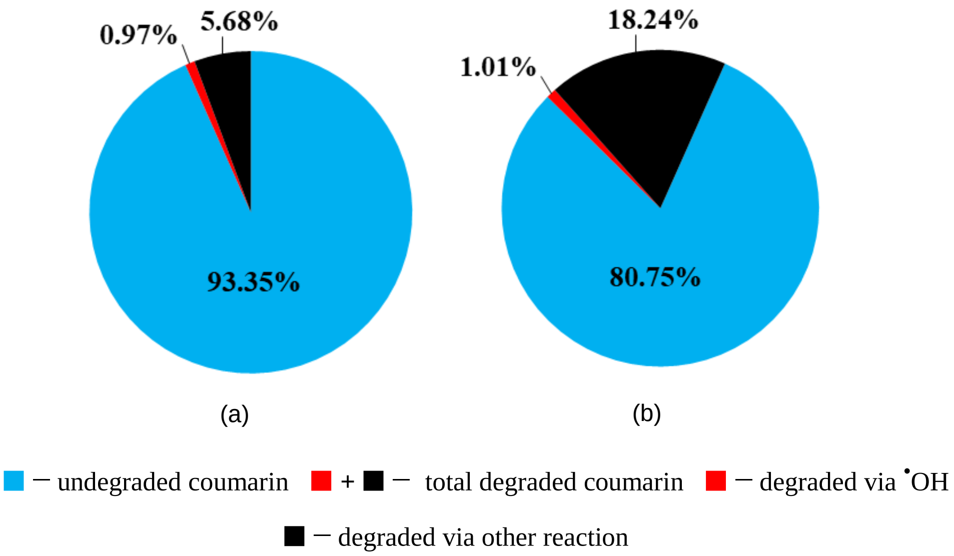

Figure 5.15. Degradation pathways of coumarin in (a) anaerobic and (b) aerobic atmosphere after 60-min irradiation under UV light.

c_0(coumarin) = 0.8×10^{-4} M, c(catalyst) = 1 g dm^{-3} NT-A (450 °C), UV LED, 20 dm^3 h^{-1} gas

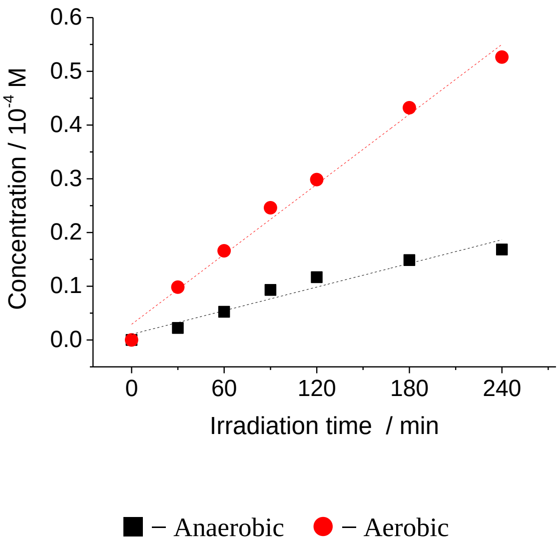

Figure 5.16. Irradiation time dependence of concentration of coumarin degraded through the reactions with other reactive species.

c_0(coumarin) = 0.8×10^{-4} M, c(catalyst) = 1 g dm^{-3} NT-A (450 °C), UV LED, 20 dm^3 h^{-1} gas

The results of the present study are in agreement with those of a previous investigation conducted by *Zerjav et al.*, according to which less than 2 % of coumarin was converted into the photoluminescent 7-OHC [134]. The v_0 of coumarin degradation via reactions with other reactive species under anaerobic and aerobic conditions were 1.0×10^{-7} M min^{-1} and 2.7×10^{-7} M min^{-1}, respectively (Fig. 5.16).

Generally, photocatalytic reaction was initiated by irradiation of NT-A catalyst, producing photo-generated electrons in the *cb*, along with the corresponding positive holes in the *vb*. In anaerobic atmosphere (Ar), these photo-generated electrons and holes can quickly recombine in the absence of electron scavenger, leading to a low photoactivity (Eqs. 5.3-5.4). However, at the same time, coumarin can act as an electron scavenger ($k = 1.6\times10^{10}$ M^{-1} s^{-1} [181]) in the absence of oxygen, forming non-fluorescent products (Eq. 5.5), while the holes in the *vb* react with adsorbed H_2O molecules, leading to the formation of hydroxyl radical (Eq. 5.6). Various OHC products are formed in the reaction with coumarin as illustrated in Eq. 5.7 [138].

$$\text{NT-A} + h\nu \rightarrow \text{NT-A}(h_{vb}^{+} + e_{cb}^{-}) \qquad \text{Excitation} \qquad (5.3)$$

$$\text{NT-A}(h_{vb}^{+} + e_{cb}^{-}) \rightarrow \text{NT-A} \qquad \text{Recombination} \qquad (5.4)$$

$$e_{cb}^{-} + \text{coumarin} \rightarrow \text{non-fluorescent products} \qquad (5.5)$$

$$h_{vb}^{+} + H_2O \rightarrow {}^{\bullet}OH + H^{+} \qquad (5.6)$$

$${}^{\bullet}OH + \text{coumarin} \rightarrow \text{fluorescent 7-OHC + other OHC} \qquad (5.7)$$

In the case of aerobic atmosphere, oxygen is a powerful electron scavenger, thus extending the lifetime of the photo-generated electron-hole pairs (or derived species). The rate constant of the reaction between electron and O_2 ($k = 2.3\times10^{10}$ M^{-1} s^{-1} [182]) is higher than that for the reaction of electron with coumarin ($k = 1.6\times10^{10}$ M^{-1} s^{-1} [181]). The concentrations of coumarin and dissolved oxygen (in air-saturated solution at 20 ^{o}C) are 0.8×10^{-4} M and 2.8×10^{-4} M [183], respectively. Therefore, the reactions of photo-generated electrons with coumarin is less favorable and more coumarin is degraded by the reaction with the superoxide anion radical (Eq. 5.8).

$$e_{cb}^{-} + O_2 \rightarrow {}^{\bullet}O_2^{-} \qquad (5.8)$$

Superoxide anion radical can be easily protonated (*pKa* ($^{\bullet}OOH/^{\bullet}O_2^{-}$) = 4.8 [184]), producing hydroxyl radical in the further reaction steps (Eqs. 5.9-5.11). Subsequently, hydroxyl radical formed from the protonation of superoxide anion radical, as well as from the oxidation of H_2O by holes (Eq. 5.6), easily reacts with coumarin (Eq. 5.7; $k = 2.0\times10^{9}$ M^{-1} s^{-1} [182]).

$${}^{\bullet}O_2^{-} + H^{+} \leftrightarrow {}^{\bullet}OOH \qquad (5.9)$$

$${}^{\bullet}OOH + {}^{\bullet}OOH \rightarrow H_2O_2 + O_2 \qquad (5.10)$$

$$H_2O_2 + {}^{\bullet}O_2^{-} \rightarrow {}^{\bullet}OH + OH^{-} + O_2 \qquad (5.11)$$

However, our results indicated that superoxide anion radicals were predominantly in deprotonated form, owing to the neutral *pH* = 6-7 of the solution during irradiation. Hence, this suggests that the reaction of superoxide anion radicals with coumarin can considerably contribute to its degradation, resulting in non-fluorescent products as shown in Eq. 5.12 [185,186].

$${}^{\bullet}O_2^{-} + \text{coumarin} \rightarrow \text{non-fluorescent products} \qquad (5.12)$$

Therefore, apart from the processes via hydroxyl radical, coumarin degradation in aerobic system is more efficient than in anaerobic one, due to the reaction with superoxide anion radicals. Moreover, dissolved oxygen can significantly increase the oxidative transformation of instable radicals formed in the reactions of coumarin with *ROS*.

Furthermore, NT-A catalysts calcined at various temperatures were also investigated in anaerobic and aerobic atmospheres under UV light. Regarding the different calcination temperatures, the photoactivity increased upon increasing the calcination temperature in both aerobic and anaerobic systems. NT-A calcined at 650 °C showed the best 7-OHC formation under both anaerobic and aerobic atmospheres (Table 5.2).

Table 5.2. Comparison of 7-OH formation over NT-A calcined at different temperatures.

Calcination temperature / °C	**v_0 of 7-OHC formation / 10^{-10} M min^{-1}**		**Ratio (b:a)**
	(a) Anaerobic	**(b) Aerobic**	
350	7.8	15.7	2.0
450	20.9	43.7	2.1
650	28.0	93.8	3.3

The degradation of coumarin revealed an identical trend, according to which NT-A catalyst calcined at 650 °C also exhibited the highest degradation efficiencies after 240 min irradiation. The results also indicate that the presence of oxygen (air) could enhance the v_0 of coumarin degradation by over 10 fold compared to that of the value in anaerobic system (Table 5.3).

Table 5.3. Comparison of coumarin degradation over NT-A calcined at different temperatures.

Calcination temperature / °C)	**v_0 of coumarin degradation / 10^{-7} M min^{-1}**		**Ratio (b:a)**
	(a) Anaerobic	**(b) Aerobic**	
350	0.3	1.5	5.0
450	1.0	3.6	3.6
650	1.3	15.1	11.6

In addition, the ratio (aerobic/anaerobic) of coumarin degradations was higher than the ratio (aerobic/anaerobic) of 7-OHC formations. In other words, the production of electrons or superoxide anion radicals was greater than that of hydroxyl radicals (7-OHC) over NT-A calcined at 650 °C. As shown in Fig. 5.12 a, the nitrogen content drops and the crystallite size increases at high calcination temperature (650 °C). From this point of view, it can be assumed that less nitrogen content and larger crystallite size of NT-A are favorable for the generation of more electrons or superoxide anion radicals under UV-light irradiation.

5.1.6.2 Under visible light

Furthermore, the 7-OHC formation under visible light was also assessed in both systems (anaerobic and aerobic). The v_0 of 7-OHC formation in anaerobic atmosphere was 0.9×10^{-10} M min^{-1} and it increased to 5.3×10^{-10} M min^{-1} upon aeration of the system as shown in Fig. 5.17.

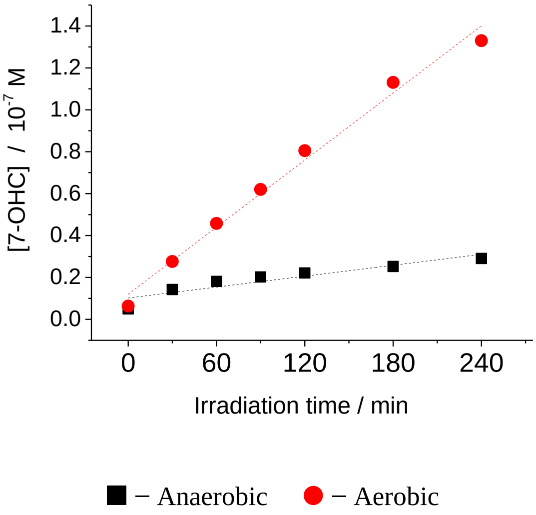

Figure 5.17. 7-OHC formation over NT-A in aerobic and anaerobic atmosphere. c_0(coumarin) = 0.8×10^{-4} M, c(catalyst) = 1 g dm^{-3} NT-A(450 °C), Vis LED (1st arrangement), 20 dm^3 h^{-1} gas

In comparison, the v_0 of 7-OHC formation in the visible was significantly lower than that under UV light. The v_0 of 7-OHC formation under UV light were 20.9×10^{-10} and 43.7×10^{-10} M min^{-1} for anaerobic and aerobic systems, respectively. As a result, the change of coumarin concentration (due to its transformations) could not be reliably detected by using spectrophotometric measurements during the photocatalytic reaction under both anaerobic and aerobic atmospheres.

In order to enhance the photoactivity, the lamp arrangement and position was modified to obtain higher light intensity. Two visible LEDs were placed at both sides of the reactor with a distance of 3 cm (Fig. 4.2 b).

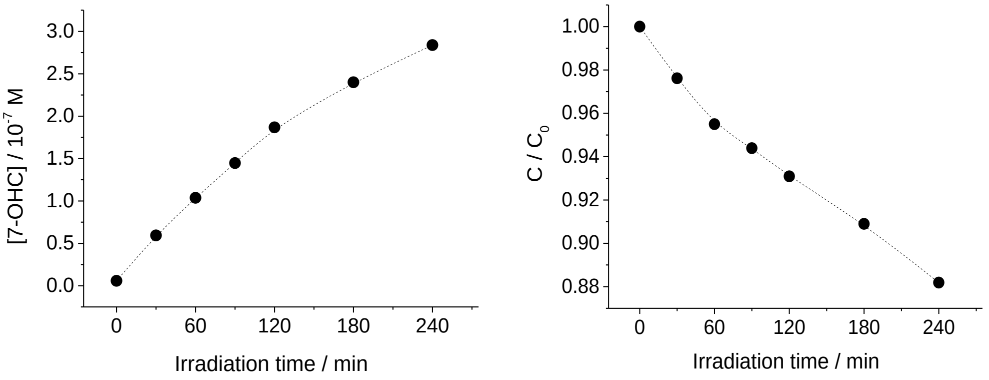

Figure 5.18. (a) 7-OHC formation and (b) coumarin degradation over NT-A by using second lamp-arrangement in aerobic atmosphere.

c_0(coumarin) = 0.8×10^{-4} M, c(catalyst) = 1 g dm^{-3} NT-A(450 °C), Vis LED (2nd arrangement), 20 dm^3 h^{-1} air

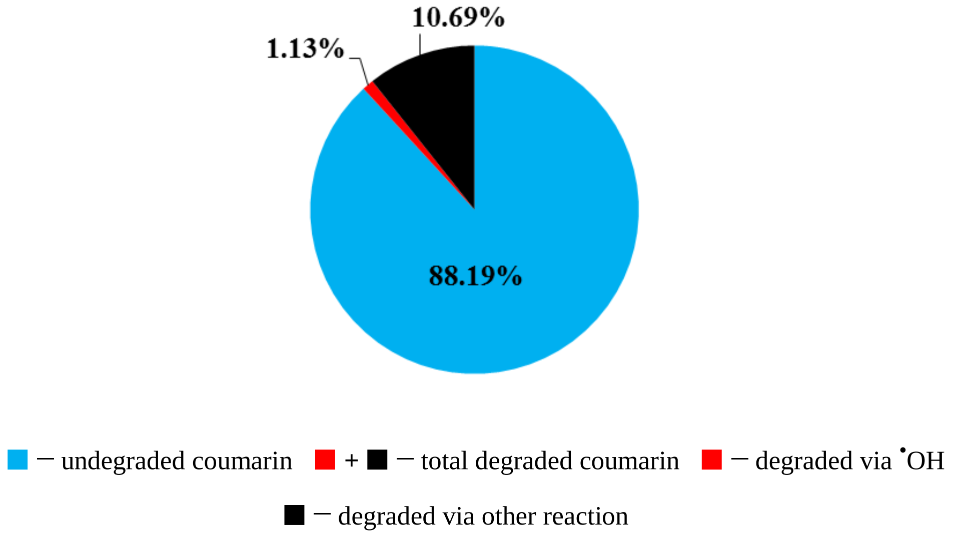

Figure 5.19. Photocatalytic pathways of degraded coumarin over NT-A after a 240-min visible irradiation.

c_0(coumarin) = 0.8×10^{-4} M, c(catalyst) = 1 g dm^{-3} NT-A(450 °C), Vis LED (2nd arrangement), 20 dm^3 h^{-1} air

As shown in Fig. 5.18 a, the NT-A catalyst with the second arrangement exhibited a higher photoactivity (v_0 = 15.4×10^{-10} M min^{-1}) compared to the first arrangement (v_0 = 5.3×10^{-10} M min^{-1}) under aerobic condition. The result was in agreement with the degradation tendency where the change of coumarin concentration could be detected during photocatalytic experiment. The efficiency of coumarin degradation within a 240-min visible irradiation was 11.82 % (Fig. 5.18 b).

Furthermore, the transformation of coumarin into other hydroxylated derivatives as well as via reactions of other photo-generated reactants (such as electrons or superoxide anion radicals) was also determined under visible irradiation. As it can be seen in Fig. 5.19, the degradation of coumarin took place predominantly via other reactive species (10.69 %), while only 1.13 % of coumarin decomposed through the reaction with hydroxyl radicals. The results indicate an identical phenomenon as in the investigation under UV light (Fig. 5.15 b).

5.2 NT-U catalyst

The optimum calcination parameters of NT-A catalyst (450 °C for 30 min) were used to prepare NT-U, but applying a deviating method and precursors. The NT-U catalyst was prepared via sol-gel method using titanium (IV) isobutoxide and urea as starting materials. The prepared catalyst was then characterized by using TG-DSC, Raman and SEM-EDS analyses.

5.2.1 Characterizations

Thermogravimetry and differential scanning calorimetry were used to detect the changes during the heat treatment of the catalysts. Fig. 5.20 shows the derivatograms of dried NT-U (initial mass = 15.090 mg) powders (100 %).

Generally, TG curve of NT-U can be divided into several stages. Firstly, the weight loss about 13.22 % (2.0 mg) was observed below 123 °C heat treatment, which could be attributed to volatilizing of residual ethanol solvent or water surface-adsorbed during the preparation. A weight loss about 15.69 % was observed in the second stage from 123-289 °C (2.40 mg), which might be corresponding to the release of surface adsorbed water or residual organic compound originated from titanium precursor [187]. No significant weight loss was observed in the following stages.

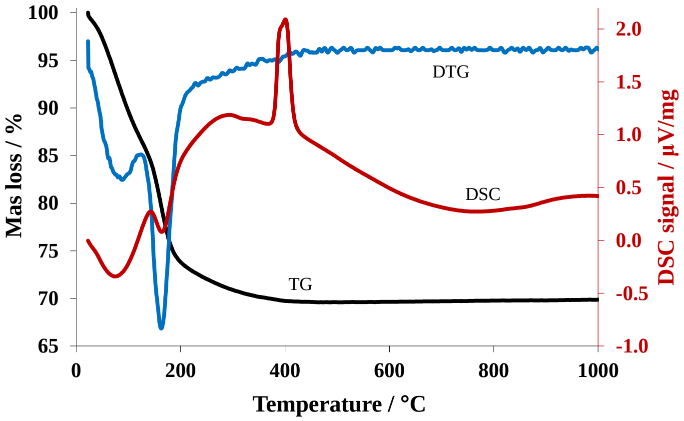

Figure 5.20. TG-DSC curve of NT-U catalysts.

Starting sample = the sample dried at 40 °C for 24 h in the preparation step

The DSC curve shows 2 separate processes below 289 °C, and this phenomenon also appears in the TG curve. However, only one overlapping mass loss can be observed for NT-A. (The TG-DSC results for NT-A catalyst investigated in the same condition can be seen in Fig. A5.4). It is owing to different solvents applied during the preparations of NT-U (ethanol) and NT-A (water). In addition, a strong exothermic peak around 400 °C is observed, which can be assigned to the phase transformation of the TiO_2 structure from amorphous to anatase [159].

Raman analysis was carried out in order to investigate the crystalline phase of catalysts after 1015 °C annealing. The results show that the crystalline phase of NT-U catalyst was transformed into rutile. However, in the case of NT-A, it was relatively stable at anatase phase, even after high annealing (Fig. A5.5).

The morphology of NT-U (calcined at 450 °C) was studied by using SEM. The results show that polydispersed (irregular) micro-particles were also obtained for the NT-U catalyst, with sizes in the 1-50-µm range. The morphology of the catalyst prepared by using sol-gel method (NT-U) showed a significant difference from that of the NT-A catalyst prepared by using co-precipitation method. NT-U possessed a non-hollow structure (Fig. 5.21 a), while NT-A exhibited a hollow structure (Fig. 5.4 b).

In addition, the nitrogen content of the catalyst obtained from EDS elemental analysis was about 4.78 wt % as shown in Fig. 5.21 b. This value is relatively lower than that for the NT-A catalyst (5.50 wt %) calcined at the same temperature (450 °C) as shown in Table 5.1. It could be attributed to the less amount of nitrogen source added during the preparation of NT-U (0.06 mol urea) compared to that applied for the NT-A catalyst (1.14 mol ammonia).

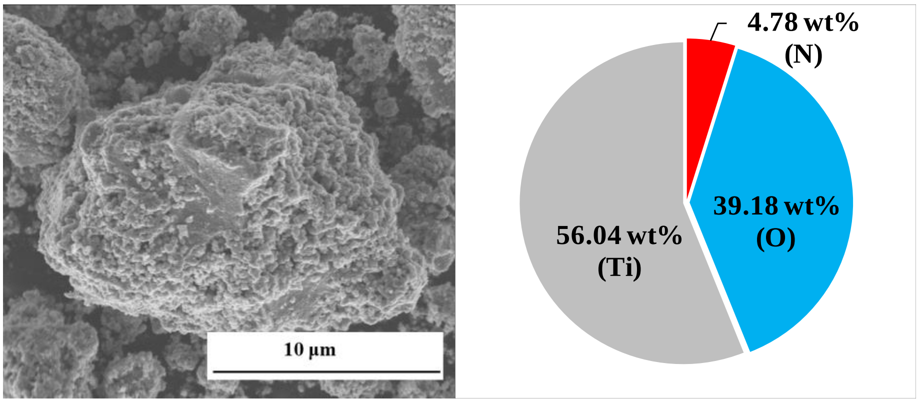

(a) (b)

Figure 5.21. (a) SEM morphology and (b) EDS elemental composition of the NT-U.

5.2.2 Photoactivity

The photocatalytic experiment with NT-U catalyst was performed by using the second arrangement (Fig. 4.2 b). As Fig. 5.22 a shows, the concentration of 7-OHC formed over NT-U catalyst after 240-min visible irradiation reached 1.43×10^{-7} M. However, NT-U generated 7-OHC at a lower rate (v_0 = 7.4×10^{-10} M min^{-1}) compared to the NT-A catalyst (v_0 = 15.4×10^{-10} M min^{-1}) under the same conditions (Fig. 5.18 a).

A better photocatalytic performance of NT-A might be due to its hollow structure. This feature is crucial in the photocatalytic performance of the catalyst, owing to its large surface area (61 m^2 g^{-1}) and, thus, more efficient adsorption of coumarin, compared to that of the non-hollow-structured NT-U (32 m^2 g^{-1}). *Liu et al.* reported that mesoporous N-TiO_2 displayed a higher photocatalytic activity than the non-porous materials did under both UV and visible-light irradiations [188].

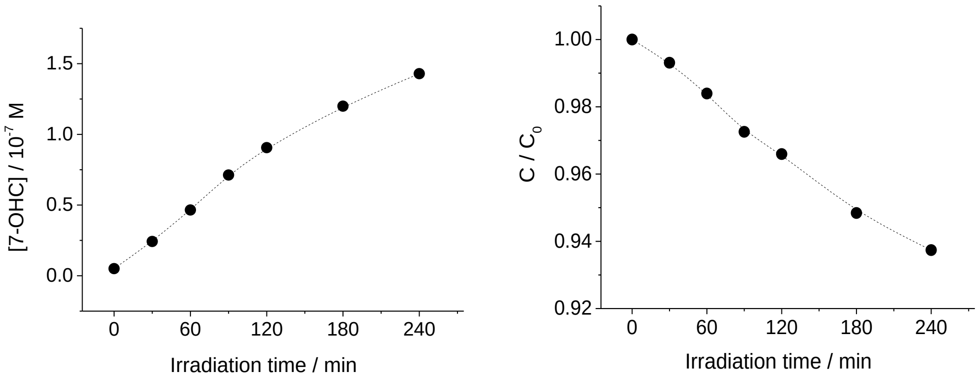

(a) (b)

Figure 5.22. (a) 7-OHC formation and (b) coumarin degradation of NT-U catalyst under aerobic atmosphere.

c_0(coumarin) = 0.8×10^{-4} M, c(catalyst) = 1 g dm^{-3} NT-U(450 °C), Vis LED (2nd arrangement), 20 dm^3 h^{-1} air

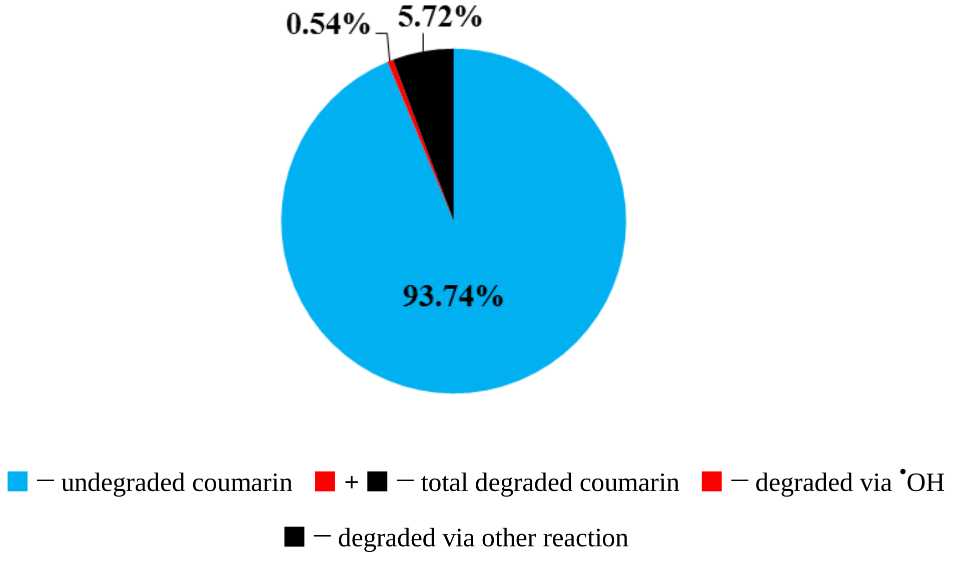

Figure 5.23. Photocatalytic pathways of degraded coumarin over NT-U after a 240-min visible irradiation.

c_0(coumarin) = 0.8×10^{-4} M, c(catalyst) = 1 g dm^{-3} NT-U (450 °C), Vis LED (2nd arrangement), 20 dm^3 h^{-1} air

Beside the formation of 7-OHC, the degradations of coumarin was also investigated. The result shows the efficiency of coumarin degradation was 6.26 % after a 240-min visible irradiation (Fig. 5.22 b). Moreover, a study of the photocatalytic pathways show the transformation of coumarin via reaction with other reactive species (5.72 %) was more favor than via reaction with hydroxyl radical producing hydroxylated derivatives (0.54 %) as shown in Fig. 5.23.

5.3 Silver deposition

In order to produce catalysts being suitable to both visible-light-driven photocatalytic and antibacterial applications, silver nanoparticles were utilized on the surface of both NT-U and NT-A catalysts by using a photodeposition technique. Silver nitrate solution and UV LED (λ_{max} = 390 nm) were used as Ag precursor and light source, respectively.

5.3.1 Silver deposition analysis

During the preparation of Ag/N-TiO_2, Ag^+ concentration in the solution was monitored by using ICP spectroscopy. Under dark conditions, a certain number of the dissolved Ag^+ ions were adsorbed on the surfaces of the catalysts. NT-A adsorbed a higher amount of Ag^+ compared to the case of the NT-U catalyst with concentrations of 0.97×10^{-5} and 0.89×10^{-5} mol Ag^+ per g catalyst, respectively (Fig. 5.24 a). However, after irradiation, all Ag^+ ions (both on the catalyst surface and in the solution) were reduced to form Ag^0 nanoparticles and deposited on the surfaces of NT-U and NT-A with concentrations of 0.99×10^{-5} mol g^{-1} and 1.00×10^{-5} mol g^{-1}, respectively (Fig. 5.24 b).

Typically, the photo-generated electrons on the surface of a catalyst are efficiently trapped by adsorbed Ag^+ (rather than by oxygen), resulting in the formation of Ag^0 nanoparticles. The holes react with adsorbed water molecules to form oxygen and H^+, according to the stoichiometry, as given in Eqs. 5.13-14 [184].

$$\text{N-TiO}_2\,(h_{vb}^+ + e_{cb}^-) + Ag^+_{adsorbed} \rightarrow \text{N-TiO}_2Ag^0\,(h_{vb}^+) \qquad (5.13)$$

$$4Ag^+ + H_2O \underset{\text{N-TiO}_2}{\overset{h\nu}{\rightarrow}} 4Ag^0 + 4H^+ + O_2 \qquad (5.14)$$

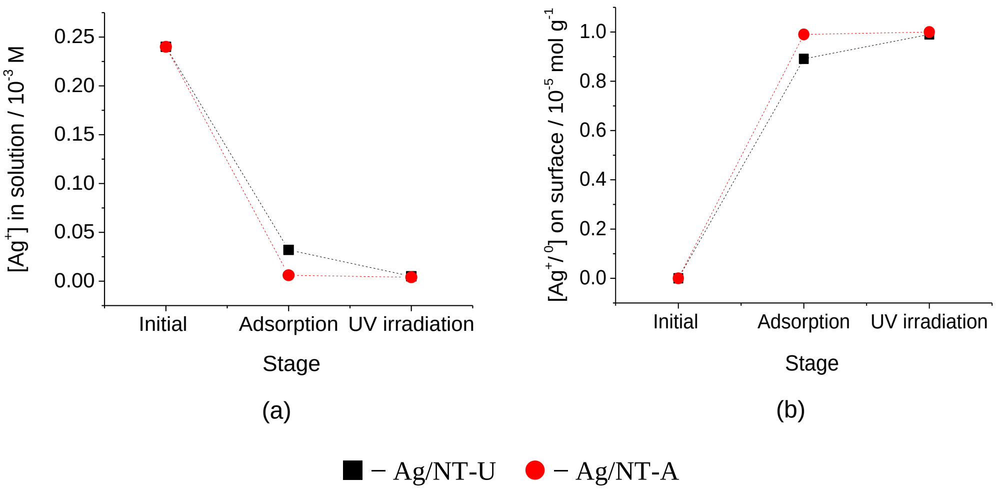

Figure 5.24. Change of (a) Ag^+ concentration in the solution phase and (b) Ag^+ (by adsorption) or Ag^0 (by photo-reduction) concentrations on the catalyst.

$c_0(AgNO_3) = 2.4\times10^{-4}$ M, c(catalyst) = 24 g dm^{-3}, NT-A, NT-U(450 °C), UV LED

Stage: **Initial** = $AgNO_3$ + water **Adsorption** = $AgNO_3$ + water + catalyst

UV irradiation = $AgNO_3$ + water + catalyst + UV LED

Moreover, the adsorption efficiency depended on the initial Ag^+ concentration in the solutions: 100 %, 89 %, and 79 % of Ag^+ were adsorbed on the surface of NT-U from solutions of 0.024, 0.24, and 2.40 mM Ag^+, respectively, resulting in 1.00×10^{-6}, 0.89×10^{-5}, and 0.79×10^{-4} mol g^{-1} concentrations on the catalyst. Subsequent UV irradiations, however, led to practically 100% deposition of silver, resulting in 1.0×10^{-6}, 1.0×10^{-5}, and 1.0×10^{-4} mol g^{-1} concentrations.

5.3.2 Material characterization

The morphology and elemental composition of the catalysts were studied by SEM and TEM-EDS measurements. As displayed in Figs. 5.25 a-b, SEM images of Ag/NT-U and Ag/NT-A show that Ag deposition exhibited a negligible difference on the surface of catalysts compared to unmodified ones (Fig. 5.21 a shows NT-U and Fig. 5.4 b shows NT-A). It might be due to the very low concentration of Ag loading, which was not detectable in the SEM measurement. However, by using TEM measurement with higher resolution, it was possible to observe the presence of quasi-spherical Ag nanoparticles on the surface of Ag/NT-U with 10^{-5} mol Ag g^{-1} catalyst (Figs. 5.25 c-f).

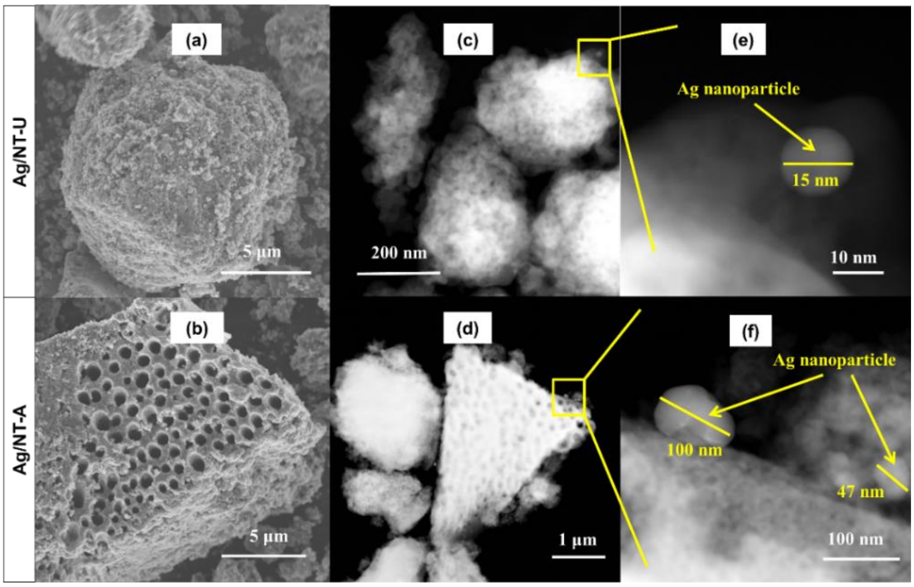

Figure 5.25. (a-b) SEM and (c-f) TEM micrographs of Ag/NT-U and Ag/NT-A catalysts. (Ag concentration = 10^{-5} mol g^{-1})

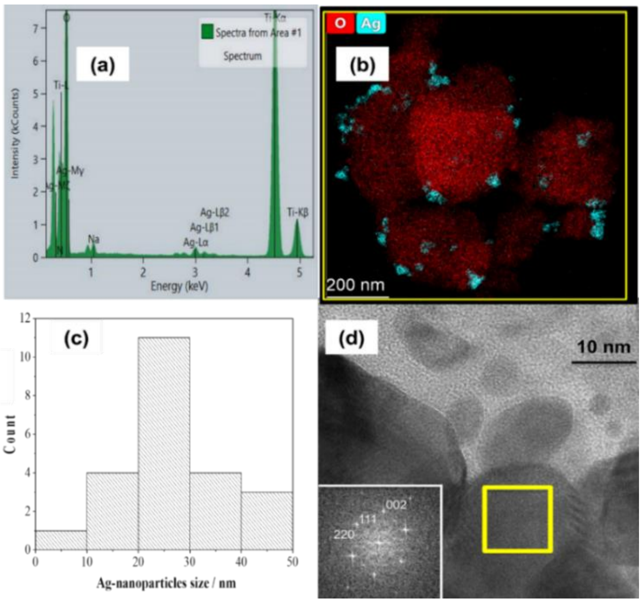

Figure 5.26. (a) EDS spectrum (b) element map obtained in STEM–EDS mode (c) size distribution of Ag nanoparticles (d) HRTEM image of Ag nanoparticles. Inserted on the lower left = FFT pattern obtained from the area marked by the yellow square; catalyst = Ag/NT-U 10^{-5} mol g^{-1}

Additionally, the EDS spectra shows that the catalyst consists of Ti and O as major elements, and according to the element maps, the nanoparticles of silver as a dopant are unevenly distributed on the TiO_2 aggregates (Figs. 5.26 a-b). The sizes of the Ag nanoparticles on Ag/NT-U 10^{-5} mol g^{-1} are typically in the range of 5-50 nm, but most of them are about 20-30 nm (Fig. 5.26 c). Fig. 5.26 d shows a high-resolution transmission electron microscope (HRTEM) image and the corresponding fast Fourier transform (FFT) pattern, suggesting that the nanoparticle consists of pure silver (Ag^0).

The specific surface areas (S_{BET}) of the samples were measured by BET (Brunauer-Emmett-Teller) methods as displayed in Table 5.4. The NT-A catalyst possessed a larger specific surface area (and pore volume) than NT-U did, with S_{BET} values of 61 and 32 m^2 g^{-1}, respectively. These values are in accordance with the different (hollow and non-hollow) structures shown by the SEM images (Fig. 5.4 b, for NT-A and Fig. 5.21 a, for NT-U). There are similar results in the literature. For instance, *Suwannaruang et al.* obtained about 34-42 m^2 g^{-1} of specific surface area for N-TiO_2 catalysts with nanorice structure prepared by using hydrothermal method [112]. Their values indicate relatively even particle surfaces.

Table 5.4. S_{BET} value and pore volume of the catalysts prepared.

Catalyst	**S_{BET} value / m^2 g^{-1}**	**Pore volume $V_{1.7\text{-}100\ nm}$ / cm^3 g^{-1}**
NT-U	32	0.08
Ag/NT-U 10^{-6}	47	0.09
Ag/NT-U 10^{-5}	47	0.10
Ag/NT-U 10^{-4}	46	0.09
NT-A	61	0.14
Ag/NT-A 10^{-6}	61	0.13
Ag/NT-A 10^{-5}	62	0.14
Ag/NT-A 10^{-4}	60	0.12

$V_{1.7\text{-}100\ nm}$ - BJH cumulative desorption pore volume of pores with diameters between 1.7 and 100 nm.

Ag-loading on the NT-U (10^{-6} mol g^{-1}) enhanced the specific surface area from 32 m^2 g^{-1} to 47 m^2 g^{-1} and relatively constant at higher Ag concentration. Meanwhile, in the case of Ag-loading (10^{-6} mol g^{-1}) on NT-A, the specific surface area is similar to that of the unmodified one and hardly changed even at different Ag concentrations (from 60 m^2 g^{-1} to 62 m^2 g^{-1}).

The different tendencies for NT-U and NT-A may be interpreted by consideration of both the structures of the catalysts and their modification by the Ag nanoparticles deposited on the particles' surfaces. The non-hollow structure of NT-U resulted in a lower specific surface area, which could be increased by the silver nanoparticles having considerably larger surfaces than the area they covered on the catalyst. The NT-A catalyst, however, possessed a significantly higher specific surface area due to the surficial holes with rather bent walls. Hence, deposition of Ag nanoparticles on these walls could not appreciably enhance the surface area; their own surface hardly exceeded the occupied area on the catalyst.

A partly similar phenomenon was observed by *Wang et al.* regarding the specific surface areas of Ag-TiO_2 nanofibers and nanotubes synthesized by general and emulsion electrospinning processes, respectively [189]. They reported that Ag-deposition on the TiO_2 nanotubes enhanced the specific surface area from 60.58 m^2 g^{-1} to 76.93 m^2 g^{-1}. In contrast, the specific surface area of TiO_2 nanofiber (53.17 m^2 g^{-1}) slightly decreased after Ag-loading (51.62 m^2 g^{-1}). Those results are also in accordance with the shapes of the catalyst surfaces.

The BJH (Barret-Joyner-Halenda) model was used to estimate the pore-size distribution of the samples in the range of 1.7-100 nm diameter. The surface of the NT-A catalyst possessed higher volumes of pores in the diameter range of 3-8.5 nm compared to those of NT-U. Ag-loading on the NT-U significantly enhanced the volumes of the pores in this diameter range, while it just slightly increased for the NT-A catalyst. Besides, much lower volumes of pores in the diameter range of 10-100 nm appeared for NT-A and Ag/NT-A catalysts, but still higher than for NT-U and Ag/NT-U. The pore distributions of NT-A and Ag/NT-A are identical for this range (10-100 nm). The higher volumes of pores resulted in larger specific surface area of the catalysts, for instance Ag/NT-A 10^{-5} possessed a largest pore volume (0.14 cm^3 g^{-1}) as well as surface area (62 m^2 g^{-1}), as indicated in Table 5.4. Besides, Fig. 5.27 also suggests that silveration of NT-U resulted in the increase of the volumes of pores with smaller diameters by the decrease of volumes of pores with longer ones, partly covering the surfaces of larger pores.

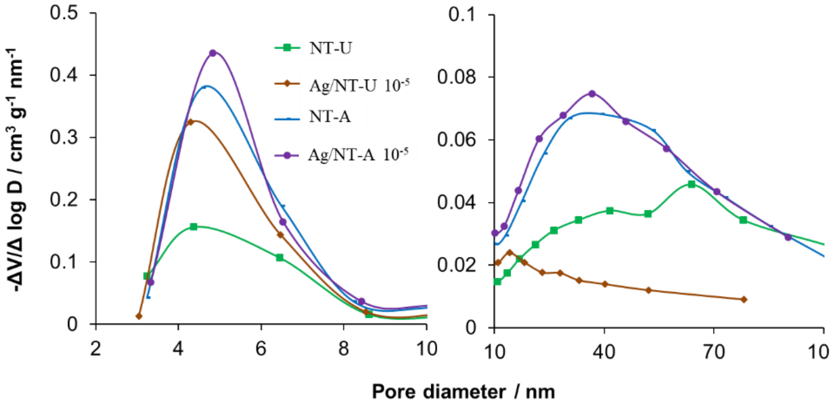

Figure 5.27. BJH pore-size distribution of the catalysts.

The XRD patterns of NT-U and NT-A catalysts are shown in Fig. 5.28. They clearly indicate that both NT-U and NT-A existed in pure anatase phase.

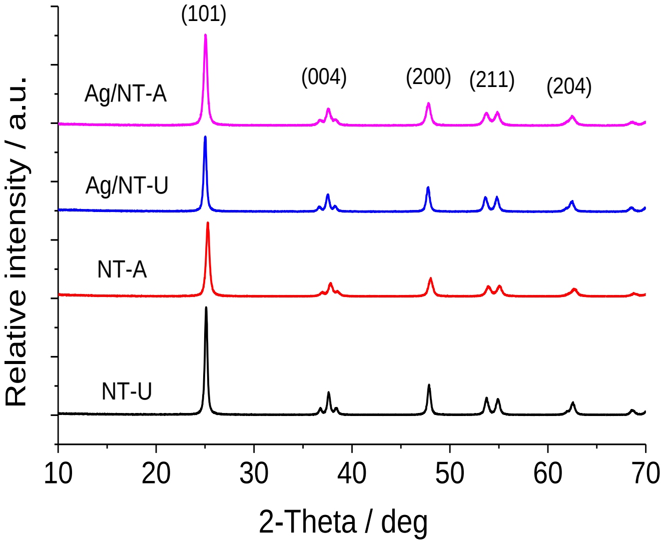

Figure 5.28. XRD patterns of the catalysts.

c(Ag) = 10^{-5} mol g^{-1} catalyst

The average of the crystallite size exhibited that the NT-U (25.2 nm) catalyst displayed a higher crystallite size compared to that of NT-A (19.0 nm) as shown in Table 5.5. It implies that application of different raw materials and preparation methods led to the formation of catalysts with identical crystalline phases, but different crystallite sizes.

Table 5.5. Crystallite size and band-gap energy of the catalysts prepared.

Catalyst	Crystallite size / nm	Band-gap energy / eV
NT-U	25.2	3.11
Ag/NT-U 10^{-6}	25.2	3.07
Ag/NT-U 10^{-5}	24.8	3.01
Ag/NT-U 10^{-4}	25.4	2.96
NT-A	19.0	3.12
Ag/NT-A 10^{-6}	17.3	3.06
Ag/NT-A 10^{-5}	18.8	3.01
Ag/NT-A 10^{-4}	17.4	2.98

Furthermore, no distinct silver signal was observed in the XRD spectra of Ag/NT-U and Ag/NT-A (Fig. 5.28). It is highly likely that the low amount of Ag-loading remained below the detection limit of the equipment. As a result, all diffraction peaks of the silver-modified catalysts (Ag/NT-U and Ag/NT-A) are rather similar to the unmodified ones (NT-U and NT-A). In addition, silver-modification at various concentrations did not significantly affect the crystallinity of the catalysts either (Table 5.5) [190,191]. *Zhou et al.* obtained a pure anatase phase for rod-like Ag/N-TiO_2 composites prepared by sol-gel method. The average crystallite size of the sample was 16.4 nm [192]. In addition, *Gao et al.* also reported a pure anatase phase of Ag/N-TiO_2 prepared by hydrothermal method, with the average crystallite size of about 36.1 nm [119].

The optical properties of the catalysts were investigated by using DRS analysis. Compared to bare TiO_2 (3.18 eV), N-doping resulted in longer-wavelength absorption edge extending into the visible range (3.11 eV for NT-U and 3.12 eV for NT-A), owing to a narrowed band-gap energy. In addition, the incorporation of silver nanoparticles on NT-U and NT-A also affected the band-gap energy [193]. Table 5.5 indicates that the band-gap energy slightly reduced upon increasing Ag concentration. The lowest band-gap energy was obtained for Ag/NT-U 10^{-4} with a value of 2.96 eV.

5.3.3 Photoactivity in the visible light

The photocatalytic activity (7-OHC formation) of Ag/NT-U and Ag/NT-A with various concentrations of Ag (as nanoparticles) were also investigated in coumarin solutions (Fig. A5.6). The photocatalytic performances were evaluated on the basis of the v_0 of 7-OHC formation. Silver-modification on the surface of NT-U catalyst remarkably enhanced the formation of 7-OHC to the v_0 of 14.9×10^{-10} M min^{-1} at the optimum Ag concentration of 10^{-6} mol g^{-1} as shown in Fig. 5.29 a.

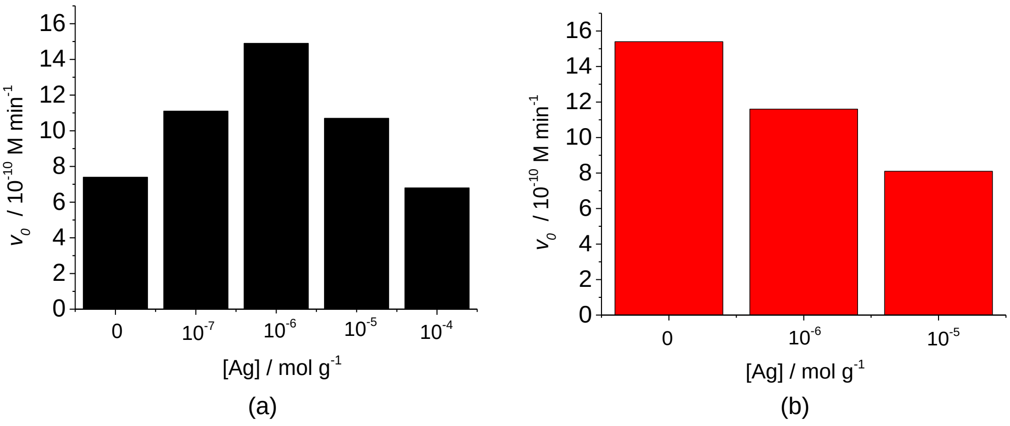

Figure 5.29. v_0 of 7-OHC formation in the presence of silver modified catalysts (a) Ag/NT-U and (b) Ag/NT-A.

c_0(coumarin) = 0.8×10^{-4} M, c(catalyst) = 1 g dm^{-3}, Vis LED (2nd arrangement), 20 dm^3 h^{-1} air

It is well known that silver-modification of such catalysts plays a crucial role in the photocatalytic activity, specifically trapping photo-generated electrons and, thus, promoting effective charge separations [147,194,195]. As mentioned in the previous literature, the Fermi level of Ag is lower than that of anatase TiO_2 and a Schottky barrier can be formed between the Ag and TiO_2 interface, which could serve as an efficient electron trap, thus preventing photoexcited electron-hole recombination [196]. In addition, Ag deposition could partially or fully protect the semiconductor surface from the solution environment, providing an enhancement of exchange current density, which is independent of the redox potential of the solution [52].

Furthermore, Ag-loading above 10^{-6} mol g^{-1} reduces the photocatalytic activity because too much silver on the catalyst surface could be detrimental to photonic efficiency. This phenomenon may be interpreted by consideration of several factors. As discussed above, silver nanoparticles can enhance the specific surfaces area of NT-U, which contribute to a better photocatalytic efficiency, along with the increased charge separation. However, the coverage of the active excitable sites on the catalyst surface reduces the amount of photons utilized for excitation of the semiconductor. Hence, these opposite effects led to a maximum efficiency at 10^{-6} mol g^{-1} silver concentration. The decrease of the active sites will be the dominant effect at higher Ag concentrations.

Earlier literatures also mentioned similar tendencies [18,197–200], but these works dealt only with silveration of bare TiO_2 catalysts (prepared by various methods) which were mostly applied for degradation of dyes or bacteria. In addition, *Gao et al.* also reported Ag-loading on the N-TiO_2 catalyst via hydrothermal procedure [119]. In this case, however, compared to Ag/NT-U produced in our work, beside the different preparation method, a rather high Ag concentration (0.92 mol %) proved to be the optimum for photocatalytic degradation of *RhB* under visible light. This value is two orders of magnitude higher than 10^{-6} mol g^{-1}, which corresponds to 0.008 mol %.

A significantly different tendency was observed at silver-modification on the surface of the hollow-structured NT-A catalyst (62 m^2 g^{-1} specific surface area).

A monotonous decrease in the photocatalytic activity was observed upon increasing the Ag concentration (to 10^{-6} mol g^{-1} and 10^{-5} mol g^{-1}), compared to the case of the unmodified NT-A (Fig. 5.29 b). While no appreciable increase of the specific surface area was caused by the Ag-loading of NT-A (Table 5.4), the accessible active sites monotonously decreased in this case, too. Therefore, the latter effect determined the results of silveration. The tendencies of coumarin degradation and quantum yield over Ag/NT-U and Ag/NT-A were in accordance with the 7-OHC formation as presented in Fig. A5.7.

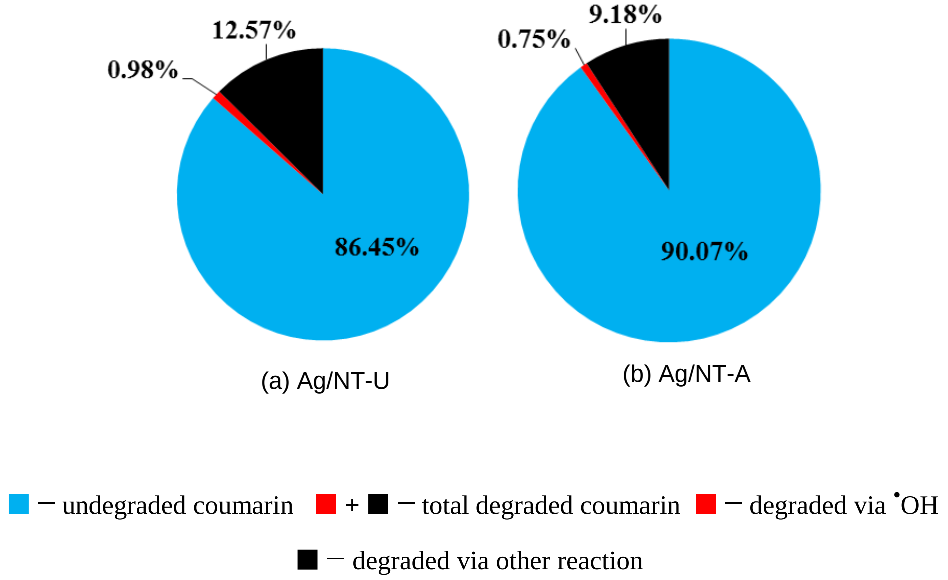

(a) Ag/NT-U

(b) Ag/NT-A

Figure 5.30. Photocatalytic pathways of different catalysts after 240 min irradiation. c_0(coumarin) = 0.8×10^{-4} M, c(catalyst) = 1 g dm^{-3}, Vis LED (2^{nd} arrangement), 20 dm^3 h^{-1} air

Furthermore, the comparison of the amounts of coumarin degraded and hydroxylated derivatives clearly indicated that transformation of the starting compound predominantly took place via pathways other than reactions with hydroxyl radicals. The results show that silver-loading of NT-U (with 10^{-6} mol g^{-1} Ag concentration) led to a significant increase of the transformation (degradation) in reactions with both hydroxyl radical from 0.54 % to 0.98% and other reactive species from 5.72 % to 12.57 % (Figs. 5.23 and 5.30 a). In the case of NT-A, Ag-loading (at same concentration) moderately decreased the coumarin transformation via hydroxyl radical reaction from 1.13 % to 0.75 % and other reactive species from 10.69 % to 9.18 % (Figs. 5.19 and 5.30 b). This tendency is in accordance with the results regarding 7-OHC formation in Fig 5.29.

5.3.4 Antibacterial study

The antibacterial effects of the catalysts were studied by using *Vibrio fischeri* bacteria as described in the Text A4.3. The catalysts were fixed in an acrylate based polymer on the surface of plastic sheets. The toxicity effects were measured by inhibition of the bioluminescence intensity of the bacterial suspension in contact with the catalysts (Fig. A5.8). A commercially available plastic sheet with antibacterial surface was used as a control sample for comparison.

Table 5.6. Antibacterial effects of various catalysts compared to the control sample after a 90-min contact.

Ag-loading / mol g^{-1}	**Ag/NT-U / %**	**Ag/NT-A / %**
0	40.4	30.0
10^{-6}	98.0	61.2
10^{-5}	70.0	52.2
10^{-4}	46.8	40.5

Table 5.6 indicates that silver doping on both NT-U and NT-A could enhance the toxicity effect compared to the unmodified catalysts. The effect of Ag could be attributed to the fact that when Ag nanoparticles interact with microorganisms such as bacteria, silver ions (Ag^+) are released and damage these organisms by attacking the negatively-charged cell walls, thereby deactivating cellular enzymes and disrupt membrane permeability; accordingly, cell lysis and cell death occur [201–203]. The maximum effects were observed at 10^{-6} mol g^{-1} Ag concentration for both Ag/NT-U and Ag/NT-A, with the values of 98 % and 61.2 %, respectively.

5.4 1,4-Hydroquinone photodegradation under visible light

The photocatalytic efficiencies of the catalysts prepared were also investigated by the degradation of 1,4-HQ, using a method based on the luminescence of the starting compound.

A blind probes (as comparisons) were measured: in the photolysis (1,4-HQ + Vis) and with catalyst in the dark (1,4-HQ + NT-U). In the both blind probes, a negligible change of the initial concentration of 1,4-HQ was observed (Fig. 5.31). However, in the presence of catalysts, 1,4-HQ was totally degraded after 180-min and 240-min irradiations with NT-A and NT-U, respectively.

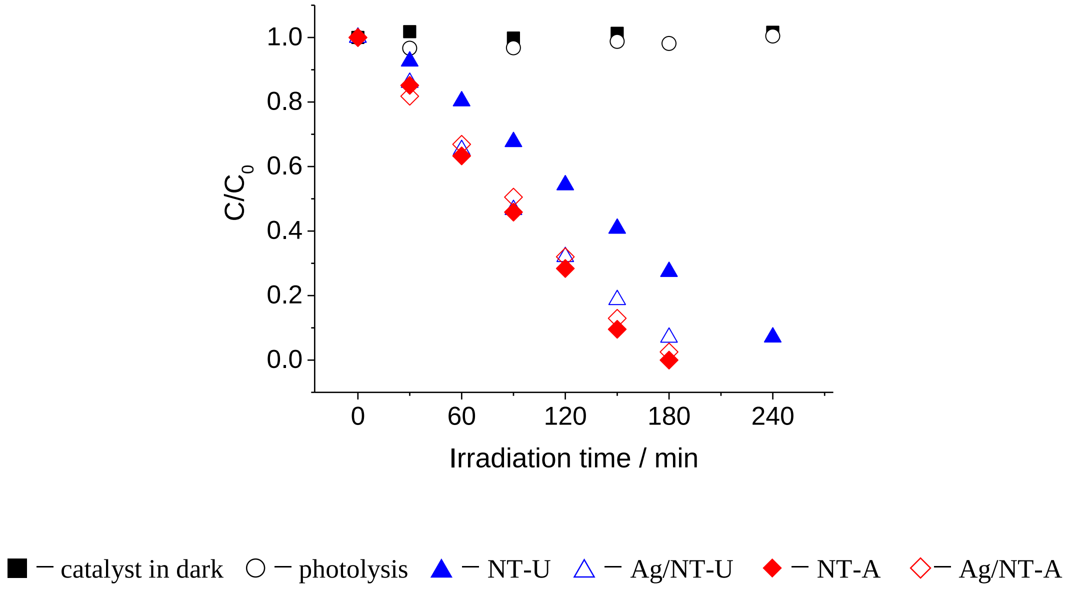

Figure 5.31. Degradation of 1,4-HQ over various catalysts.
c_0(1,4-HQ) = 2×10^{-4} M, c(catalyst) = 1 g dm^{-3}, Vis LED (2nd arrangement), 20 dm^3 h^{-1} air

These results are in full agreement with those obtained for the degradation of coumarin. The same is valid for the observations with the silverized catalysts with 10^{-6} mol g^{-1} Ag concentration. Accordingly, the photocatalytic degradation of 1,4-HQ on Ag/NT-U was significantly more efficient than on the unmodified NT-U catalyst. In contrast, Ag-loading of NT-A slightly decreased the degradation efficiency. The comparisons of the rate data obtained on the unmodified and silverized catalysts are shown in Table 5.7.

Table 5.7. Ratio (Ag/NT:NT) of 1,4-HQ degradation and coumarin reaction with other reactive species.

Catalyst	***v_0* (1,4-HQ) / 10^{-6} M min^{-1}**	**Ratio**	***v_0* (other reactive species) / 10^{-7} M min^{-1}**	**Ratio**
NT-U	5.10	1.88	0.233	2.00
Ag/NT-U 10^{-6}	9.60		0.468	
NT-A	10.00	0.92	0.379	0.91
Ag/NT-A 10^{-6}	9.20		0.344	

Beside the rates of 1,4-HQ degradation and their ratios (Ag/NT:NT), similar types of data are also shown regarding the reactions of coumarin with reactive species other than hydroxyl radicals (i.e. electrons or superoxide anion radicals). These agreements indicate that, similarly to coumarin, hydroxylation is not the main degradation route for 1,4-HQ. This observation confirms our previous results [204], showing that the cleavage of the aromatic ring takes place via reactions other than hydroxylation, and it needs the presence of dissolved oxygen.

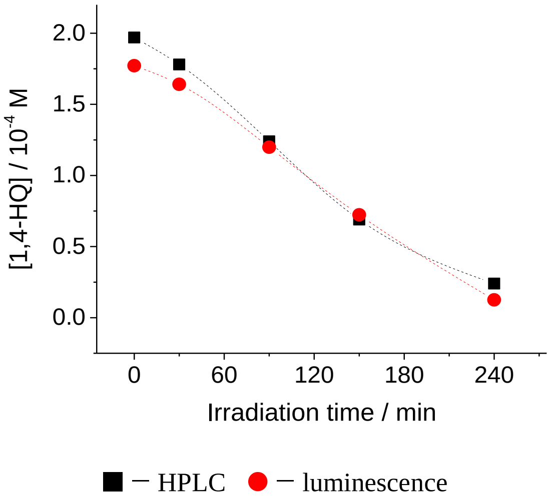

Figure 5.32. Comparison of HPLC and luminescence method for monitoring of photocatalytic 1,4-HQ degradation.

c_0(1,4-HQ) = 2×10^{-4} M, c(catalyst) = 1 g dm^{-3} NT-U, Vis LED (2nd arrangement), 20 dm^3 h^{-1} air

HPLC analyses were also performed in order to investigate the degradation of 1,4-HQ on the NT-U catalyst. The concentrations of 1,4-HQ measured by using HPLC technique were compared to those obtained by the luminescence method. The results regarding the photocatalytic degradation of 1,4-HQ were in full agreement as shown in Fig. 5.32. This comparison confirmed the reliable applicability of the faster and simpler luminescence method [152].

Total organic carbon (TOC) measurements were also carried out to clarify the mineralization process. The TOC representing the intermediates was estimated from the difference between the TOC concentration of the reaction mixture and that of the unreacted 1,4-HQ. The result indicated that the TOC concentration of intermediate products increased during the photodegradation, while the TOC of the reaction mixture steadily dropped from 14.6 mg dm^{-3} to 7.4 mg dm^{-3} (Fig. 5.33). It implies that a considerable part of the intermediates was mineralized to CO_2 and H_2O.

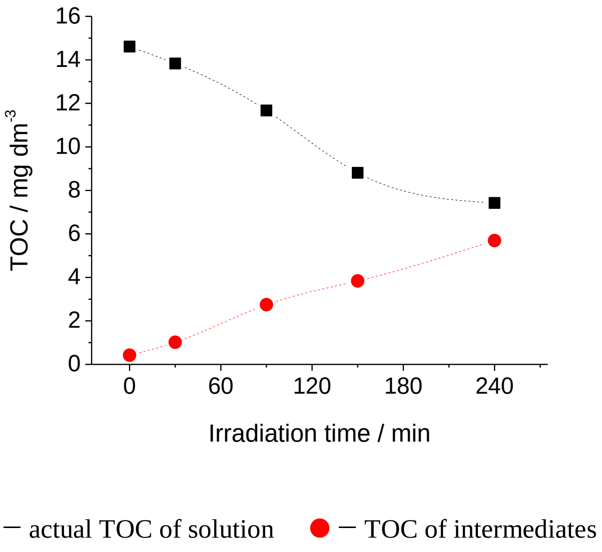

Figure 5.33. The change of TOC values during the photocatalytic experiment.
c_0(1,4-HQ) = 2×10^{-4} M, c(catalyst) = 1 g dm^{-3} NT-U, Vis LED (2nd arrangement), 20 dm^{3} h^{-1} air

The intermediates formed from 1,4-HQ are mostly short-chain acids as observed earlier in similar systems [26,129,131,132,205]. Generally, the produced *ROS* attack the phenyl ring of 1,4-HQ, producing dihydroxy derivatives (via hydroxyl radical reaction) or promoting aromatic ring cleavage (via superoxide anion radical reaction; k = 1.7×10^{7} $M^{-1}s^{-1}$ [206]). The mineralization of the intermediates, according to the TOC results, along with our earlier observation [204] that hydroxyl radical alone cannot cleave aromatic rings, confirm that other reactive photo-generated species (i.e. superoxide anion radicals) play crucial role in the degradation of these aromatic compounds.

6. Summary

Titanium dioxide is well known as one of the excellent photocatalysts for possible environmental application due to its low cost, low toxicity, outstanding chemical stability and unique photochemical properties. However, it has some drawbacks, which need to be improved for its practical application under visible light; e.g., the large band gap energy (~3.2 eV for anatase) and fast recombination of photo-generated electron-hole pairs. The present study aimed to overcome these problems by modification of TiO_2 with different elements such as N and Ag.

Visible-light-active N-TiO_2 catalysts were successfully prepared by a co-precipitation method, using ammonium hydroxide as nitrogen source (NT-A). Different dosing orders of the reagents resulted in deviating morphologies such as non-hollow and hollow structures obtained by the dosing orders of TTIP-H_2O-HNO_3-NH_4OH and HNO_3-NH_4OH-H_2O-TTIP, respectively. The investigation of photoactivity showed that the catalyst of hollow structure provided a more efficient generation of hydroxyl radical under visible light. Other operational parameters such as temperature of the synthesis and calcination time were optimized regarding the photocatalytic activity (with the values of 10 °C and 30 min). Furthermore, these optimum parameters were used for further experiments.

The catalysts calcined at various temperatures (350-650 °C) consisted of pure anatase phases. However, the nitrogen content decreased and the crystallite size increased by elevating the calcination temperature, which strongly affected the photocatalytic efficiency. NT-A catalysts calcined at 450 °C and 650 °C for 30 min showed the highest photocatalytic activity under visible and UV light, respectively. The band-gap energy of the catalysts increased from 3.01 eV to 3.17 eV upon increasing the calcination temperature and, thus, decreasing the nitrogen content.

Moreover, a sol-gel method, using urea as nitrogen source (NT-U) was applied for preparation of different catalysts. SEM images showed that the catalysts exhibited deviating morphologies; NT-U consisted non-hollow, while NT-A revealed hollow structure. Due to the non-hollow structure, the NT-U catalyst possessed a smaller specific surface area (32 $m^2\ g^{-1}$) compared to that of NT-A (61 $m^2\ g^{-1}$). As a consequence, the photocatalytic 7-OHC formation by NT-A in the visible light was significantly higher than that provided by the non-hollow NT-U, with the v_0 of 15.4×10^{-10} M min^{-1} and 7.4×10^{-10} M min^{-1}, respectively.

Furthermore, a facile photo-deposition method was used to decorate N-TiO_2 surfaces with Ag nanoparticles. No significant distinction was observed for the crystallite size after Ag modification. However, the band-gap energy slightly narrowed upon the increasing Ag concentration.

The Ag concentration played a critical role in the photoactivity of Ag/N-TiO_2. The optimum Ag concentration was 10^{-6} mol g^{-1} which could enhance the photoactivity of the non-hollow NT-U. The reaction of coumarin with hydroxyl radical and other species (i.e. electrons or superoxide anion radicals) appreciably increased after silveration, from 0.54 % to 0.98 % for hydroxyl radical; and from 5.72 % to 12.57 % for other species. However, Ag-loading on the hollow surface of NTA was not favorable for photocatalytic enhancement. It could be attributed to the specific surface area after silveration; its value increased for Ag/NT-U (from 32 m^2 g^{-1} to 47 m^2 g^{-1}), but hardly changed for Ag/NT-A (from 61 m^2 g^{-1} to 62 m^2 g^{-1}). In addition, the purpose of silveration was also to make these catalysts efficiently antibacterial against *Vibrio fischeri* strain. Ag/NT-U with 10^{-6} mol g^{-1} Ag concentration proved to be optimal, considering both photocatalytic and disinfectional activities.

Coumarin was used as a chemical probe for the monitoring of hydroxyl radical formation by production of hydroxylated derivatives. The reaction of coumarin with other species (instead of hydroxyl radical) was determined from the difference between the amounts of hydroxylated derivatives formed and coumarin degraded. The results exhibited that coumarin efficiently reacted with photo-generated electrons (anaerobic) and superoxide anion radicals (in aerobic system). Therefore, we have unambiguously proved that beside as hydroxyl radical scavenger, coumarin could also be used to estimate the production of other species (i.e. electrons or superoxide anion radicals).

A similar phenomenon was also observed for 1,4-HQ as a pollutant model compound, the photodegradation of which in visible light took place predominantly through the cleavage of the aromatic ring via reactions with other species (i.e. superoxide anion radicals), instead of hydroxylation via reaction with hydroxyl radical.

7. Thesis Points of PhD Dissertation

I. The dosing order of precursors (N and Ti) and the calcination temperature remarkably affect the surface morphology and photoactivity of N-doped TiO_2 catalysts.

1. The hollow structure of catalyst prepared by the dosing order of (HNO_3-NH_4OH-H_2O-TTIP) exhibited a higher photoactivity under visible light, regarding the hydroxyl radical formation, compared to the non-hollow catalyst synthesized by an other sequence of these reagents (TTIP-H_2O-HNO_3-NH_4OH).
2. The calcination temperature of the catalysts (at optimum parameters of the synthesis temperature and calcination time) strongly influenced the nitrogen content and crystallite size, which played important roles in the photoactivity. The catalysts calcined at 450 °C and 650 °C showed the highest photocatalytic activity under visible and UV light, respectively.

Wafi, A.; Szabó-Bárdos, E.; Horváth, O.; Makó, É.; Jakab, M.; Zsirka, B. Coumarin-based quantification of hydroxyl radicals and other reactive species generated on excited nitrogen-doped TiO_2. *J. Photochem. Photobiol. A Chem.* **2021**, *404*, 112913
doi:10.1016/j.jphotochem.2020.112913.

II. The specific surface area played a crucial role on the photocatalytic performance of nitrogen-doped TiO_2.

1. The SEM images of N-TiO_2 (Urea) displayed a non-hollow structure on the surface of the catalyst, which resulted in a smaller specific surface area (32 m^2 g^{-1}) compared to the hollow N-TiO_2 (Ammonia; 61 m^2 g^{-1}).
2. This specific surface area (corresponding to the adsorption behavior of the catalysts) played a critical role in the photocatalytic hydroxyl radical production. As a result, the initial rate of 7-OHC formation for N-TiO_2 (Ammonia) in visible-light irradiation was about twice as high (15.4×10^{-10} M min^{-1}) as that for N-TiO_2 (Urea; 7.4×10^{-10} M min^{-1}).

Wafi, A.; Szabó-Bárdos, E.; Horváth, O.; Pósfai, M.; Makó, É.; Juzsakova, T.; Fónagy, O. The photocatalytic and antibacterial performance of nitrogen-doped TiO_2: Surface-structure dependence and silver-deposition effect. *Nanomaterials* **2020**, *10*, 2261
doi:10.3390/nano10112261.

III. The effect of silver modification toward photocatalytic and antibacterial activities depended on the surface morphology of the nitrogen-doped catalysts.

1. The Ag concentration of the catalysts played a critical role in the photoactivity of Ag/N-TiO_2. The optimum Ag concentration (as low as 10^{-6} mol g^{-1}) could double the photocatalytic efficiency of the non-hollow N-TiO_2 (Urea), regarding the formation of hydroxyl radical and superoxide anion radical. However, Ag-loading on the hollow surface of N-TiO_2 (Ammonia), at the same concentration, decreased the photoactivity.
2. The specific surface area of the non-hollow structure of N-TiO_2 (Urea; 32 m^2 g^{-1}) could be significantly increased by silver modification (to 47 m^2 g^{-1} by 10^{-6} mol g^{-1} Ag concentration) because the surfaces of the deposited metal particles were considerably larger than the area they covered on the catalyst.
3. N-TiO_2 (Ammonia; 61 m^2 g^{-1}) possessed surficial holes with rather bent walls. Hence, deposition of Ag nanoparticles (10^{-6} mol g^{-1}) on these walls could not appreciably enhance the surface area (62 m^2 g^{-1}); their own surface hardly exceeded the occupied area on the catalyst.
4. The toxicity effects of the non-hollow Ag/N-TiO_2 (Urea) catalysts toward *Vibrio fischeri* bacteria were significantly higher than the corresponding values for the hollow-structure Ag/N-TiO_2 (Ammonia).

Wafi, A.; Szabó-Bárdos, E.; Horváth, O.; Pósfai, M.; Makó, É.; Juzsakova, T.; Fónagy, O. The photocatalytic and antibacterial performance of nitrogen-doped TiO_2: Surface-structure dependence and silver-deposition effect. *Nanomaterials* **2020**, *10*, 2261
doi:10.3390/nano10112261.

IV. Coumarin can be used as a single chemical probe to detect both the formation of hydroxyl radical and other reactive species.

1. During the photocatalytic experiments, the formation of 7-OHC (i.e., hydroxylated coumarins) and coumarin degradation were monitored under anaerobic and aerobic atmospheres.
2. The formation of hydroxylated coumarins corresponded to the reactions of coumarin with hydroxyl radicals. The difference between the amounts of the hydroxylated derivatives formed and the degraded coumarin represented the part of coumarin which reacted with other species (i.e. electrons or superoxide anion radicals).
3. Conventionally, coumarin is only applied as a hydroxyl radical scavenger, however, in this study it could also be used to estimate the production of other reactive species (i.e. electrons or superoxide anion radicals).

Wafi, A.; Szabó-Bárdos, E.; Horváth, O.; Makó, É.; Jakab, M.; Zsirka, B. Coumarin-based quantification of hydroxyl radicals and other reactive species generated on excited nitrogen-doped TiO_2. *J. Photochem. Photobiol. A Chem.* **2021**, *404*, 112913
doi:10.1016/j.jphotochem.2020.112913.

V. Instead of dyes, the colorless 1,4-hydroquinone proved to be a promising model compound for photocatalytic experiments under visible-light illumination.

1. 1,4-Hydroquinone was totally decomposed after a 240-min visible-light irradiation in the presence of both unmodified (N-TiO_2) and modified (Ag/N-TiO_2) catalysts.
2. The ratio of the photocatalytic efficiencies (Ag/N-TiO_2:N-TiO_2) was similar to the data obtained from the reactions of coumarin with other species (i.e. electrons or superoxide anion radicals), indicating that these photo-generated agents played vital roles in the degradation processes of 1,4-hydroquinone.

Wafi, A.; Szabó-Bárdos, E.; Horváth, O.; Pósfai, M.; Makó, É.; Juzsakova, T.; Fónagy, O. The photocatalytic and antibacterial performance of nitrogen-doped TiO_2: Surface-structure dependence and silver-deposition effect. *Nanomaterials* **2020**, *10*, 2261
doi:10.3390/nano10112261.

8. References

1. Mahamuni, N.N.; Adewuyi, Y.G. *Ultrason. Sonochem.* **2010**, *17*, 990–1003.
2. Gaya, U.I.; Abdullah, A.H. *J. Photochem. Photobiol. C Photochem. Rev.* **2008**, *9*, 1–12.
3. Basavarajappa, P.S.; Patil, S.B.; Ganganagappa, N.; Reddy, K.R.; Raghu, A. V.; Reddy, C.V. *Int. J. Hydrogen Energy* **2020**, *45*, 7764–7778.
4. Wetchakun, K.; Wetchakun, N.; Sakulsermsuk, S. *J. Ind. Eng. Chem.* **2019**, *71*, 19–49.
5. Guba, S.; Somogyi, V.; Szabó-Bárdos, E. *Hungarian J. Ind. Chem.* **2015**, *43*, 39–44.
6. Tong, A.Y.C.; Braund, R.; Warren, D.S.; Peake, B.M. *Cent. Eur. J. Chem.* **2012**, *10*, 989–1027.
7. Rueda-Marquez, J.J.; Levchuk, I.; Fernández Ibañez, P.; Sillanpaa, M. *J. Clean. Prod.* **2020**, *258*, 120694.
8. Bethi, B.; Sonawane, S.H.; Bhanvase, B.A.; Gumfekar, S.P. *Chem. Eng. Process. Process Intensif.* **2016**, *109*, 178–189.
9. Sułek, A.; Pucelik, B.; Kobielusz, M.; Łabuz, P.; Dubin, G.; Dąbrowski, J.M. *Catalysts* **2019**, *9*, 821.
10. Yu, B.; Zhou, Y.; Li, P.; Tu, W.; Li, P.; Tang, L.; Ye, J.; Zou, Z. *Nanoscale* **2016**, *8*, 11870–11874.
11. Vargas-Hernández, J.; Coste, S.; García Murillo, A.; Carrillo Romo, F.; Kassiba, A. *J. Alloys Compd.* **2017**, *710*, 355–363.
12. Marques, J.; Gomes, T.D.; Forte, M.A.; Silva, R.F.; Tavares, C.J. *Catal. Today* **2019**, 36–45.
13. González-Torres, J.C.; Poulain, E.; Domínguez-Soria, V.; García-Cruz, R.; Olvera-Neria, O. *Int. J. Photoenergy* **2018**, *2018*, 1–12.
14. Asahi, R.; Morikawa, T.; Irie, H.; Ohwaki, T. *Chem. Rev.* **2014**, *114*, 9824–9852.
15. Ravindranath, R.; Roy, P.; Periasamy, A.P.; Chang, H.T. *RSC Adv.* **2014**, *4*, 57290–57296.
16. Jaafar, N.F.; Jalil, A.A.; Triwahyono, S.; Shamsuddin, N. *RSC Adv.* **2015**, *5*, 90991–91000.
17. Zielińska-Jurek, A.; Hupka, J. *Catal. Today* **2014**, *230*, 181–187.
18. Ali, T.; Ahmed, A.; Alam, U.; Uddin, I.; Tripathi, P.; Muneer, M. *Mater. Chem. Phys.* **2018**, *212*, 325–335.
19. Sanchez-Martinez, A.; Ceballos-Sanchez, O.; Koop-Santa, C.; López-Mena, E.R.; Orozco-Guareño, E.; García-Guaderrama, M. *Ceram. Int.* **2018**, *44*, 5273–5283.
20. Cheng, X.; Yu, X.; Xing, Z.; Yang, L. *Arab. J. Chem.* **2016**, *9*, S1706–S1711.

21. Katoueizadeh, E.; Zebarjad, S.M.; Janghorban, K. *J. Mater. Res. Technol.* **2018**, *7*, 204–211.

22. Sacco, O.; Stoller, M.; Vaiano, V.; Ciambelli, P.; Chianese, A.; Sannino, D. *Int. J. Photoenergy* **2012**, *2012*, 1–8.

23. Vaiano, V.; Sacco, O.; Sannino, D.; Ciambelli, P. *Appl. Catal. B Environ.* **2015**, *170–171*, 153–161.

24. Wafi, A.; Szabó-Bárdos, E.; Horváth, O.; Makó, É.; Jakab, M.; Zsirka, B. *J. Photochem. Photobiol. A Chem.* **2021**, *404*, 112913.

25. Enguita, F.J.; Leitão, A.L. *Biomed Res. Int.* **2013**, *2013*, 1–14.

26. Feng, C.; Chen, Z.; Jing, J.; Hou, J. *J. Mater. Chem. C* **2020**, *8*, 3000–3009.

27. Baniamerian, H.; Tsapekos, P.; Alvarado-Morales, M.; Shokrollahzadeh, S.; Safavi, M.; Angelidaki, I. *Inorg. Chem. Commun.* **2020**, *116*, 107936.

28. Cesaro, A.; Naddeo, V.; Belgiorno, V. *J. Bioremediation Biodegrad.* **2013**, *4*, 1–8.

29. Wang, J.L.; Xu, L.J. *Crit. Rev. Environ. Sci. Technol.* **2012**, *42*, 251–325.

30. Das, S.; Wan Daud, W.M.A. *Renew. Sustain. Energy Rev.* **2014**, *39*, 765–805.

31. Cerreta, G.; Roccamante, M.A.; Oller, I.; Malato, S.; Rizzo, L. *Chemosphere* **2019**, *236*, 124354.

32. Cuerda-Correa, E.M.; Alexandre-Franco, M.F.; Fernández-González, C. *Water (Switzerland)* **2020**, *12*, 102.

33. Zhao, Y.; Kuang, J.; Zhang, S.; Li, X.; Wang, B.; Huang, J.; Deng, S.; Wang, Y.; Yu, G. *J. Hazard. Mater.* **2017**, *323*, 460–470.

34. Kıdak, R.; Doğan, Ş. *Ultrason. Sonochem.* **2018**, *40*, 131–139.

35. Alharbi, S.K.; Price, W.E.; Kang, J.; Fujioka, T.; Nghiem, L.D. *Desalin. Water Treat.* **2016**, *57*, 29340–29351.

36. Kanakaraju, D.; Glass, B.D.; Oelgemöller, M. *J. Environ. Manage.* **2018**, *219*, 189–207.

37. Alalm, M.G.; Tawfik, A.; Ookawara, S. *J. Environ. Chem. Eng.* **2015**, *3*, 46–51.

38. Corma, A.; Garcia, H. *J. Catal.* **2013**, *308*, 168–175.

39. Julkapli, N.M.; Bagheri, S.; Bee-Abd-Hamid, S. *Sci. World J.* **2014**, *2014*, 1–25.

40. Barry, T.I.; Stone, F.S. *Proc. R. Soc. London. Ser. A. Math. Phys. Sci.* **1960**, *255*, 124–144.

41. Djeghri, N.; Formenti, M.; Juillet, F.; Teichner, S.J. *Faraday Discuss. Chem. Soc.* **1974**, *58*, 185–193.

42. Fujishima, A.; Honda, K. *Nature* **1972**, *238*, 37–38.

43. Pawar, R.C.; Lee, C.S. *William Andrew* **2015**, 1–7.

44. Singh, P.; Sharma, K.; Hasija, V.; Sharma, V.; Sharma, S.; Raizada, P.; Singh, M.; Saini, A.K.; Hosseini-Bandegharaei, A.; Thakur, V.K. *Mater. Today Chem.* **2019**, *14*, 100186.

45. Fox, M.A.; Dulay, M.T. *Chem. Rev.* **1993**, *93*, 341–357.

46. Dong, S.; Feng, J.; Fan, M.; Pi, Y.; Hu, L.; Han, X.; Liu, M.; Sun, J.; Sun, J. *RSC Adv.* **2015**, *5*, 14610–14630.

47. Kisch, H. *Angew. Chemie - Int. Ed.* **2013**, *52*, 812–847.

48. Yang, X.; Wang, D. *Semicond. Semimetals* **2017**, *97*, 47–80.

49. Memming, R. *Wiley* **2000**, 1–486.

50. Melikov, R. *Master's Thesis, Koc Univ.* **2016**, 1–105.

51. Tan, H.L.; Abdi, F.F.; Ng, Y.H. *Chem. Soc. Rev.* **2019**, *48*, 1255–1271.

52. Joe, J.; Yang, H.; Bae, C.; Shin, H. *Catalysts* **2019**, *9*, 149.

53. Harrison, S. *Master's Thesis, Lancaster Univ.* **2016**, 1–199.

54. Thurston, T.R.; Wilcoxon, J.P. *J. Phys. Chem. B* **1999**, *103*, 11–17.

55. Wu, W.; Zhang, S.; Zhou, J.; Xiao, X.; Ren, F.; Jiang, C. *Chem. - A Eur. J.* **2011**, *17*, 9708–9719.

56. Chen, D.; Huang, F.; Ren, G.; Li, D.; Zheng, M.; Wang, Y.; Lin, Z. *Nanoscale* **2010**, *2*, 2062–2064.

57. Wu, W.; Xiao, X.; Zhang, S.; Zhou, J.; Ren, F.; Jiang, C. *Chem. Lett.* **2010**, *39*, 684–685.

58. Makama, A.B.; Umar, M.; Saidu, S.A. *InTech* **2018**, 111–136.

59. Vinu, R.; Madras, G. *J. Indian Inst. Sci.* **2010**, *90*, 189–230.

60. Kudo, A.; Miseki, Y. *Chem. Soc. Rev.* **2009**, *38*, 253–278.

61. Cheng, L.; Xiang, Q.; Liao, Y.; Zhang, H. *Energy Environ. Sci.* **2018**, *11*, 1362–1391.

62. Ong, C.B.; Ng, L.Y.; Mohammad, A.W. *Renew. Sustain. Energy Rev.* **2018**, *81*, 536–551.

63. Etacheri, V.; Di Valentin, C.; Schneider, J.; Bahnemann, D.; Pillai, S.C. *J. Photochem. Photobiol. C Photochem. Rev.* **2015**, *25*, 1–29.

64. Wu, W.; Jiang, C.; Roy, V.A.L. *Nanoscale* **2015**, *7*, 38–58.

65. Selloni, A. *Nat. Mater.* **2008**, *7*, 613–615.

66. Xie, Y.P.; Liu, G.; Yin, L.; Cheng, H.M. *J. Mater. Chem.* **2012**, *22*, 6746–6751.

67. Pan, J.; Liu, G.; Lu, G.Q.; Cheng, H.M. *Angew. Chemie - Int. Ed.* **2011**, *50*, 2133–2137.

68. Ye, L.; Mao, J.; Peng, T.; Zan, L.; Zhang, Y. *Phys. Chem. Chem. Phys.* **2014**, *16*, 15675–15680.

69. Sajan, C.P.; Wageh, S.; Al-Ghamdi, A.A.; Yu, J.; Cao, S. *Nano Res.* **2016**, *9*, 3–27.

70. Pan, J.; Wu, X.; Wang, L.; Liu, G.; Lu, G.Q.; Cheng, H.M. *Chem. Commun.* **2011**, *47*, 8361–8363.

71. Xu, H.; Ouyang, S.; Li, P.; Kako, T.; Ye, J. *ACS Appl. Mater. Interfaces* **2013**, *5*, 1348–1354.

72. Liu, G.; Sun, C.; Yang, H.G.; Smith, S.C.; Wang, L.; Lu, G.Q.; Cheng, H.M. *Chem. Commun.* **2010**, *46*, 755–757.

73. Xiong, Z.; Lei, Z.; Li, Y.; Dong, L.; Zhao, Y.; Zhang, J. *J. Photochem. Photobiol. C Photochem. Rev.* **2018**, *36*, 24–47.

74. Li, R.; Li, T.; Zhou, Q. *Catalysts* **2020**, *10*, 804.

75. Li, Z.; Fang, Y.; Zhan, X.; Xu, S. *J. Alloys Compd.* **2013**, *564*, 138–142.

76. Shang, J.; Zhao, F.; Zhu, T.; Li, J. *Sci. China Chem.* **2011**, *54*, 167–172.

77. Murcia, J.J.; Ávila-Martínez, E.G.; Rojas, H.; Cubillos, J.; Ivanova, S.; Penkova, A.; Laguna, O.H. *Nanomaterials* **2019**, *9*, 517.

78. Reddy, P.A.K.; Reddy, P.V.L.; Kwon, E.; Kim, K.H.; Akter, T.; Kalagara, S. *Environ. Int.* **2016**, *91*, 94–103.

79. Mehrabian, M.; Dalir, S. *Optik (Stuttg).* **2018**, *169*, 214–223.

80. Yang, M. *PhD's Thesis, Univ. Pittsburgh* **2012**, 1–142.

81. Afzal, S.; Daoud, W.A.; Langford, S.J. *ACS Appl. Mater. Interfaces* **2013**, *5*, 4753–4759.

82. Wu, S.H.; Wu, J.L.; Jia, S.Y.; Chang, Q.W.; Ren, H.T.; Liu, Y. *Appl. Surf. Sci.* **2013**, *287*, 389–396.

83. Sekar, N.; Gehlot, V.Y. *Resonance* **2010**, *15*, 819–831.

84. Yamazaki, Y.; Takeda, H.; Ishitani, O. *J. Photochem. Photobiol. C Photochem. Rev.* **2015**, *25*, 106–137.

85. Gholamkhass, B.; Mametsuka, H.; Koike, K.; Tanabe, T.; Furue, M.; Ishitani, O. *Inorg. Chem.* **2005**, *44*, 2326–2336.

86. Bae, E.; Choi, W. *Environ. Sci. Technol.* **2003**, *37*, 147–152.

87. Iliev, V.; Tomova, D.; Bilyarska, L.; Eliyas, A.; Petrov, L. *Appl. Catal. B Environ.* **2006**, *63*, 266–271.

88. Jin, Z.; Zhang, X.; Lu, G.; Li, S. *J. Mol. Catal. A Chem.* **2006**, *259*, 275–280.

89. Zhang, H.; Chen, G.; Bahnemann, D.W. *J. Mater. Chem.* **2009**, *19*, 5089–5121.

90. Tada, H.; Kiyonaga, T.; Naya, S.I. *Chem. Soc. Rev.* **2009**, *38*, 1849–1858.

91. Zheng, Z.; Huang, B.; Qin, X.; Zhang, X.; Dai, Y.; Whangbo, M.H. *J. Mater. Chem.* **2011**, *21*, 9079–9087.

92. Murdoch, M.; Waterhouse, G.I.N.; Nadeem, M.A.; Metson, J.B.; Keane, M.A.; Howe, R.F.; Llorca, J.; Idriss, H. *Nat. Chem.* **2011**, *3*, 489–492.

93. Li, X.; Zhuang, Z.; Li, W.; Pan, H. *Appl. Catal. A Gen.* **2012**, *429–430*, 31–38.

94. Dunnill, C.W.; Ansari, Z.; Kafizas, A.; Perni, S.; Morgan, D.J.; Wilson, M.; Parkin, I.P. *J. Mater. Chem.* **2011**, *21*, 11854–11861.

95. Liu, C.; Yang, D.; Jiao, Y.; Tian, Y.; Wang, Y.; Jiang, Z. *ACS Appl. Mater. Interfaces* **2013**, *5*, 3824–3832.

96. Sun, M.; Fang, Y.; Sun, S.; Wang, Y. *RSC Adv.* **2016**, *6*, 12272–12279.

97. Bhardwaj, S.; Sharma, D.; Kumari, P.; Pal, B. *Opt. Mater. (Amst).* **2020**, *106*, 109975.

98. Rabhi, S.; Belkacemi, H.; Bououdina, M.; Kerrami, A.; Ait Brahem, L.; Sakher, E. *Mater. Lett.* **2019**, *236*, 640–643.

99. Patil, S.B.; Basavarajappa, P.S.; Ganganagappa, N.; Jyothi, M.S.; Raghu, A. V.; Reddy, K.R. *Int. J. Hydrogen Energy* **2019**, *44*, 13022–13039.

100. Jiang, Z.; Lv, X.; Jiang, D.; Xie, J.; Mao, D. *J. Mater. Chem. A* **2013**, *1*, 14963–14972.

101. Karafas, E.S.; Romanias, M.N.; Stefanopoulos, V.; Binas, V.; Zachopoulos, A.; Kiriakidis, G.; Papagiannakopoulos, P. *J. Photochem. Photobiol. A Chem.* **2019**, *371*, 255–263.

102. Elmehasseb, I.; Kandil, S.; Elgendy, K. *Optik (Stuttg).* **2020**, *213*, 164654.

103. Caratto, V.; Setti, L.; Campodonico, S.; Carnasciali, M.M.; Botter, R.; Ferretti, M. *J. Sol-Gel Sci. Technol.* **2012**, *63*, 16–22.

104. Zhang, C.; Liu, Y.; Zhou, J.; Jin, W.; Chen, W. *Dye. Pigment.* **2018**, *156*, 213–218.

105. Li, T.; Abdelhaleem, A.; Chu, W.; Pu, S.; Qi, F.; Zou, J. *Chem. Eng. J.* **2021**, *411*, 128450.

106. Liu, S.; Chen, X.; Chen, X. *Chinese J. Catal.* **2006**, *27*, 697–702.

107. Prabakar, K.; Takahashi, T.; Nezuka, T.; Takahashi, K.; Nakashima, T.; Kubota, Y.; Fujishima, A. *J. Vac. Sci. Technol. A Vacuum, Surfaces, Film.* **2007**, *25*, 1188–1192.

108. Maeda, M.; Watanabe, T. *J. Electrochem. Soc.* **2006**, *153*, C186.

109. Shifu, C.; Lei, C.; Shen, G.; Gengyu, C. *Chem. Phys. Lett.* **2005**, *413*, 404–409.

110. Gurkan, Y.Y.; Turkten, N.; Hatipoglu, A.; Cinar, Z. *Chem. Eng. J.* **2012**, *184*, 113–124.

111. Than, L.D.; Luong, N.S.; Ngo, V.D.; Tien, N.M.; Dung, T.N.; Nghia, N.M.; Loc, N.T.; Thu, V.T.; Lam, T.D. *J. Electron. Mater.* **2017**, *46*, 158–166.

112. Suwannaruang, T.; Kidkhunthod, P.; Chanlek, N.; Soontaranon, S.; Wantala, K. *Appl. Surf. Sci.* **2019**, *478*, 1–14.

113. Yang, G.; Jiang, Z.; Shi, H.; Xiao, T.; Yan, Z. *J. Mater. Chem.* **2010**, *20*, 5301–5309.

114. Cheng, X.; Yu, X.; Xing, Z. *Appl. Surf. Sci.* **2012**, *258*, 3244–3248.

115. Abdelhaleem, A.; Chu, W. *J. Hazard. Mater.* **2017**, *338*, 491–501.

116. Suwannaruang, T.; Kamonsuangkasem, K.; Kidkhunthod, P.; Chirawatkul, P.; Saiyasombat, C.; Chanlek, N.; Wantala, K. *Mater. Res. Bull.* **2018**, *105*, 265–276.

117. Giannakas, A.E.; Antonopoulou, M.; Daikopoulos, C.; Deligiannakis, Y.; Konstantinou, I. *Appl. Catal. B Environ.* **2016**, *184*, 44–54.

118. Mancuso, A.; Sacco, O.; Sannino, D.; Pragliola, S.; Vaiano, V. *Arab. J. Chem.* **2020**, *13*, 8347–8360.

119. Gao, Y.; Fang, P.; Chen, F.; Liu, Y.; Liu, Z.; Wang, D.; Dai, Y. *Appl. Surf. Sci.* **2013**, *265*, 796–801.

120. Gaidau, C.; Petica, A.; Ignat, M.; Iordache, O.; Ditu, L.M.; Ionescu, M. *Open Chem.* **2016**, *14*, 383–392.

121. Yang, G.; Yin, H.; Liu, W.; Yang, Y.; Zou, Q.; Luo, L.; Li, H.; Huo, Y.; Li, H. *Appl. Catal. B Environ.* **2018**, *224*, 175–182.

122. Dziedzic, A.; Bochnowski, W.; Adamiak, S.; Szyller; Cebulski, J.; Virt, I.; Kus-Liśkiewicz, M.; Marzec, M.; Potera, P.; Żaczek, A.; et al. *Surf. Coatings Technol.* **2020**, *393*, 125844.

123. Leandri, V.; Gardner, J.M.; Jonsson, M. *J. Phys. Chem. C* **2019**, *123*, 6667–6674.

124. Gomes, J.; Lincho, J.; Domingues, E.; Quinta-Ferreira, R.M.; Martins, R.C. *Water (Switzerland)* **2019**, *11*, 373.

125. Houndedjihou, D.; Kodom, T.; Dougna, A.A.; Tchakala, I.; Djaneye-Boundjou, G.; Bawa, L.M. *Chem. Sci. Int. J.* **2018**, *4*, 1–10.

126. Nguyen, T.P.; Tran, Q.B.; Ly, Q.V.; Thanh Hai, L.; Le, D.T.; Tran, M.B.; Ho, T.T.T.; Nguyen, X.C.; Shokouhimehr, M.; Vo, D.V.N.; et al. *Arab. J. Chem.* **2020**, *13*, 8361–8371.

127. Rajoriya, S.; Bargole, S.; George, S.; Saharan, V.K.; Gogate, P.R.; Pandit, A.B. *Sep. Purif. Technol.* **2019**, *209*, 254–269.

128. O’Donoghue, J.L. *J. Cosmet. Dermatol.* **2006**, *5*, 196–203.

129. Tao, Y.; Cheng, Z.L.; Ting, K.E.; Yin, X.J. *J. Catal.* **2013**, *2013*, 1–6.

130. Santos, A.; Yustos, P.; Quintanilla, A.; García-Ochoa, F.; Casas, J.A.; Rodriguez, J.J. *Environ. Sci. Technol.* **2004**, *38*, 133–138.

131. Wysocka, I.; Kowalska, E.; Trzciński, K.; Łapiński, M.; Nowaczyk, G.; Zielińska-Jurek, A. *Nanomaterials* **2018**, *8*, 1–20.

132. Azizi, A.; Abouseoud, M.; Amrane, A. *Nat. Environ. Pollut. Technol.* **2017**, *16*, 321–330.

133. Nosaka, Y.; Nosaka, A.Y. *Chem. Rev.* **2017**, *117*, 11302–11336.

134. Žerjav, G.; Albreht, A.; Vovk, I.; Pintar, A. *Appl. Catal. A Gen.* **2020**, 117566.

135. Bubacz, K.; Kusiak-Nejman, E.; Tryba, B.; Morawski, A.W. *J. Photochem. Photobiol. A Chem.* **2013**, *261*, 7–11.

136. Page, S.E.; Arnold, W.A.; McNeill, K. *J. Environ. Monit.* **2010**, *12*, 1658–1665.

137. Zhang, J.; Nosaka, Y. *J. Phys. Chem. C* **2013**, *117*, 1383–1391.

138. Louit, G.; Foley, S.; Cabillic, J.; Coffigny, H.; Taran, F.; Valleix, A.; Renault, J.P.; Pin, S. *Radiat. Phys. Chem.* **2005**, *72*, 119–124.

139. Czili, H.; Horváth, A. *Appl. Catal. B Environ.* **2008**, *81*, 295–302.

140. Baldacchino, G.; Maeyama, T.; Yamashita, S.; Taguchi, M.; Kimura, A.; Katsumura, Y.; Murakami, T. *Chem. Phys. Lett.* **2009**, *468*, 275–279.

141. Manevich, Y.; Held, K.D.; Biaglow, J.E. *Radiat. Res.* **1997**, *148*, 580.

142. Jing, J.G.; Ke, H.X.; Ji, X.H.; Huang, H.; Tang, B. *J. Agric. Food Chem.* **2006**, *54*, 7968–7972.

143. Fernández-Castro, P.; Vallejo, M.; San Román, M.F.; Ortiz, I. *J. Chem. Technol. Biotechnol.* **2015**, *90*, 796–820.

144. Lu, C.; Song, G.; Lin, J.M. *TrAC - Trends Anal. Chem.* **2006**, *25*, 985–995.

145. Khan, P.; Idrees, D.; Moxley, M.A.; Corbett, J.A.; Ahmad, F.; Von Figura, G.; Sly, W.S.; Waheed, A.; Hassan, M.I. *Appl. Biochem. Biotechnol.* **2014**, *173*, 333–355.

146. He, J.; Zeng, X.; Lan, S.; Lo, I.M.C. *Chemosphere* **2019**, *217*, 869–878.

147. Yang, S.; Wang, H.; Yu, H.; Zhang, S.; Fang, Y.; Zhang, S.; Peng, F. *Int. J. Hydrogen Energy* **2016**, *41*, 3446–3455.

148. Klug, H.; Alexander, L. *Willey* **1974**, 992.

149. Nobre, F.X.; Gil Pessoa, W.A.; Ruiz, Y.L.; Imbiriba Bentes, V.L.; Silva-Moraes, M.O.; Costa Silva, T.M.; Miranda Rocco, M.L.; González Larrudé, D.R.; de Matos, J.M.E.; da Costa Couceiro, P.R.; et al. *Mater. Res. Bull.* **2019**, *109*, 60–71.

150. Ninomiya, K.; Noda, K.; Ogino, C.; Kuroda, S.I.; Shimizu, N. *Ultrason. Sonochem.* **2014**, *21*, 289–294.

151. Hyunku, J. *Korean J. Chem. Eng.* **2006**, *23*, 931–934.

152. Fónagy, O.; Szabó-Bárdos, E.; Horváth, O. *J. Photochem. Photobiol. A Chem.* **2021**, *407*, 113057.

153. Chung, W.J.; Nguyen, D.D.; Bui, X.T.; An, S.W.; Banu, J.R.; Lee, S.M.; Kim, S.S.; Moon, D.H.; Jeon, B.H.; Chang, S.W. *J. Environ. Manage.* **2018**, *213*, 541–548.

154. Szabó-Bárdos, E.; Kulcsár, P.; Kováts, N.; Békéssy, Z.; Eck-Varanka, B.; Horváth, O. *Luminescence* **2020**, *35*, 434–436.

155. Zhang, J.; Nosaka, Y. *J. Phys. Chem. C* **2014**, *118*, 10824–10832.

156. Wu, C.Y.; Tu, K.J.; Deng, J.P.; Lo, Y.S.; Wu, C.H. *Materials (Basel).* **2017**, *10*, 566.

157. Huang, Z. *Master's Thesis, Univ. Utah* **2017**, 1–92.

158. Eiden-Assmann, S.; Widoniak, J.; Maret, G. *Chem. Mater.* **2004**, *16*, 6–11.

159. Pérez, E.; Torres, M.F.; Morales, G.; Murgia, V.; Sham, E. *Procedia Mater. Sci.* **2015**, *8*, 649–655.

160. Kirkey, A.; Li, J.; Sham, T.K. *Surf. Sci.* **2019**, *680*, 68–74.

161. Albetran, H.; O’Connor, B.H.; Low, I.M. *Appl. Phys. A Mater. Sci. Process.* **2016**, *122*.

162. Baszczuk, A.; Jasiorski, M.; Winnicki, M. *J. Therm. Spray Technol.* **2018**, *27*, 1551–1562.

163. Akple, M.S.; Low, J.; Qin, Z.; Wageh, S.; Al-Ghamdi, A.A.; Yu, J.; Liu, S. *Cuihua Xuebao/Chinese J. Catal.* **2015**, *36*, 2127–2134.

164. Bao, H.; Zhang, H.; Liu, G.; Li, Y.; Cai, W. *Langmuir* **2017**, *33*, 5430–5438.

165. Wang, G.; Xu, L.; Zhang, J.; Yin, T.; Han, D. *Int. J. Photoenergy* **2012**, *2012*, 1–9.

166. Yu, J.; Wang, G. *J. Phys. Chem. Solids* **2008**, *69*, 1147–1151.

167. Sabri, N.A.; Nawi, M.A.; Nawawi, W.I. *Opt. Mater. (Amst).* **2015**, *48*, 258–266.

168. Hu, Y.; Liu, H.; Kong, X.; Guo, X. *J. Nanosci. Nanotechnol.* **2014**, *14*, 3532–3537.

169. Lei, X.F.; Xue, X.X.; Yang, H.; Chen, C.; Li, X.; Niu, M.C.; Gao, X.Y.; Yang, Y.T. *Appl. Surf. Sci.* **2015**, *332*, 172–180.

170. Wu, H.; Ma, J.; Zhang, C.; He, H. *J. Environ. Sci. (China)* **2014**, *26*, 673–682.

171. Ohno, T.; Sarukawa, K.; Tokieda, K.; Matsumura, M. *J. Catal.* **2001**, *203*, 82–86.

172. Junwei, W.; Wei, Z.; Yinqing, Z.; Shuangxi, L. *J. Phys. Chem. C* **2007**, *111*, 1010–1014.

173. Xiang, Q.; Yu, J.; Wong, P.K. *J. Colloid Interface Sci.* **2011**, *357*, 163–167.

174. Nagarajan, S.; Skillen, N.C.; Fina, F.; Zhang, G.; Randorn, C.; Lawton, L.A.; Irvine, J.T.S.; Robertson, P.K.J. *J. Photochem. Photobiol. A Chem.* **2017**, *334*, 13–19.

175. Rutely, B.C.C.; Fontmorin, J.M.; Tang Walter, Z.; Xochitl, D.B.; Mika, S.; Burgos Castillo Rutely, C.; Fontmorin, J.M.; Tang Walter, Z.; Xochitl, D.B.; Mika, S. *RSC Adv.* **2018**, *8*, 5321–5330.

176. Ishibashi, K. ichi; Fujishima, A.; Watanabe, T.; Hashimoto, K. *J. Photochem. Photobiol. A Chem.* **2000**, *134*, 139–142.

177. Narayana, R.L.; Matheswaran, M.; Aziz, A.A.; Saravanan, P. *Desalination* **2011**, *269*, 249–253.

178. Yu, J.; Zhang, L.; Cheng, B.; Su, Y. *J. Phys. Chem. C* **2007**, *111*, 10582–10589.

179. Khaki, M.R.D.; Shafeeyan, M.S.; Raman, A.A.A.; Daud, W.M.A.W. *J. Environ. Manage.* **2017**, *198*, 78–94.

180. Khotseng, L. *InTech* **2018**, 25–50.

181. Land, E.J.; Truscott, T.G. *Photochem. Photobiol.* **1979**, *29*, 861–866.

182. Buxton, G. V.; Greenstock, C.L.; Helman, W.P.; Ross, A.B. *J. Phys. Chem. Ref. Data* **1988**, *17*, 513–886.

183. Näykki, T.; Jalukse, L.; Helm, I.; Leito, I. *Water (Switzerland)* **2013**, *5*, 420–442.

184. Szabó-Bárdos, E.; Czili, H.; Horváth, A. *J. Photochem. Photobiol. A Chem.* **2003**, *154*, 195–201.

185. Rabani, J.; Nielsen, S.O. *J. Phys. Chem.* **1969**, *73*, 3736–3744.

186. Frimer, A.A.; Aljadeff, G.; Gilinsky-Sharon, P. *Isr. J. Chem.* **1986**, *27,* 39–44.

187. He, T.; Guo, X.; Zhang, K.; Feng, Y.; Wang, X. *RSC Adv.* **2014**, *4,* 5880–5886.

188. Liu, G.; Wang, X.; Wang, L.; Chen, Z.; Li, F.; (Max) Lu, G.Q.; Cheng, H.M. *J. Colloid Interface Sci.* **2009**, *334*, 171–175.

189. Wang, T.; Wei, J.; Shi, H.; Zhou, M.; Zhang, Y.; Chen, Q.; Zhang, Z. *Phys. E Low-Dimensional Syst. Nanostructures* **2017**, *86*, 103–110.

190. Behnajady, M.A.; Modirshahla, N.; Shokri, M.; Rad, B. *Glob. Nest J.* **2008**, *10*, 1–7.

191. Abbad, S.; Guergouri, K.; Gazaout, S.; Djebabra, S.; Zertal, A.; Barille, R.; Zaabat, M. *J. Environ. Chem. Eng.* **2020**, *8*, 103718.

192. Zhou, X.; Lu, J.; Cao, J.; Xu, M.; Wang, Z. *Ceram. Int.* **2014**, *40*, 3975–3979.

193. Sirivallop, A.; Areerob, T.; Chiarakorn, S. *Catalysts* **2020**, *10*, 251.

194. Bamwenda, G.R.; Tsubota, S.; Nakamura, T.; Haruta, M. *J. Photochem. Photobiol. A Chem.* **1995**, *89*, 177–189.

195. Gallo, A.; Montini, T.; Marelli, M.; Minguzzi, A.; Gombac, V.; Psaro, R.; Fornasiero, P.; Dal Santo, V. *Chem. Sus. Chem.* **2012**, *5*, 1800–1811.

196. Shang, M.; Hou, H.; Gao, F.; Wang, L.; Yang, W. *RSC Adv.* **2017**, *7*, 30051–30059.

197. Sobana, N.; Muruganadham, M.; Swaminathan, M. *J. Mol. Catal. A Chem.* **2006**, *258*, 124–132.

198. Pham, T.D.; Lee, B.K. *J. Colloid Interface Sci.* **2014**, *428*, 24–31.

199. Rengaraj, S.; Li, X.Z. *J. Mol. Catal. A Chem.* **2006**, *243*, 60–67.

200. Demirci, S.; Dikici, T.; Yurddaskal, M.; Gultekin, S.; Toparli, M.; Celik, E. *Appl. Surf. Sci.* **2016**, *390*, 591–601.

201. Raza, M.A.; Kanwal, Z.; Rauf, A.; Sabri, A.N.; Riaz, S.; Naseem, S. *Nanomaterials* **2016**, *6*, 74.

202. Choi, O.; Deng, K.K.; Kim, N.J.; Ross, L.; Surampalli, R.Y.; Hu, Z. *Water Res.* **2008**, *42*, 3066–3074.

203. Feng, Q.L.; Wu, J.; Chen, G.Q.; Cui, F.Z.; Kim, T.N.; Kim, J.O. *J. Biomed. Mater. Res.* **2000**, *52*, 662–668.

204. Szabó-Bárdos, E.; Markovics, O.; Horváth, O.; Toro, N.; Kiss, G. *Water Res.* **2011**, *45*, 1617–1628.

205. Mahrouqi, H.K.N.; Nawi, M.A.; Nawawi, W.I. *Int. J. Sci. Res. Publ.* **2014**, *4*, 1–7.

206. Bielski, B.H.J.; Cabelli, D.E.; Arudi, R.L.; Ross, A.B. *J. Phys. Chem. Ref. Data* **1985**, *14*, 1041–1100.

9. Attachments

9.1 Text

Text A4.1. Calculation of band-gap energy

The optical properties of catalysts were studied by using diffuse reflectance spectra analysis. Typically, the experimental values of wavelength (λ) were converted into photon energy (E_{photon}) by using the Planck equation, where h is the Planck constant (6.63×10^{-34} J s) and c is the speed of light (3.0×10^{8} m s^{-1}) (Eq. A.1):

$$E_{photon} = \frac{hc}{\lambda} \text{ x } 6.24150 \text{ x } 10^{18} \text{ eV} \qquad \text{(A.1)}$$

The diffuse reflectance data were converted into the Kubelka-Munk function [F(R)] (Eq. A.2):

$$\mathrm{F(R\infty)} = \frac{(1-\mathrm{R\infty})^2}{2\mathrm{R\infty}} = \frac{k}{s} \qquad \text{(A.2)}$$

where k is the characteristic molar absorption coefficient of the material and s is the scattering coefficient of the radiation. R∞ is the absolute reflectance, which can be obtained by the following expression: $R\infty = \%R_{sample} / \%R_{standard}$ ratio. In this work, $BaSO_4$ was used as a reference standard. The band-gap energy (E_g) was calculated by using the Tauc's relation (Eq. A.3):

$$(\alpha hv) = A\,(hv - E_g)^n \qquad \text{(A.3)}$$

considering α~F(R) and an indirect allowed transition (n=2).

Text A4.2. Calculation of quantum yield (Φ)

The overall quantum yield is estimated by using Eq. A.4:

$$\Phi = N_{cpr} / N_{aph} \qquad \text{(A.4)}$$

where

N_{cpr}	= rate of conversion of the probe material (coumarin)
N_{aph}	= rate of absorption of photons at the irradiation wavelength

The amount of converted probe material (coumarin) is calculated by using Eq. A.5:

$$N_{cpr} = V \times C \times k \qquad \text{mol s}^{-1} \qquad \text{(A.5)}$$

where

V = volume of coumarin solution (0.05 dm^3)

C = concentration of coumarin (0.8×10^{-4} mol dm^{-3})

k = the first order rate constant of coumarin degradation (s^{-1})

The amount of absorbed photons is calculated by using Eqs. A.6-A.7:

$$U_\lambda = (h \times c \times N_A) / \lambda \qquad \text{J mol}^{-1} \qquad \text{(A.6)}$$

$$N_{aph} = (E \times A) / U_\lambda \qquad \text{mol s}^{-1} \qquad \text{(A.7)}$$

where

U_λ = mole photon energy of representative wavelength (J mol^{-1}),

h = Planck constant (6.63×10^{-34} J s)

c = speed of light in vacuum (3×10^8 m s^{-1})

N_A = Avogadro number (6.02×10^{23} mol^{-1})

λ = representative wavelength of light source (m)

E = light intensity absorbed by the catalyst (W cm^{-2})*

A = area of circle quartz glass reactor (28.26 cm^2)

* Since the exact measurement of absorbed light is difficult for powdered catalyst, the number of incident light can be used for the calculation of quantum yield.

Text A4.3. Sample preparation for antibacterial study

For measurements of the antibacterial effect, the catalyst samples were immobilized in an acrylate based polymer on a plastic surface. The catalyst concentration on the plastic surface was 485 mg m^{-2}. Discs of 1 cm diameter were cut from this plastic sheet and fixed to the bottom of small, open sample containers (glass tubes) with screw caps. The bacterial suspensions were layered on the samples. The antibacterial effects of the catalysts were measured by using *Vibrio fischeri* luminescent bacteria. After reconstitution, the guaranteed life-span of bacteria was 4 hours. The suspension of bacteria was incubated for 80 min at 15 °C. At the end of the incubation period, 0.5 cm^3 sample was measured into the sample holders, which were kept in the dark during the experiment, and the emission intensities of the samples were recorded at defined times. The reference sample was stored in a bottle, which did not contain any plastic disc. The control sample contained a disc from a commercially available plastic sheet with antibacterial surface. During the evaluation, the results obtained from 3 parallel measurements were averaged and then the relative decomposition percentage was calculated. Afterwards, the relative decomposition (%) of the actual sample was compared to the control one.

9.2 Figure

		
150 °C (white)	350 °C (yellowish)	400 °C (yellowish)
	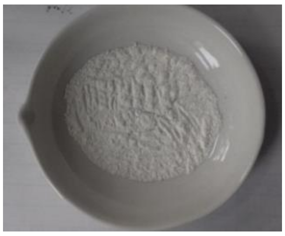	
450 °C (yellowish)	500 °C (white)	650 °C (white)

Figure A4.1. Photograph of NT-A catalysts under various calcination temperatures.

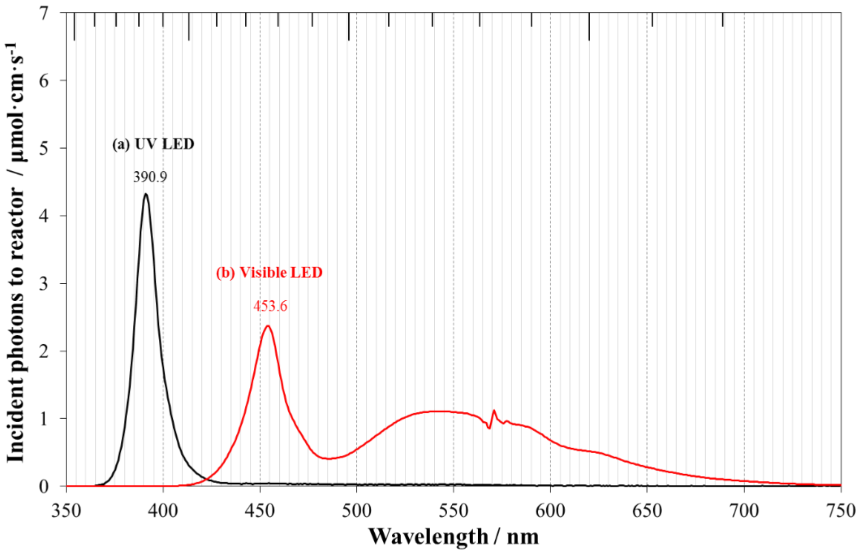

Figure A4.2. Emission spectra of (a) UV and (b) visible LEDs.

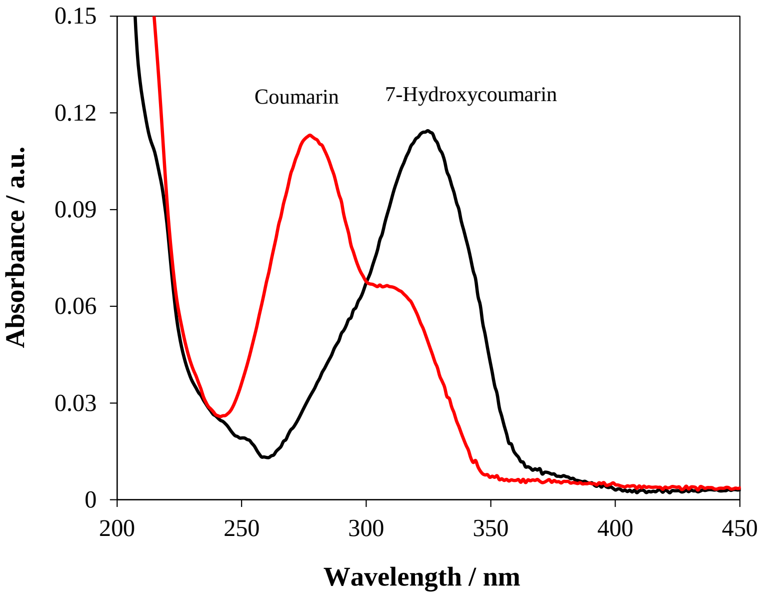

Figure A4.3. Absorbance spectra of coumarin and 7-hydroxycoumarin.

$c = 10^{-5}$ M, path length:1 cm

Wavelength (nm)	**Molar absorption coefficient ($M^{-1}\,cm^{-1}$)**	
	coumarin	**7-hydroxycoumarin**
277	11308	3209
324	5122	11405

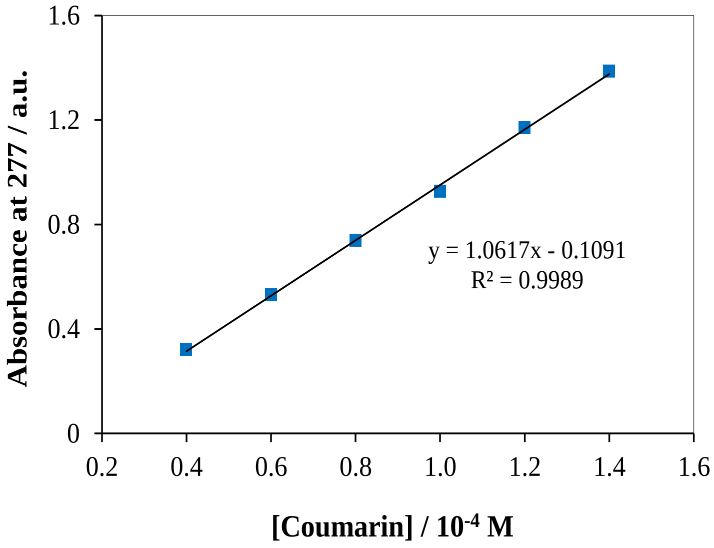

Figure A4.4. Calibration curves of coumarin.

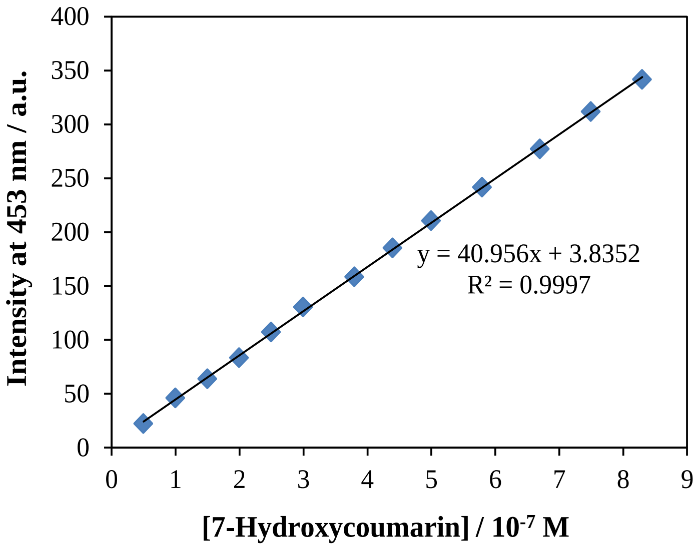

Figure A5.1. Calibration curves of 7-hydroxycoumarin.

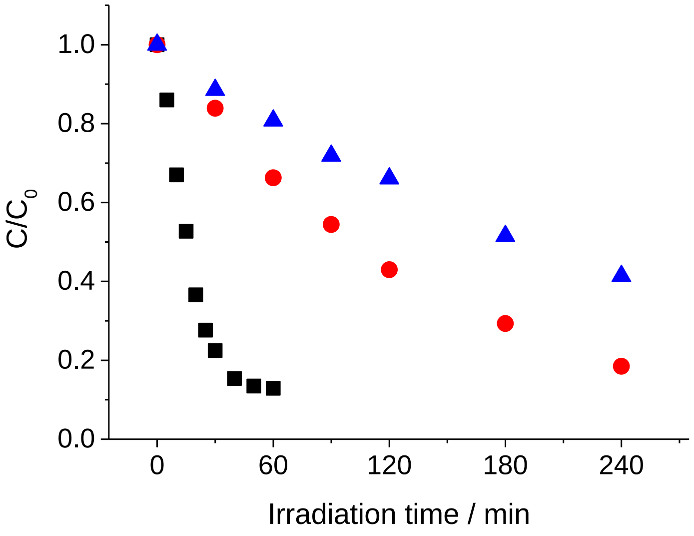

■ – Degussa P25 TiO_2 ● – undoped TiO_2 ▲ – NT-A 450 °C

Figure A5.2. Coumarin degradation over various catalysts under UV illumination.

c_0(coumarin) = 0.8×10^{-4} M, c(catalyst) = 1 g dm^{-3}, UV LED, 20 dm^3 h^{-1} air

Rate constant and quantum yield for degradation of coumarin over various catalysts under UV illumination.

Catalyst	**k / $\times10^{-4}$ s^{-1}**	**Quantum yield / %**
Degussa P25 TiO_2	8.05	0.46
Undoped TiO_2	1.16	0.07
NT-A 450 °C	0.61	0.04

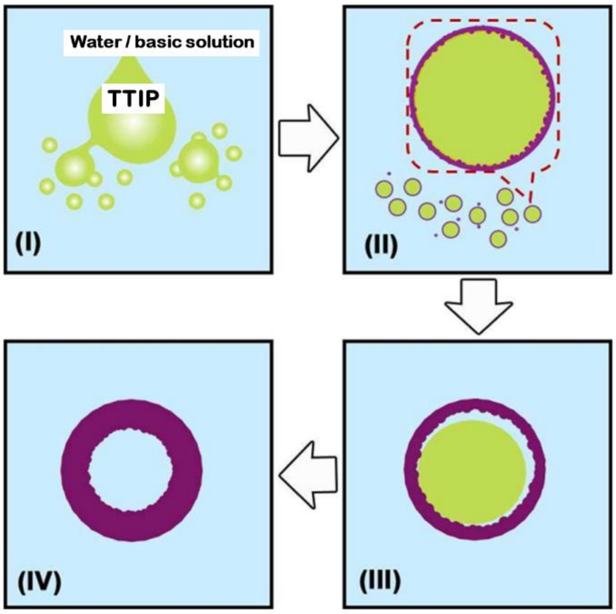

Figure A5.3. Schematic illustration of the formation of hollow structure for the second dosing order (HNO_3-NH_4OH-H_2O-TTIP).

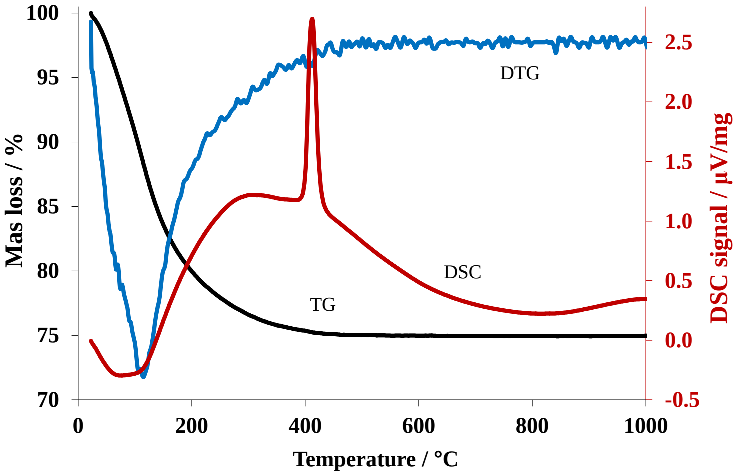

Figure A5.4. TG-DSC curve of NT-A catalysts.

Starting sample = the sample dried at 40 °C for 24 h in the preparation step

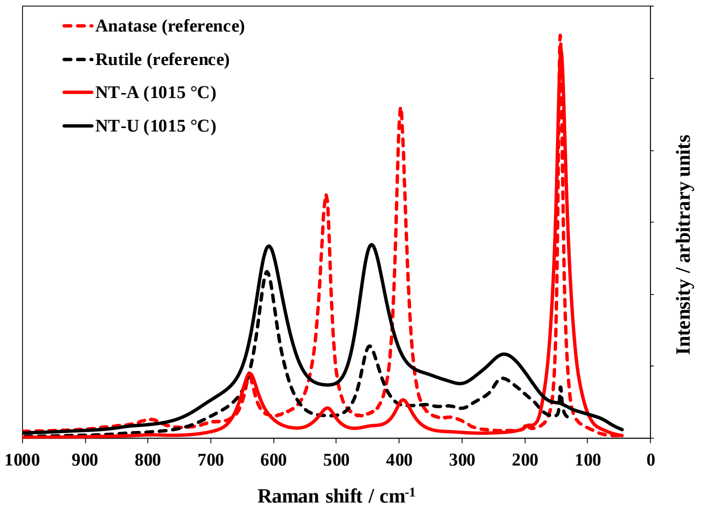

Figure A5.5. Raman spectra of NT-U and NT-A catalysts after heating treatment at 1015 °C.

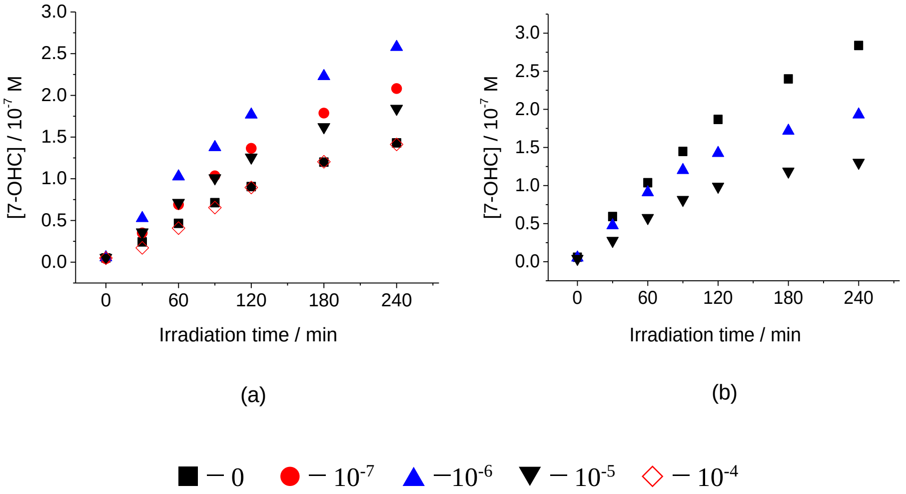

(a)

(b)

Figure A5.6. 7-OHC formation of (a) Ag/NTU and (b) Ag/NT-A with different Ag-loadings (mol Ag g^{-1} catalyst).

c_0(coumarin) = 0.8×10^{-4} M, c(catalyst) = 1 g dm^{-3}, Vis LED (2nd arrangement), 20 dm^3 h^{-1} air

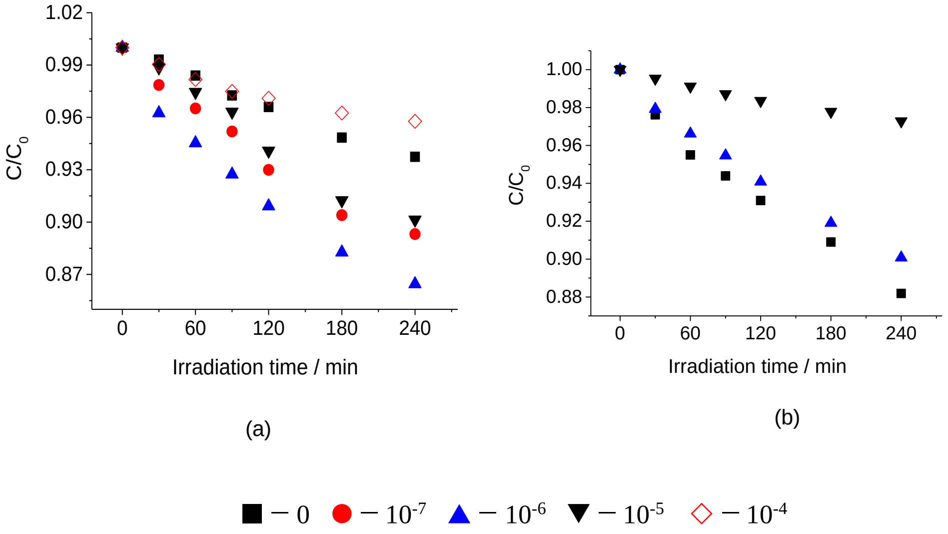

(a)

(b)

Figure A5.7. Coumarin degradation of (a) Ag/NTU and (b) Ag/NT-A with different Ag-loadings (mol Ag g^{-1} catalyst).

c_0(coumarin) = 0.8×10^{-4} M, c(catalyst) = 1 g dm^{-3}, Vis LED (2nd arrangement), 20 dm^3 h^{-1} air

Rate constant and quantum yield for degradation of coumarin over various catalysts under visible illumination.

Catalyst	***k* / ×10^{-6} s^{-1}**	**Quantum yield / ×10^{-4} %**
NT-U	5.00	1.0
Ag/NT-U 10^{-6}	10.00	2.1
Ag/NT-U 10^{-5}	8.33	1.8
NT-A	10.00	2.1
Ag/NT-A 10^{-6}	8.33	1.8
Ag/NT-A 10^{-5}	1.67	0.3

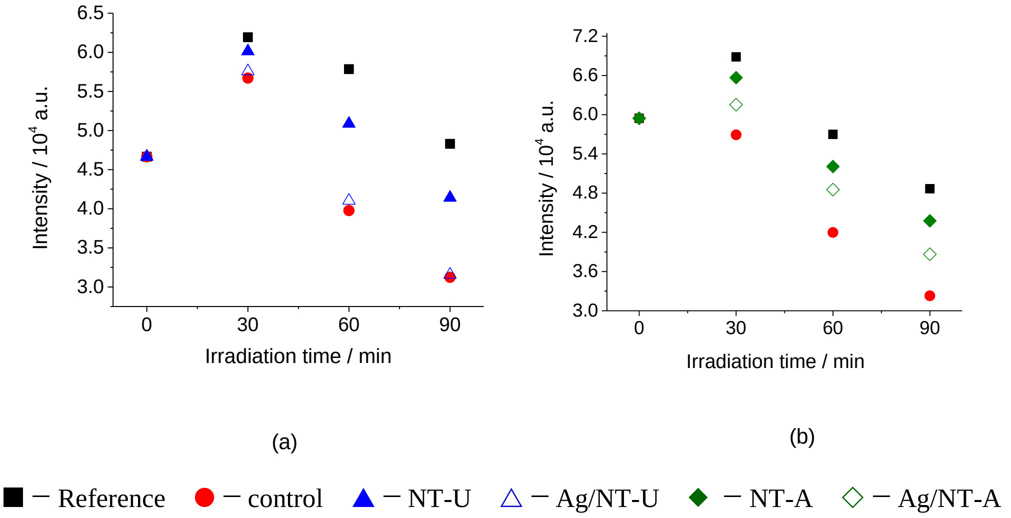

(a)

(b)

Figure A5.8. Luminescence intensity of bacterial suspension in the presence of (a) Ag/NT-U and (b) Ag/NT-A catalysts (with 10^{-6} mol Ag g^{-1} catalyst) compared to the reference and control samples.

Relative decomposition of bacteria in presence of NT-U and Ag/NT-U (with 10^{-6} mol Ag g^{-1} catalyst) catalysts as well as the control sample.

Time / min	**NT-U / %**	**Ag/NT-U / %**	**Control / %**
0	0.0	0.0	0.0
30	2.9	7.0	8.4
60	12.1	29.1	31.2
90	14.3	34.6	35.3

Relative decomposition of bacteria in presence of NT-A and Ag/NT-A (with 10^{-6} mol Ag g^{-1} catalyst) catalysts as well as the control sample.

Time / min	**NT-A / %**	**Ag/NT-A / %**	**Control / %**
0	0.0	0.0	0.0
30	4.6	10.6	17.3
60	8.6	14.8	26.3
90	10.1	20.6	33.7

9.3 Table

Table A5.1. Ratio ($v_{0\ \mathrm{UV/Vis}}$) of 7-OHC formation under UV and visible irradiations.

Catalyst	**v_0 of 7-OHC formation / 10^{-10} M min^{-1}**		**Ratio (a:b)**
	(a) UV	**(b) visible**	
NT-A 350 °C	15.7	3.0	5.2
NT-A 400 °C	26.5	3.7	7.2
NT-A 450 °C	43.7	5.3	8.3
NT-A 500 °C	49.9	1.7	29.4
NT-A 650 °C	93.8	0.5	187.6

10. Acknowledgements

The completion of this dissertation is one of the important milestones in my life. I realize, I could not have achieved this without the help of several people and programs.

My deepest gratitude goes first to my supervisors: Dr. Ottó Horváth, DSc. and Dr. Erzsébet Szabó-Bárdos, PhD, who have guided, supported, and encouraged me during this long journey. Their patience and dedication kept me constantly engaged with my research and their generous personality made my time in Hungary enjoyable.

My appreciation also extends to all people who contributed to my research, including Dr. Mihály Pósfai, DSc. for TEM-EDS analyses, Dr. Éva Makó for XRD analyses, Dr. Tatyana Juzsakova for BET analyses, Dr. Balázs Zsirka for TG-DSC analyses, Orsolya Fónagy for HPLC measurements, Miklós Jakab for SEM-EDS analyses, Edina Ring-Nyári for TOC measurements, and Petra Kulcsár for antibacterial measurements.

I would like to thank for all financial supports we received, such as the scholarship for my PhD study in the frame of the Stipendium Hungaricum Program as well as the financial aids for research activities, provided by the Széchenyi 2020 program of the Hungarian Ministry for Innovation and Technology and by the Thematic Excellence Program of the National Research, Development and Innovation Fund of Hungary.

Furthermore, I am indebted to my parents, Abdul Adzim and Sulastri, who constantly put my name in their prayer every day. And finally, I sincerely acknowledge the continuous physical and spiritual support of my lovely wife, Mrs. Dian Naelatul Karimah and our little daughter, Nashwa Putri Avicenna, who have accompanied, encouraged, and balanced my life in Hungary.